

**İSTANBUL TECHNICAL UNIVERSITY ★ INSTITUTE OF SCIENCE AND TECHNOLOGY**

**THREE-DIMENSIONAL COMPUTATIONAL ANALYSIS OF THE FLOW  
AROUND AN OSCILLATING FLAT-PLATE**

**M.Sc. Thesis by  
Sophia BUCKINGHAM**

**Department : Aeronautical Engineering  
Programme : Aeronautical and Astronautical  
Engineering (Interdisciplinary)**

**JUNE 2009**



**THREE-DIMENSIONAL COMPUTATIONAL ANALYSIS OF THE FLOW  
AROUND AN OSCILLATING FLAT-PLATE**

**M.Sc. Thesis by  
Sophia BUCKINGHAM  
(511071151)**

**Date of submission : 04 May 2009  
Date of defence examination: 03 June 2009**

**Supervisor (Chairman) : Assoc. Prof. Dr. Fırat Oğuz EDİS (İTÜ)  
Members of the Examining Committee : Prof. Dr. Mehmet Fevzi ÜNAL (İTÜ)  
Prof. Dr. Aydın MISIRLIOĞLU (İTÜ)**

**JUNE 2009**



**İSTANBUL TEKNİK ÜNİVERSİTESİ ★ FEN BİLİMLERİ ENSTİTÜSÜ**

**SALINIM YAPAN DÜZ LEVHA ETRAFINDAKİ ÜÇ-BOYUTLU AKIŞIN  
ANALİZİ**

**YÜKSEK LİSANS TEZİ  
Sophia BUCKINGHAM  
(511071151)**

**Tezin Enstitüye Verildiği Tarih : 04 Mayıs 2009**

**Tezin Savunulduğu Tarih : 03 Haziran 2009**

**Tez Danışmanı : Assoc. Prof. Dr. Fırat Oğuz EDİS (İTÜ)  
Diğer Jüri Üyeleri : Prof. Dr. Mehmet Fevzi ÜNAL (İTÜ)  
Prof. Dr. Aydın MISIRLIOĞLU (İTÜ)**

**HAZİRAN 2009**



## **FOREWORD**

First of all I want to give my special thanks to my supervisor Assoc. Prof. Dr. Fırat Oğuz Edis, for all his support, valuable instructions and kindness towards me during my study.

Thanks to all my professors in Istanbul Technical University for every bit of information I have learned from them.

Last but not least, I want to thank my family for their morale support, encouragement and understanding throughout this time.

May 2009

Sophia Buckingham  
Aeronautical Engineer





## TABLE OF CONTENTS

	<u>Page</u>
<b>ABBREVIATIONS</b> .....	<b>xi</b>
<b>LIST OF TABLES</b> .....	<b>xii</b>
<b>LIST OF FIGURES</b> .....	<b>xiii</b>
<b>LIST OF SYMBOLS</b> .....	<b>xvii</b>
<b>SUMMARY</b> .....	<b>xix</b>
<b>ÖZET</b> .....	<b>xxi</b>
<b>1. INTRODUCTION TO LOW-REYNOLDS NUMBER FLOWS</b> .....	<b>1</b>
1.1 Presentation of the Subject.....	1
1.1.1 Motivations and applications of Micro-Air Vehicles .....	1
1.1.2 Challenges and objectives.....	5
1.1.3 Organization.....	6
1.2 Governing Parameters of the Flow and Flapping Motion.....	7
1.2.1 Critical parameters of oscillating airfoils.....	7
1.2.1.1 Kinematics .....	8
1.2.1.2 Flapping parameters.....	9
1.2.1.3 Thrust generation .....	9
1.2.1.4 Propulsive efficiency.....	10
1.2.2 Non-dimensional parameters .....	11
1.2.2.1 Mach number .....	11
1.2.2.2 Reynolds number .....	11
1.2.2.3 Amplitude ratio .....	12
1.2.2.4 Aspect ratio .....	13
1.3 Flow-Physics of Low Reynolds-Number Flows.....	13
1.3.1 Shear stress and boundary layer separation .....	13
1.3.2 Aerodynamic coefficients .....	16
1.3.3 Reynolds-number effects .....	18
1.3.4 Static and dynamic stall types.....	19
1.3.4.1 Static stall.....	19
1.3.4.2 Dynamic stall .....	21
1.3.5 Vortex shedding allowing thrust generation .....	21
1.4 Previous Work on Unsteady Low-Speed Aerodynamics.....	27
1.4.1 Plunging airfoils.....	27
1.4.2 Pitching airfoils.....	33
1.4.3 Combined pitching and plunging airfoil .....	35
1.4.4 Three-dimensional flow effects.....	45
<b>2. METHODOLOGY APPLIED TO THE COMPUTATIONAL ANALYSIS</b> .....	<b>51</b>
2.1 Generation of the Mesh.....	52
2.1.1 Definition of the model.....	52
2.1.2 Presentation of Gridgen .....	53
2.1.3 Grid generation technique.....	55

2.1.3.1	Extrusion from the 2D section .....	57
2.1.3.2	Creation of the flat-plate tip by revolution.....	62
2.1.3.3	Flat-plate surface by translation .....	63
2.2	Finite Volume Method .....	65
2.2.1	Introduction to Computational Fluid Dynamics.....	65
2.2.2	Governing equations given in conservative form .....	67
2.2.2.1	Mass conservation .....	68
2.2.2.2	Momentum conservation.....	69
2.2.2.3	Energy conservation.....	71
2.2.2.4	Navier-Stokes equations.....	74
2.2.3	Turbulence modeling.....	75
2.2.3.1	Introduction .....	75
2.2.3.2	Turbulence models .....	77
2.2.4	Wall treatment .....	80
2.2.4.1	Viscous sublayer .....	80
2.2.4.2	Buffer region .....	80
2.2.4.3	The outer layer .....	81
2.2.4.4	Near-wall modelling approach.....	82
2.2.4.5	Calculation of the first mesh height .....	84
2.3	Set-Up of the Computational Fluid Dynamic Simulation.....	86
2.3.1	Implementation of the Boundary Conditions.....	86
2.3.2	Implementation of the Flapping Motion .....	87
2.3.3	Fluent parameters .....	90
<b>3.</b>	<b>RESULTS OBTAINED FOR THE FLAT-PLATE MODEL.....</b>	<b>91</b>
3.1	Introduction to the Simulation Cases .....	91
3.2	Preparatory Work .....	92
3.2.1	Verification of the motion .....	92
3.2.2	Time step determination.....	95
3.2.3	Periodicity of the results.....	97
3.3	Mesh Effect Study .....	98
3.4	Structure of the Flow.....	101
3.4.1	Formation of the leading-edge vortex .....	101
3.4.2	Tip effects.....	107
3.5	Parameter Study .....	112
3.5.1	Effect of the aspect-ratio .....	112
3.5.2	Effect of the mean angle of attack.....	115
3.5.3	Effect of the amplitude ratio.....	119
3.5.4	Effect of the reduced frequency .....	124
3.6	Conclusions .....	131
	<b>REFERENCES.....</b>	<b>135</b>
	<b>APPENDICES .....</b>	<b>139</b>
	<b>CURRICULUM VITA.....</b>	<b>149</b>

## **ABBREVIATIONS**

<b>AR</b>	: Aspect Ratio
<b>CFD</b>	: Computational Fluid Dynamics
<b>FVM</b>	: Finite Volume Method
<b>LE</b>	: Leading Edge
<b>LEV</b>	: Leading Edge Vortex
<b>LSB</b>	: Laminar Separation Bubble
<b>MAV</b>	: Micro Air Vehicle
<b>RANS</b>	: Reynolds Averaged Navier-Stokes
<b>TE</b>	: Trailing Edge
<b>UDF</b>	: User Defined Function

## LIST OF TABLES

	<b><u>Page</u></b>
<b>Table 2.1:</b> Characteristic parameters of the coarse and fine grids.....	65
<b>Table 3.1:</b> Simulation cases .....	91
<b>Table 3.2:</b> Modified mesh parameters characterizing the final grid.....	100
<b>Table 3.3:</b> Effect of the AR on the thrust and power input coefficients.....	115
<b>Table 3.4:</b> Effect of the mean flow angle on the thrust and power input coefficients .....	119
<b>Table 3.5:</b> Pitch amplitudes related to each amplitude ratio .....	120
<b>Table 3.6:</b> Effect of the amplitude ratio on the thrust and power input coefficients .....	123
<b>Table 3.7:</b> Effect of the reduced frequency on the performance parameters .....	130

## LIST OF FIGURES

	<u>Page</u>
<b>Figure 1.1</b> : a) Fixed-wing MAV [1] b) Rotary-wing MAV [2].....	2
<b>Figure 1.2</b> : a) Flexible-flapping wing [3] b) Bi-plane configuration of a flapping wing [4] .....	4
<b>Figure 1.3</b> : Two-degree-of-freedom motion .....	8
<b>Figure 1.4</b> : Two-degree-of-freedom motion .....	8
<b>Figure 1.5</b> : Wing planform and aspect ratio .....	13
<b>Figure 1.6</b> : a) Boundary layer thickness $\delta$ b) Flow separation .....	14
<b>Figure 1.7</b> : a) Boundary layer profiles [7] b) Transitional separation bubble (Horton 1968) .....	15
<b>Figure 1.8</b> : Definition and representation of the aerodynamic coefficients.....	16
<b>Figure 1.9</b> : Aerodynamic coefficients with respect to the angle of attack a) $C_L / \alpha$ b) $C_D / \alpha$ c) $C_M / \alpha$ .....	18
<b>Figure 1.10</b> : Effect of the Reynolds-number on the maximum lift coefficient [7]..	19
<b>Figure 1.11</b> : a) Progression of the trailing-edge stall b) Reattachment of the LSB.	20
<b>Figure 1.12</b> : Vortex shedding taking place during dynamic stall .....	21
<b>Figure 1.13</b> : First theory describing the generation of thrust from a flapping airfoil .....	22
<b>Figure 1.14</b> : Surface and wake vortex sheet .....	23
<b>Figure 1.15</b> : Starting Vortex resulting from a sudden incidence change.....	23
<b>Figure 1.16</b> : Vortical wake induced by sinusoidal plunge oscillation a) $k = 0.5$ b) $k = 1.0$ .....	24
<b>Figure 1.17</b> : a) Drag producing wake for a stationary NACA0012 airfoil b) Thrust producing wake for a NACA0012 airfoil undergoing pure plunging motion .....	25
<b>Figure 1.18</b> : Vortex Street indicative of a jet-like flow .....	25
<b>Figure 1.19</b> : Comparison of time-averaged velocity profiles .....	26
<b>Figure 1.20</b> : Transition from normal to reverse Karman vortex street as $kh$ increases a) $kh = 0$ b) $kh = 0.1$ c) $kh = 0.2$ d) $kh = 0.4$ .....	28
<b>Figure 1.21</b> : a) $C_x$ , $C_z$ and $\alpha_{\text{eff}}$ for one plunge period b) Division of the h-k plane at $k = 0.35$ .....	29
<b>Figure 1.22</b> : Thrust coefficient and propulsive efficiency as a function of the reduced frequency .....	30
<b>Figure 1.23</b> : a) Vorticity field for $k = 2$ (downstroke) b) Vorticity $k = 6.667$ (downstroke) .....	31
<b>Figure 1.24</b> : a) Flow visualization b) Panel code prediction, $kh = 1.5$ .....	32
<b>Figure 1.25</b> : a) Variation of $C_{T\text{mean}}$ with $kh$ for $h = 0.175$ b) Variation of $\eta_p$ with $kh$ for $h = 0.175$ .....	32
<b>Figure 1.26</b> : a) Ratio of E/K as a function of $1/k$ [15] b) Experimental verification of Garrick's predictions [31].....	33
<b>Figure 1.27</b> : Results collected by [32] a) Frequency variation b) $\alpha_0$ variation c) $C_T$ Vs. $k$ .....	34

<b>Figure 1.28</b> : a) Rigid airfoil in pure pitch b) Pressure distributions (pitching motion)	35
<b>Figure 1.29</b> : a) Numerical predictions as a function of $\varphi$ [33] b) $\eta_p$ as a function of $k$ and $\varphi$ [34]	37
<b>Figure 1.30</b> : Propulsive efficiency as a function of Strouhal number [28]	38
<b>Figure 1.31</b> : Contour plot of the wake vorticity for different $k$ values [37] a) $St=2.0$ , b) $St=1.0$ , c) $St=0.5$	39
<b>Figure 1.32</b> : Vorticity contour plot and $C_L$ for $\alpha = 40^\circ$ and $Re = 1000$ [37]	39
<b>Figure 1.33</b> : a) Evolution of $C_D$ in time ( $\Delta\alpha$ ) [37] b) Evolution of $C_x$ as a function of $\alpha$ [37]	40
<b>Figure 1.34</b> : Thrust and efficiency as functions of $St_c$ for various $St_a$ values [37]	41
<b>Figure 1.35</b> : Propulsive efficiency as a function of $St$ for several angles [38]	42
<b>Figure 1.36</b> : a) Optimization cases and starting conditions [42] b) Optimization results [42]	44
<b>Figure 1.37</b> : a) Equalizing of pressure at the wing tips b) Tip vortices in three-dimensions	45
<b>Figure 1.38</b> : Tip vortex system in the wake of an aircraft	46
<b>Figure 1.39</b> : a) Wing geometry and parameters [43] b) Pressure distributions along the span [43]	48
<b>Figure 1.40</b> : a) Effect of twisting on $C_T$ [43] b) Effect of twisting on $\eta_p$ [43]	48
<b>Figure 1.41</b> : a) Plan view of 3D flapping airfoil [46] b) Effect of twisting on $\eta_p$ [46]	49
<b>Figure 1.42</b> : Shed vorticity behind a three-dimensional flapping wing	50
<b>Figure 2.1</b> : Technical drawing of the flat-plate geometry	52
<b>Figure 2.2</b> : Half section of the flat-plate model	56
<b>Figure 2.3</b> : a) Flat-plate tip after rotation of the 2D section b) Inside view of the rounded edge	56
<b>Figure 2.4</b> : Final geometry after applying the translational operation ( $AR = 1$ )	56
<b>Figure 2.5</b> : Extrusion from the edge of the flat-plate section	57
<b>Figure 2.6</b> : Extrusion operation and growth rate	58
<b>Figure 2.7</b> : Mesh surrounding the half flat-plate resulting from the extrusion process	58
<b>Figure 2.8</b> : a) Mesh surrounding the flat-plate model b) Mesh around the LE	59
<b>Figure 2.9</b> : 2D mesh obtained at the end of step 1	60
<b>Figure 2.10</b> : a) Mesh before applying the elliptic solver b) Mesh after applying the elliptic solver	61
<b>Figure 2.11</b> : Rotation of the 2D mesh surrounding the half flat-plate section	62
<b>Figure 2.12</b> : a) Total rotational angle of 180 degrees b) Block resulting from the revolution operation	62
<b>Figure 2.13</b> : a) Selected domains to be translated b) Sub-connector used during the translation operation	63
<b>Figure 2.14</b> : Projection of the 2D flat-plate section along the sub-connector	64
<b>Figure 2.15</b> : View of the final grid	64
<b>Figure 2.16</b> : Mass flows in and out of the element [47]	68
<b>Figure 2.17</b> : Forces in the x-direction [47]	70
<b>Figure 2.18</b> : Energy fluxes in the x-direction	73
<b>Figure 2.19</b> : Decomposition of the boundary layer into three layers	81
<b>Figure 2.20</b> : a) Wall function approach b) Near-wall model approach	82
<b>Figure 2.21</b> : a) Skin friction over the flat-plate surface b) $y^+$ values over the flat-plate surface	85

<b>Figure 2.22</b> : a) Boundary conditions applied to the CFD domain b) No-slip wall BC at the flat-plate surface.....	86
<b>Figure 2.23</b> : Fluent parameters .....	90
<b>Figure 3.1</b> : Cursors positioned at LE and TE.....	93
<b>Figure 3.2</b> : a) Residuals during the first iteration b) Behavior of the residuals for $\Delta t = T/1000$ .....	95
<b>Figure 3.3</b> : Effect of the time step on the time variation of $C_D$ - case A .....	96
<b>Figure 3.4</b> : a) Periodicity of $C_L$ – case A b) Periodicity of $C_D$ – case A .....	97
<b>Figure 3.5</b> : Effect of the mesh on the lift and drag coefficients.....	98
<b>Figure 3.6</b> : a) Vorticity contours at the tip of flat-plate with the coarse grid – case B b) Mesh at the tip of the flat-plate with the coarse grid – case B.....	99
<b>Figure 3.7</b> : a) Vorticity contours at the tip of flat-plate with the final grid – case B b) Mesh at the tip of the flat-plate with the final grid – case B.....	100
<b>Figure 3.8</b> : a) xy planes in the chordwise direction x b) xz planes in the spanwise directions z.....	101
<b>Figure 3.9</b> : Spanwise vorticity contours in the symmetry plane - cased A a) $t = 0$ b) $t = T/4$ c) $t = T/2$ d) $t = 3T/4$ .....	102
<b>Figure 3.10</b> : a) Kinematics of the flapping motion – case A b) Behavior of the $C_D$ and $C_L$ in time – case A.....	103
<b>Figure 3.11</b> : Velocity vector flow fields fields – case A a) $t = 0$ b) $t = T/4$ c) $t = T/2$ d) $t = 3T/4$ .....	103
<b>Figure 3.12</b> : a) Velocity vectors at the LE ( $t = T/2$ ) – case A b) Velocity vectors at the TE ( $t = 3T/4$ ) – case A.....	104
<b>Figure 3.13</b> : a) Velocity vectors at the TE, $t = 2T/3$ 3 – case A b) Velocity vectors at $t = 5T/6$ – case A.....	106
<b>Figure 3.14</b> : Pressure distributions throughout the period (- $C_p$ values) .....	107
<b>Figure 3.15</b> : Vorticity components in the TE plane a) spanwise vorticity at $t = 0$ b) streamwise vorticity at $t = 0$ c) spanwise vorticity at $t = 3T/4$ b) streamwise vorticity at $t = 3T/4$ .....	108
<b>Figure 3.16</b> : Spanwise vorticity contours at $t = 3T/4$ – case A a) symmetry plane b) plane at 50% span c) plane at 75% span d) tip plane.....	110
<b>Figure 3.17</b> : Evolution of the pressure distributions spanwise at $t = 3T/4$ – case A .....	111
<b>Figure 3.18</b> : Evolution of the lift and drag coefficients according to the aspect ratio – case A & B a) $C_L$ Vs. time b) $C_D$ Vs. time. ....	112
<b>Figure 3.19</b> : Vorticity contours in the TE plane at $t = 3T/4$ a) $AR = 2$ – case A b) $AR = 1$ – case B.....	113
<b>Figure 3.20</b> : Vorticity contours in the plane at 50% span at $t = 3T/4$ a) $AR = 2$ – case A b) $AR = 1$ – case B.....	113
<b>Figure 3.21</b> : Velocity vectors in symmetry plane at $t = 3T/4$ a) $AR = 2$ – case A b) $AR = 1$ – case B .....	114
<b>Figure 3.22</b> : Effect of the AR on the pressure distributions in the symmetry plane a) $AR = 2$ – case A b) $AR = 1$ – case B.....	114
<b>Figure 3.23</b> : Evolution of the lift and drag coefficients according to the mean flow angle – case A & C a) $C_L$ Vs. time b) $C_D$ Vs. time. ....	116
<b>Figure 3.24</b> : Vorticity contours in the chordwise direction at $t = 0$ a) Sym. plane, $8^\circ$ - case A b) 50% span plane, $8^\circ$ - case A c) 75% span plane, $8^\circ$ - case A d) Tip plane, $8^\circ$ - case A a) Sym. plane, $4^\circ$ - case C b) 50% span plane, $4^\circ$ - case C c) 75% span plane, $4^\circ$ - case C d) Tip plane, $4^\circ$ - case C	117

<b>Figure 3.25</b> : Vorticity contours in the spanwise direction at $t = 3T/4$ a) 33% chord plane, $8^\circ$ - case A b) TE plane, $8^\circ$ - case A c) 1 chord after TE plane, $8^\circ$ - case A d) 33% chord plane, $4^\circ$ - case C b) TE plane, $4^\circ$ - case C c) 1 chord after TE plane, $4^\circ$ - case C.....	117
<b>Figure 3.26</b> : Velocity vectors at $t = T/2$ a) $\alpha_0 = 4^\circ$ - case C b) $\alpha_0 = 8^\circ$ - case A ....	117
<b>Figure 3.27</b> : Effect of the mean flow angle on the pressure distributions in the symmetry plane a) $\alpha_0 = 4^\circ$ - case C b) $\alpha_0 = 8^\circ$ - case A .....	118
<b>Figure 3.28</b> : Evolution of the lift and drag coefficients according to the amplitude ratio – case D, E & A a) CL Vs. time b) CD Vs. time. ....	120
<b>Figure 3.29</b> : Streamwise vorticity contours at $t = 0$ in the TE plane a) $\lambda = 0.4$ – case D b) $\lambda = 0.6$ – case A c) $\lambda = 0.75$ – case E. ....	121
<b>Figure 3.30</b> : Velocity vector flow fields in the LE region of the symmetry plane at $t = T/2$ a) $\lambda = 0.4$ – case D b) $\lambda = 0.6$ – case A c) $\lambda = 0.75$ – case E. ..	122
<b>Figure 3.31</b> : Velocity vector flow fields in the symmetry plane at $t = 3T/4$ a) $\lambda = 0.4$ – case D b) $\lambda = 0.6$ – case A c) $\lambda = 0.75$ – case E. ....	122
<b>Figure 3.32</b> : a) $-C_p$ values in sym. plane, $\lambda = 0.4$ – case D b) $-C_p$ values in sym. plane, $\lambda = 0.6$ – case A c) $-C_p$ values in sym. plane, $\lambda = 0.75$ – case E d) Effect of the amplitude ratio on the thrust coefficient. ....	123
<b>Figure 3.33</b> : Evolution of the lift and drag coefficients according to the reduced frequency – case F, G, H & A a) CL Vs. time b) CD Vs. time. ....	124
<b>Figure 3.34</b> : Vorticity contours in the symmetry plane at $t = 0$ a) $k = 0.15$ – case F b) $k = 0.25$ – case A c) $k = 0.35$ – case G d) $k = 0.5$ – case H .....	125
<b>Figure 3.35</b> : Contours of vorticity magnitude in the TE plane at $t = 0$ a) $k = 0.15$ – case F b) $k = 0.25$ – case A c) $k = 0.35$ – case G d) $k = 0.5$ – case H. ....	125
<b>Figure 3.36</b> : Velocity vector flow fields in the symmetry plane at $t = 0$ a) $k = 0.15$ – case F b) $k = 0.25$ – case A c) $k = 0.35$ – case G d) $k = 0.5$ – case H. ....	126
<b>Figure 3.37</b> : Streamwise vorticity in the TE plane at $a = 0$ a) $k = 0.15$ – case F b) $k = 0.25$ – case A c) $k = 0.35$ – case G d) $k = 0.5$ – case H.....	126
<b>Figure 3.38</b> : Contours of vorticity magnitude at $t = 0$ a) sym. plane, $k = 0.15$ – case F b) plane at 50% span, $k = 0.15$ – case F c) plane at 75% span, $k = 0.15$ – case F d) sym. plane, $k = 0.5$ – case H e) plane at 50% span, $k = 0.5$ – case H f) plane at 75% span – $k = 0.5$ – case H.....	127
<b>Figure 3.39</b> : Velocity vector flow fields in the symmetry plane a) $t = T/2$ , $k = 0.15$ – case F b) $t = T/2$ , $k = 0.25$ – case A c) $t = T/2$ , $k = 0.35$ – case G d) $t = T/2$ , $k = 0.5$ – case H e) $t = 3T/4$ , $k = 0.15$ – case F f) $t = 3T/4$ , $k = 0.25$ – case A g) $t = 3T/4$ , $k = 0.35$ – case G h) $t = 3T/4$ , $k = 0.5$ – case H.....	128
<b>Figure 3.40</b> : Pressure distributions in the symmetry plane a) $k = 0.15$ – case F b) $k = 0.25$ – case A c) $k = 0.35$ – case G d) $k = 0.5$ – case H. ....	129
<b>Figure 3.41</b> : Effect of the reduced frequency on the thrust coefficient .....	130
<b>Figure 3.42</b> : a) Experimental data for the average thrust coefficient of an airfoil [48] b) Wake classification based on observed vortex positions [19].....	133



## LIST OF SYMBOLS

$A$	: Wake width (approximated as $2h_{max}$ )
$b$	: Half-span
$c$	: Chord length
$s$	: Span
$\alpha_0$	: Mean angle of attack
$f$	: Flapping frequency
$k$	: Reduced frequency
$h$	: Non-dimensional plunge amplitude
$\alpha_1$	: Non-dimensional pitch amplitude
$z_1$	: Dimensional plunge amplitude
$\nu$	: Fluid kinematic viscosity
$\mu$	: Absolute viscosity of the fluid
$U_\infty$	: Free stream velocity
$M_\infty$	: Free stream Mach number
$a_\infty$	: Local speed of sound
$\rho_\infty$	: Free stream density
$\gamma$	: Ratio of specific heats
$R$	: Gas constant
$T$	: Temperature of the fluid
$P$	: Pressure of the fluid
$\rho$	: Density of the fluid
$T$	: Temperature of the fluid
$Re$	: Reynolds number
$St$	: Strouhal number
$C_p$	: Power coefficient
$C_T$	: Thrust coefficient
$C_f$	: Skin friction coefficient
$\eta_P$	: Propulsive efficiency
$\varphi$	: Phase angle between the pitching and plunging motion
$\delta$	: Boundary layer thickness
$\tau_w$	: Wall shear
$L$	: Lift force
$D$	: Drag force
$M$	: Moment force
$C_L$	: Lift coefficient
$C_D$	: Drag coefficient
$C_M$	: Moment coefficient



## **THREE-DIMENSIONAL ANALYSIS OF THE FLOW AROUND AN OSCILLATING FLAT-PLATE**

### **SUMMARY**

Recently, flapping-wing aerodynamics has generated a great deal of interest and an important research effort is being made due to its potential application to Micro-Air Vehicles. The low speed and small aspect ratios generate low Reynolds number flows that are still not well understood. The objective of this study was to perform three-dimensional CFD (Computational Fluid Dynamics) analyzes of the flow developing around an oscillating flat-plate. The commercial software Fluent was used to carry out the computations based on the Reynolds Averaged Navier-Stokes (RANS) equations.

The aim was to highlight the three dimensional flow structure and the effect that some of the kinematics parameters have on the flow and performance parameters. To account for the unsteady flow features a turbulence model had to be incorporated. The  $k\omega$ -sst model was chosen as it includes a treatment of low-Reynolds number flows and proved to provide reliable results for these types of flows. A near-wall modelling approach was adopted since the flow had to be properly resolved throughout the viscosity-affected region.

The Reynolds number was fixed to 60 000 and the parametric studies consisted in varying the aspect ratio of the flat-plate, the mean flow angle, the amplitude ratio and the reduced frequency, independently from one another. The results highlighted the presence of an excessive amount of separation, resulting mainly in drag-producing motions. The tip vortex played a positive role by controlling and limiting the spreading of the leading-edge vortex (LEV) to the downstream. It is by increasing the reduced frequency that a thrust-producing configuration was achieved, for which a stronger tip vortex developed and the amount of separation was considerably reduced.



## SALINIM YAPAN DÜZ LEVHA ETRAFINDAKİ ÜÇ-BOYUTLU AKIŞIN ANALİZİ

### ÖZET

Son zamanlarda, kanat-çırpma aerodinamiği büyük bir ilgi toplamış ve mikro-hava taşıtlarına uygulanabilirlik açısından büyük bir potansiyel teşkil ettiğinden, konu üzerindeki araştırmalar yoğunlaşmıştır. Düşük hızlar ve düşük en-boy oranları, halen tam anlaşılammış düşük Reynolds-sayılı akışlar yaratmaktadırlar. Bu çalışmanın amacı, salınım yapmakta olan düz bir plaka etrafındaki üç-boyutlu akışın HAD (Hesaplamalı Akışkanlar Dinamiği) yöntemiyle incelenmesidir. Reynolds Ortalamalı Navier-Stokes Denklemlerinin çözümü için ticari bir program olan Fluent kullanılmıştır.

Hedef, üç boyutlu akış karakteristiklerinin ve bazı kinematik parametrelerin akış ve performans üzerindeki etkilerinin vurgulanmasıdır. Süreksiz akış özelliklerinin çözümlenebilmesi için bir türbülans modelinin kullanılması gerekmektedir. Düşük Reynolds-sayılı akışları da kapsayan bir yöntem olduğundan ve bu tür akışlar için güvenilir sonuçlar verdiği bilindiğinden, k- $\omega$  sst modeli kullanılmıştır. Viskozitenin etkili olduğu bölgelerin düzgün olarak çözümlenebilmesi için duvar kenarı modelli bir yaklaşım uygulanmıştır.

Çalışma boyunca Reynolds sayısı 60 000'e sabitlenmiş, en-boy oranı, ortalama akış açısı, genlik oranı ve indirgenmiş frekans değerleri birbirlerinden bağımsız olarak değiştirilerek parametrik çalışmalar yapılmıştır. Sonuçlar, genel olarak sürüklenme hareketine yol açan hareketlerin aşırı miktarda sınırı tabak ayrılmalarına yol açtığını göstermiştir. Uç vorteksinin (girdap), hücum-kenarı vorteksini kontrol etmek ve dağılmasını sınırlamak suretiyle, aşağı akış üzerinde olumlu bir etkisi vardır. İndirgenmiş frekans değerinin artırılması yoluyla, kuvvetli bir uç vorteksi oluşturulabilmiş, sınır tabak ayrılması büyük ölçüde azaltılmış ve itki meydana getiren bir konfigürasyon elde edilebilmiştir.



# **1. INTRODUCTION TO LOW-REYNOLDS NUMBER FLOWS**

## **1.1 Presentation of the Subject**

### **1.1.1 Motivations and applications of Micro-Air Vehicles**

Over the past decade, Micro Air Vehicles (MAVs) have received an increasing amount of attention in view of potential applications to both the civilian and military markets. MAVs are referred to as flight vehicles with a characteristic length of at most 15 cm which makes them barely detectable to the naked eye. Combined to their low noise and radar cross section, these capabilities make them prime candidates for carrying out surveillance, reconnaissance, communication and detection missions. Once equipped with miniaturized electronic and detector sensor equipment of a total payload mass of less than 18 g, they may be used in numerous situations. Real-time data acquisition collected with the help of cameras for instance can be crucial to hostage rescue, counter-drug operations, or surveillance of urban areas. MAVs outfitted with very small sensors are able to undertake missions such as the sensing of nuclear materials or any type of biological agent. These operations may extend to a very wide range of environments and may have to be carried out in the jungle or the desert for example. Therefore, MAVs should be able to perform in all weather conditions and be equipped with a collision avoidance system. All these requirements may sometimes constitute technical barriers that need to be overcome for MAVs to reach the objectives in terms of performances. In this project we will be focusing on the aerodynamic aspect of the problem as the airfoil section and wing geometry are of major concern while designing MAVs. However, the aerodynamics of small-scale flight is not so well understood since the flow regime of MAVs is very different than for conventional aircrafts. Consequently the particular features and structure of the flow that characterize these scales have not yet been thoroughly studied. Thus, the design methods that have been developed over the past decades are inadequate since the wing aerodynamics affect in turn the static, dynamic and aeroelastic stability of the vehicles. The starting point is therefore to focus on the

flow effects as they constitute a critical point of the design process. This brings us to consider first of all the various types of wing arrangements that can be used.

Three distinct types of configurations are possible which include fixed wings, flapping wings and rotary wings. Each of them present benefits and disadvantages according to the range of Reynolds numbers. The Reynolds number can be defined as the non-dimensional ratio of the inertial and viscous forces. Because of the small length scales involved and an operating speed around 10 m/s, the Reynolds number is very low and typically,  $Re = 10^3 - 10^5$ . Therefore, viscous forces become dominant with respect to the inertial forces, and will have a strong influence on the flow characteristics. Fixed wing MAVs have proved to have deteriorating performances as the Reynolds number drops below  $10^5$ . For this reason, this class of MAVs usually flies within the upper range of Reynolds numbers around  $10^5$ . An example for the design of fixed-wing vehicle is given on Figure 1.1 a).

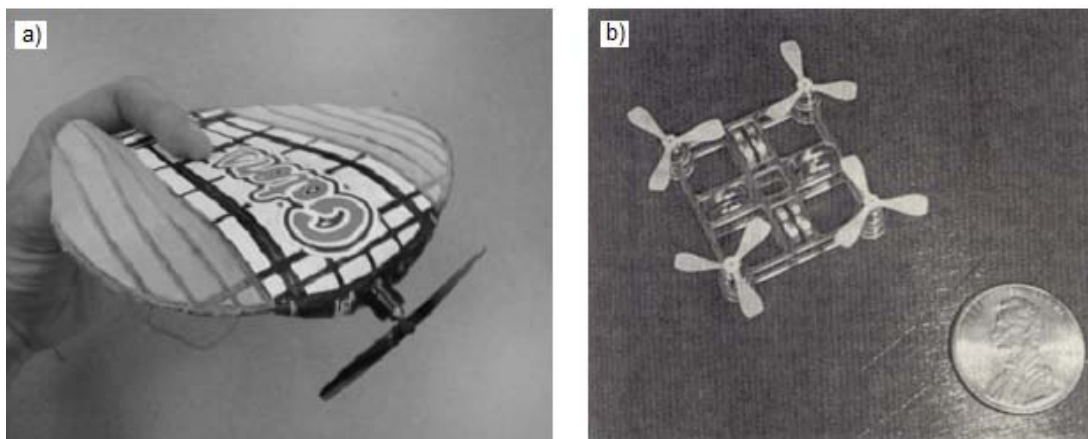


**Figure 1.1 :** a) Fixed-wing MAV [1] b) Rotary-wing MAV [2]

Rotary-wing MAVs are usually used to fly at Reynolds numbers around  $10^4$ . These present key advantages compared to the other two due to their ability to hover, allowing them to evolve vertically and remain in a still position. This can be a huge advantage in many circumstances as their manoeuvrability exceeds by far the other classes of vehicles. In many imaging applications for instance, the limitations of conventional wing configurations on the minimum flight speed are problematic. In addition to the flexibility of their flight-path, rotary wings are less sensitive to crosswind gusts and therefore more stable. However, due to poor aerodynamic efficiency of the rotor, the power requirements are very hard to achieve. This is due to the degradation of the airfoil performances related to low Reynolds number



effects, such as flow separation at low incidences. As a result, the power output reached by rotary-wing MAVs is much lower than for full-scale helicopters. On Figure 1.1 b) an example of rotary-wing design is given. This MAV was named mesicopter, referring to its very small scale made obvious on the picture by the comparison with a coin. Indeed, the thrust required by the rotor in order to maintain level flight is equal to the vehicle's weight whereas for a vehicle in forward flight it is substantially less due to the lift generated by the wing. The aim in this study conducted by Kroo [2] was to diminish the differences in terms of power requirement by reducing the scale of the vehicle.

These considerations bring us to consider the flapping wing design which is of interest in this study. The increasing research effort is motivated by the fact that a small scale flapping wing, compared to a fix wing model offers unique aerodynamic advantages. We recall that the earliest flight trials were highly inspired by birds. However, Sir George Cayley in 1799 put an end to the flapping wing concept by introducing the model based on a fixed wing airplane equipped with a propulsive system. The flapping wing studies became secondary and the main focus was to develop human-carrying airplanes based on this new approach. Nevertheless, research on flapping wing propulsion continued. One of the main points for the aerodynamicists has been to understand how the vortices may increase the lift, thrust and efficiency. Solutions to these problems can first of all be obtained by using different sophisticated numerical approaches, such as computational fluid dynamics or also inviscid panel methods that impose some vortex behaviour. Secondly, to further understand the aerodynamic behaviour of flapping wing creatures, experimentalists are reproducing them and building mechanical replicas. These models allow the scientists to observe the vortex shedding process by means of non-intrusive visualisation methods. More precisely, the vortex structure and scale of an unsteady airfoil has been observed and the flapping wing aerodynamics better understood, such that the challenging problem in mimicking these complex mechanisms could start to be possible.

The fundamental advantages that this configuration shares with rotary wings, is that lift and thrust may be generated with a reasonable size and weight. Indeed, it is thought that approaching the agility and endurance of birds and insects is possible by adopting a flapping wing mechanism, defined as a combination of pitching and

plunging. This is motivated by the fact that flapping wings may offer unique aerodynamic advantages over fixed wings, as they are able to generate propulsion and lift without any additional propulsive device. These unique attributes lead us to further explore the unsteady aerodynamic features that provide these advantages over fixed wing designs.

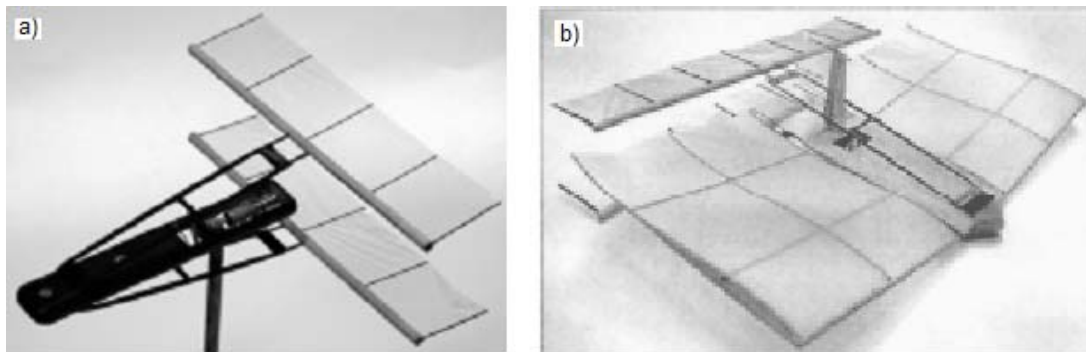


**Figure 1.2 :** a) Flexible-flapping wing [3] b) Bi-plane configuration of a flapping wing [4]

Animal flight analyzes have highlighted the complexity of the wing movement, which may include spanwise wing folding as a consequence of muscle actuation. This additional complexity has up to now only been useful in the case of animal flight mimicking. We will focus on a simplified oscillating rigid-wing. In reality, bird or insect wings are flexible which affects the separation and transition positions [5]. Although there is growing interest in understanding the physics of flexible wing flapping, it is for the moment mainly limited to the use of membranes in fixed wings. On Figure 1.2 a) is represented a model for which the plunging motion is imposed whereas the pitching mode is implemented passively thanks to the flexible wings. As a result from this degree of flexibility, the thrust and efficiency were increased. These improvements are due to the ability of flexible wings to facilitate passive shape adaptation. This results in delayed stall as membrane wings stall at much higher angles of attack. However, to simulate the flow over a flexible surface a structural model will need to be coupled to the Navier-Stokes equations in order to model the transient behaviour of the flexible surface which considerably adds complexity to the problem. Finally, more complex arrangements have been designed that combine different types of configurations as illustrated on Figure 1.2 b). Here, the thrust is provided by the flapping-wings in bi-plane arrangement at the back of the vehicle. These are mounted very close to the fixed wing that provides the

required lift. To conclude we may say that this project solely focuses on the aerodynamic properties of the flow that develops around a rigid flapping wing. We will now present the objectives of the study that is based on a CFD analysis of the flow past an oscillating three-dimensional wing.

### **1.1.2 Challenges and objectives**

We will see later that although the shedding process allowing the generation of thrust is essentially an inviscid phenomenon, at low Reynolds numbers the viscous effects cannot be neglected as the propulsive efficiency greatly depends on them. The boundary layer thickens due to the high viscous forces and remains laminar over the majority of the surface. At higher angles of attack, the flow decelerates due to the adverse pressure gradients it encounters. The flow near the surface becomes very sensitive to the shear stress. Because of the absence of momentum transfer in between the layers, the flow may then separate in the leading edge region. Generally, the laminar boundary layer soon reattaches as a turbulent boundary layer. As a result of the transition from laminar to turbulent, a laminar separation bubble appears, usually located near the leading edge. As the wing oscillates this LEV is utilized by insects for instance to increase the efficiency of lift and thrust generation. The LEV is the defining characteristic of flapping wing aerodynamics. As our study will be numerical, we should insist on the fact that prediction of the separation and transition plays a critical role in determining the development of the boundary layer. In turn this affects the aerodynamic performance of the wing so we may conclude that properly dealing with the sensitive boundary layer is essential to design a vehicle at low Reynolds numbers.

MAV wings are also characterized by low aspect ratios that usually do not exceed 4. Consequently, the flow past the finite wing is highly influenced by the wing tip vortex that forms on the upper surface for positive lift. In general we may say that tip vortices are of major concern in aeronautical applications due to their drag contribution at low speeds and unexpected effects on aircraft safety. Indeed, the process of tip vortex formation is extremely complicated because of the flowfield being turbulent and three-dimensional. It is caused by the mixing at the wing tip of the high and low pressures of the two surfaces. In addition, the pressure change at the tip affects the spanwise lift distribution. A few studies have focused on these three-dimensional effects and in general it has been found that the efficiency is

overestimated in 2D as the tip vortices lead to a loss in energy. We may conclude by saying that the three-dimensional flows around flapping-wings are significantly more complex than in the simplified two-dimensional case as the wing tips greatly modify the wake flow.

The objective of this project consists in solving computationally the flow around a finite flapping wing. The flat-plate geometry has been chosen in common with other experimental studies. Indeed, it can be very valuable to later compare the two sets of results. The aim will be to make use of the experimental data once available, in order to validate the numerical approach. We may add that CFD analyzes have been rarely conducted in this range of Reynolds numbers. The final objective is to later consider Computational Fluid Dynamics as a valuable tool to investigate the flow experienced by Micro-Air Vehicles.

The current aim is not only to perform a computational validation of low Reynolds number flows but also to thoroughly investigate the complex three-dimensional flow structure. Indeed, low Reynolds number flows are well understood from a theoretical point of view but not as well from a computational perspective. In order for the flow solver to gain credibility we must insure that the flow physics are correctly represented. Determining the forces on the wing will be sufficient to characterize the performance. Results for several mean flow angles of attack will be compared. The wing's spanwise dimension will be modified in order to study the impact of the aspect ratio on the solution. Finally, we will also perform a parametric study. Several of the flapping parameters will vary within a range allowing us to deduce their effect on the flow structure and performance parameters.

### **1.1.3 Organization**

We will introduce the subject of this thesis by briefly presenting the flow physics, while giving particular attention to the low Reynolds number effects and the three-dimensional effects. Preceding the treatment of the underlying flow physics, we will give the critical parameters related to the oscillatory motion. In addition to the flapping parameters that define the flapping motion itself, the performance parameters that are used to judge the efficiency reached by the vehicle while generating thrust will also be discussed. These are based on the aerodynamic coefficients that we will also present to complete this section. Once all the

terminology useful to the subject and the physics related to low Reynolds number flows is presented, we will summarize the important historical developments that were achieved and the critical results obtained in previous works. We will mainly focus on numerical studies which have most of the time been carried out in two-dimensions, sufficient to investigate the effect of the kinematics parameters. However, a few studies have been three-dimensional which will help us to gain deeper insight into the 3D effects before starting our own computations.

In the second chapter of the thesis, the methodology that we have applied to conduct the CFD analysis of the flow around the oscillating flat-plate is presented. It is composed of several steps, from the grid generation to the preparation of the simulation. The method employed for creating the mesh surrounding the rectangular flat-plate is presented in detail. The assumptions allowing the problem to be simplified are discussed as the computational effort required to solve the unsteady three-dimensional flow needs to be limited as much as possible. The governing equations are given along with a brief introduction to the Finite Volume method. The simulation parameters are fixed according to the requirements imposed by low Reynolds number flows. Particular attention is given to the modeling of turbulence and to the near-wall approach necessary to accurately capture the unsteady aerodynamic features.

In the last chapter, the results obtained from the computations are given. As a preparation to the simulations, a mesh sensitivity analysis was conducted. Once the overall mesh density was considered suitable, the kinematics of the flapping motion was verified and the appropriate time step determined. The calculations are post-processed by examining the aerodynamic coefficients and other flow properties.

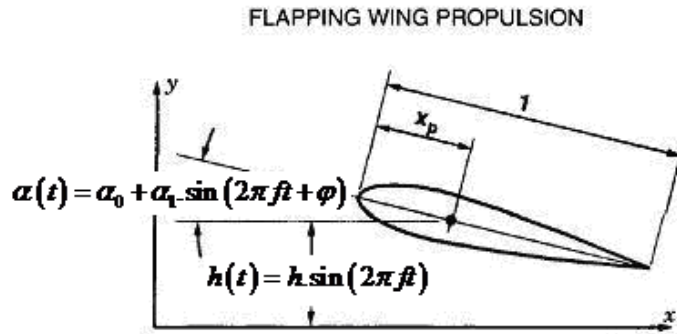
## **1.2 Governing Parameters of the Flow and Flapping Motion**

### **1.2.1 Critical parameters of oscillating airfoils**

We wish to identify the critical parameters useful in the study of flapping-wing aerodynamics, first of all by fully defining the flapping motion. In this section we will also highlight the objectives as far as the performance of the MAVs is concerned, that represent the critical parameters to be optimized.

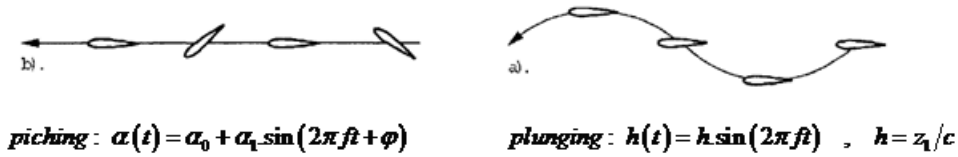
### 1.2.1.1 Kinematics

Figure 1.3 illustrates the two degree of freedom motion prescribed to a flapping airfoil. We will be applying both the plunging and pitching movements sinusoidally with a frequency  $f$ .



**Figure 1.3 :** Two-degree-of-freedom motion

The two movements are illustrated below on Figure 1.4 along with the equations governing the kinematics:



**Figure 1.4 :** Two-degree-of-freedom motion

These two are limited by the pitch and vertical plunge amplitudes, denoted as  $\alpha_1$  and  $h$  respectively.  $h$  is the ratio of the plunge amplitude  $z_1$  and airfoil chord  $c$ , and is therefore non-dimensionalized. The angle  $\alpha_0$  corresponds to the mean angle of attack between the airfoil and the incoming free-stream. We notice that the pitching motion imposes a sinusoidal oscillating movement to the airfoil for which a pitching axis needs to be defined. On the above figure, it is denoted as  $X_p$  that represents the pivot location from the leading edge, again with respect to the chord  $c$ . In addition, it has been proved that shifting one of the motions in time compared to the other has a significant impact on the critical parameters we wish to optimize. Therefore, a phase angle  $\varphi$  is introduced in the equation that describes the pitching motion. If this angle is positive we say that the pitching is *leading* the plunging by an angle  $\varphi$ .

### 1.2.1.2 Flapping parameters

One of the key parameters is the non-dimensional reduced frequency that is defined as follows:

$$\text{reduced frequency: } k = \frac{\pi fc}{U_\infty}, \text{ Strouhal number: } Sr = \frac{fA}{U_\infty} \quad (1.1)$$

However, since the flow fields that develop around a flapping airfoil are usually wake-dominant flows, the Strouhal number is often taken into account. As a reference length it uses the wake's width instead of the chord, where  $A$  is the oscillatory amplitude of the trailing edge. It has a very similar meaning that of the reduced frequency.

Among the simulation parameters, we will often encounter the product of the reduced frequency and plunge amplitude  $kh$ . It represents the maximum non-dimensional flapping velocity. It can be related to the Strouhal number as follows:

$$kh = 2\pi (a/A) Sr \quad (1.2)$$

Both the Strouhal number and the value of  $kh$  indicate the angle of attack that is induced by the flapping motion. Indeed, we have:  $\alpha_1 = \arctan(kh)$

### 1.2.1.3 Thrust generation

The purpose of flapping wings is to produce a forward thrust while simultaneously supporting the weight. The amount of thrust is measured in terms of the mean thrust coefficient defined as follows:

$$\text{mean thrust coefficient: } C_{Tmean} = -\frac{1}{T} \int_t^{t+T} C_D(t) \cdot dt \quad (1.3)$$

It is very important that the wing produces thrust in an economic way. Therefore, it has to minimize the drag penalty as well as mechanical losses, which are the counterpart of thrust optimization. Consequently, it is crucial to also account for the efficiency of the airfoil.

#### 1.2.1.4 Propulsive efficiency

One of the key objectives is to minimize the power consumption of flapping wings under optimum conditions. It has been shown [6] that the mechanical power output for steady level flight follows a U-shaped curve. This quantity corresponds to the rate of increase of the kinetic energy of the air caused by the passage of the wing. In the case of birds, the speed is controlled by variation of the wingbeat frequency and amplitude. Considering that the work required for flight is related to the flight muscles controlling the movement of the wings, the efficiency of bird flight is expected to vary with the speed flight. At the contrary, it can be possible to maintain efficiency for an MAV by respecting some design constraints on the actuators responsible for the wing movement. The measured performance criteria representing the propulsive efficiency, is defined as the ratio of the power output to the power input. It is given by:

$$\eta = \frac{\text{power output}}{\text{power input}} = \frac{TU_{\infty}}{P} = \frac{C_T}{C_P} \quad (1.4)$$

The power output corresponds to the product of the thrust and free stream velocity and the power input is the time rate of work done to the wing. The propulsive efficiency can be put into a non-dimensional form and becomes the ratio of the thrust coefficient to the power coefficient. The most important loss is by far the work that is necessary to harmonically accelerate the mass of the wings at high frequencies. This is when the observation of the natural movement can be crucial to diminish these losses. Indeed, it has been observed that birds use aerodynamic forces by making minor pitch and camber changes in order to facilitate the acceleration process.

We may conclude by saying that a compromise between thrust generation and efficiency needs to be reached, according to the requirements in terms of performances. Indeed, these depend on the type of mission the MAV is most lightly to be carrying out. Considering extreme cases, if a high degree of maneuverability is required then the amount of thrust available needs to be maximized. At the contrary if the vehicle is to mainly evolve in forward flight, it is the efficiency that needs to be optimized. Therefore, the efforts should be orientated towards satisfying these priorities such that appropriate wing design and kinematic parameters are determined.



## 1.2.2 Non-dimensional parameters

Non-dimensionalized flow characteristics allow us to compare results under the same dynamic conditions, whether they are numerical or experimental even though these are collected for different scale models. However, the scale effect is to be eliminated. The non-dimensionalization of the Navier-Stokes equations leads to two key non-dimensional parameters, namely the Mach number and the Reynolds number.

### 1.2.2.1 Mach number

The free-stream Mach number  $M_\infty$  relates the free-stream velocity  $V_\infty$  to the local speed of sound  $a_\infty$  as follows:

$$M_\infty = \frac{V_\infty}{a_\infty}, \quad \text{speed of sound} \rightarrow a_\infty = \sqrt{\gamma RT_\infty} \quad (1.5)$$

where the local speed of sound is defined in terms of  $\gamma$  the ratio of specific heats of the fluid,  $R$  the gas constant and  $T$  the temperature of the fluid. The Mach-number is a dimensionless value that is used to analyze fluid flow dynamics problems. It indicates the significance of the compressibility effects and characterizes the flow regime. Applied to MAVs, the operating speeds are relatively low, therefore so will be the Mach number. It is necessarily smaller than 0.3 for which the density changes are usually negligible. Consequently, the subsonic flow ( $M_\infty < 1$ ) can be treated as incompressible.

### 1.2.2.2 Reynolds number

The Reynolds number  $Re$  is a non dimensional parameter that relates the viscous and inertial forces as follows:

$$Re = \frac{\rho_\infty V_\infty c}{\mu} \approx \frac{\text{Inertial forces}}{\text{Viscous forces}} \quad (1.6)$$

where  $c$  is the chord length taken as a reference,  $\rho_\infty$  and  $V_\infty$  are the free-stream density and velocity respectively and  $\mu$  the absolute viscosity of the fluid. Considering that for MAVs both the chord length and the flight velocity are relatively small, the flight regime under consideration is characterized by a low-

Reynolds number. From these observations we deduce that the viscous forces dominate which results in a relatively thick boundary layer.

To allow comparison, it is essential that the scale effect is suppressed. For the boundaries of the flow to be close to identical, a constant ratio has to be conserved in between the characteristic quantities of the two arrangements. Thus, this principle needs to be applied not only to the model's dimensions but to the flow properties as well. If the flow is not exactly similar but only approximately, the information becomes unreliable. A 'scale effect' exists and must not be underestimated. The first assumption was to assume that none of the physical properties of the fluids has any influence on the shape of the flow pattern or on the fluid forces, despite the density of the fluids. Therefore, the mass force of the particles is the only force and needs to be equalized. Indeed, for a viscous flow, it is arranged so that the pressure forces and viscous forces are in equilibrium with the mass force. To obtain the criterion for the similarity of flows, two of the three forces need to be changed by an identical ratio (mass and viscosity forces), in order to maintain equilibrium. The mass forces are changed in the ratio  $\frac{\rho_2 V_2^2 l_2^2}{\rho_1 V_1^2 l_1^2}$  and the viscous forces with  $\frac{\mu_2 V_2 l_2}{\mu_1 V_1 l_1}$ . Hence the condition for an exact model test is:

$$\left( \frac{\rho_2 V_2^2 l_2^2}{\rho_1 V_1^2 l_1^2} = \frac{\mu_2 V_2 l_2}{\mu_1 V_1 l_1} \right) \Rightarrow \frac{V_1 l_1 \rho_1}{\mu_1} = \frac{V_2 l_2 \rho_2}{\mu_2} \Leftrightarrow \text{Re}_1 = \text{Re}_2 \quad (1.7)$$

The equality of the two Reynolds numbers ensures the dynamic similarity of the flows. It is only if in addition the two bodies are geometrically similar that the similarity is perfect.

### 1.2.2.3 Amplitude ratio

The amplitude ratio corresponds to the non-dimensional ratio of the pitching and plunging amplitudes:

$$\lambda = \frac{\alpha_1}{2k \cdot z_1/c} \quad (1.8)$$

This parameter is often given along with the non-dimensional plunge amplitude  $h$  such that the pitching amplitude can be deduced since the reduced frequency  $k$  is

necessarily known. It is a comparative parameter that gives us an idea of the importance of the motions with respect to each other, in terms of amplitudes.

#### 1.2.2.4 Aspect ratio

Figure 1.5 below represents a wing viewed from the top looking down on the wing. The ends of the wing are called the wing tips and the distance from one tip to the other is called the span  $s$ . The wing geometry does not present any sweep just like the flat-plate we will be modeling. Indeed, for a rectangular wing the chord length remains constant along the span.

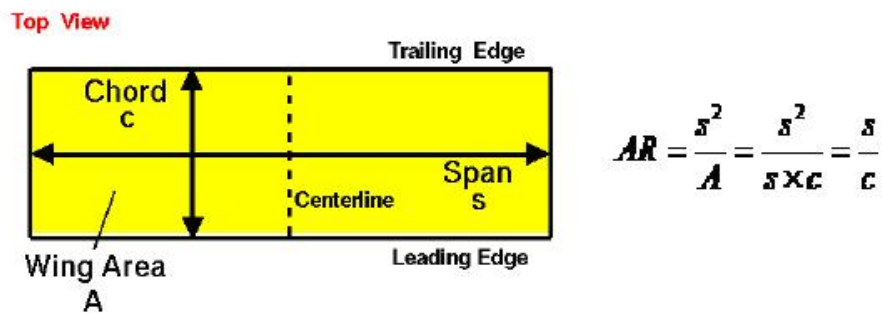


**Figure 1.5 :** Wing planform and aspect ratio

The planform corresponds to the shape of the wing when viewed from above looking down onto the wing. The wing area  $A$  is bounded by the leading and trailing edges and the wing tips. It is defined as the projected area of the planform. The Aspect ratio  $AR$  of a wing is defined as the square of the span divided by the wing area.

### 1.3 Flow-Physics of Low Reynolds-Number Flows

#### 1.3.1 Shear stress and boundary layer separation

As we mentioned in the introduction, at low-Reynolds numbers the performance of the airfoils rapidly deteriorates due to boundary layer separation. The Aerodynamic efficiency is defined as the lift to drag ratio  $(C_L/C_D)_{\max}$  and for three-dimensional wings it is less than for airfoil sections when the aspect ratio is less than 2. For these reasons the airfoil section and wing planform are a critical part of the design procedure. It has been proved that in these regimes where the Reynolds number is less than  $10^5$ , thick airfoils (above 6%) present significant hysteresis in the lift and drag forces due to laminar separation and transition to turbulent flow. Furthermore, to reach higher values the wings must imitate bird and insect airfoils and be very fine

with a small amount of camber. The aim in this section is to discuss the formation of the separation bubble and its effect on the flow. To do so, we should first of all introduce the concept of boundary layer, in conjunction with the notion of shear stress as it leads to the separation of the boundary layer.

In reality, when fluid particles come close to the surface their velocity slows down due to the viscous friction. Viscosity is a physical property that affects stresses of a fluid due to fluid motion. In the case of a viscous fluid flowing past a body, it adheres to the body surface and frictional forces retard a thin layer of fluid adjacent to the surface. The velocity then becomes a function of the distance from the surface and it is only at a certain distance that it is equal to the free-stream velocity. The distance ( $\delta$ ) required by the fluid to reach 99% of  $U_{\infty}$ , is known as the boundary layer thickness and is represented on Figure 1.6 a). As a result, the velocity inside the boundary layer is less than the velocity at its outer edge. The existence of this velocity deficit is a necessary condition for separation. At the outer edge of the boundary layer viscous forces are negligible, and there is an exact balance between inertia and pressure gradient, as expressed by the Bernoulli equation. In the case of an airfoil, the curvature of the top surface caused by the angle of attack forces the flow to first accelerate around the leading edge and then decelerate.

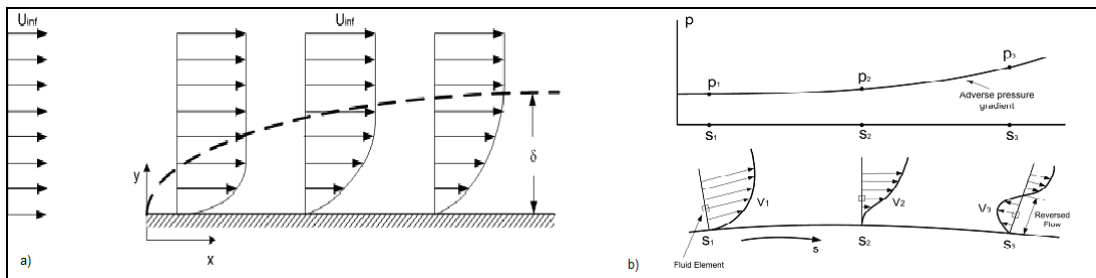


**Figure 1.6 :** a) Boundary layer thickens  $\delta$  b) Flow separation

While the pressure increases as the particle moves downstream, it is accompanied by a decrease in velocity. The inertia of the particles near the wall may not be sufficient to overtake the pressure forces, causing the velocity vector to change direction. This velocity deficit indicates separation. Figure 1.6 b) illustrates the different stages leading to separation. As we can see, the process can only be initiated by a sufficiently strong adverse pressure gradient. On the schema, it first increases up to an inflection point known as the separation point. The wall shear stress is exactly zero. As the unfavourable pressure gradient increases, the velocity gradient at the

wall decreases and may become negative indicating the occurrence of reversed flow. The boundary layer has detached from the surface, resulting in a region of recirculating flow.

They are two types of boundary layer represented on Figure 1.7 a) which can either be laminar or turbulent with a transition phase in between. Laminar boundary layers are relatively thin and are characterized by low levels of mixing between the adjacent layers. At the contrary, turbulent boundary layers are quite thick and present significant mixing in between the layers.

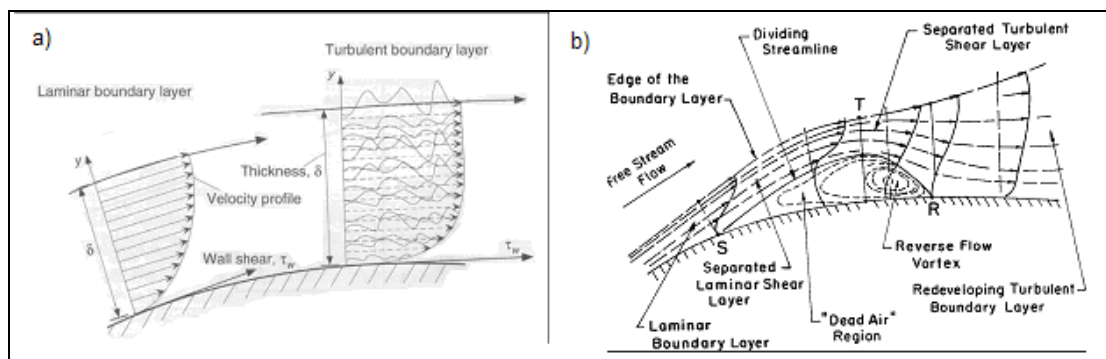


**Figure 1.7 :** a) Boundary layer profiles [7] b) Transitional separation bubble (Horton 1968)

Due to the important viscous effects, the boundary layer is very lightly to separate and form a shear layer as it is very sensitive to the shear stress because of the absence of mixing. At Reynolds numbers greater than 50 000, transition from laminar to turbulent takes place within the shear layer and if there is enough energy it may reattach to the surface. A region of recirculating flow forms, often referred to as a transitional separation bubble since it causes the boundary layer to trip. At low Reynolds-numbers, the bubble can be relatively long and cover from 15 to 40% of the airfoil's surface. This phenomena is illustrated on Figure 1.7 b). At Reynolds numbers below 50 000, the separated shear layer does not always reattach. An accurate prediction of the existence and extent of the separation bubble is crucial to the design of low-speed wings.

The shear stress is the physical force that resists to the flow and tends to slow it down. It is tangential to the surface and is related to the absolute viscosity  $\mu$  of the fluid as follows:

$$\tau = \mu \cdot \left( \frac{\partial u}{\partial y} + \frac{\partial v}{\partial x} \right) \quad \rightarrow \quad \tau_w \approx \mu \cdot \frac{\partial u}{\partial y} \quad \text{at : } y = 0 \quad (1.9)$$

It can be approximated at the wall by  $\tau_w$ , represented on Figure 1.7 a) above. The local shear stress varies in the chordwise direction, and it is convenient to define the dimensionless skin friction coefficient as follows:

$$C_f = \frac{\tau_w}{1/2 \cdot \rho_\infty V_\infty^2} \quad (1.10)$$

We will now see that the skin friction plays an important role in the aerodynamic properties of an airfoil as the shear stress greatly contributes to the lift and drag forces, especially at low Reynolds numbers.

### 1.3.2 Aerodynamic coefficients

The forces and moments of a wing are obtained by integrating the local values of pressure and shear stress acting on the surface of the wing. The two components, related to pressure and friction, are added to obtain the total forces and moments. Once again these are non-dimensionalized in order to bring the values back to a known scale of reference. In addition, the coefficients can then be compared to other values obtained in the same conditions. The coefficients for lift  $C_L$ , drag  $C_D$  and moment  $C_M$  are defined on Figure 1.8 where the lift, drag and moment forces are denoted as  $L$ ,  $D$  and  $M$  respectively.

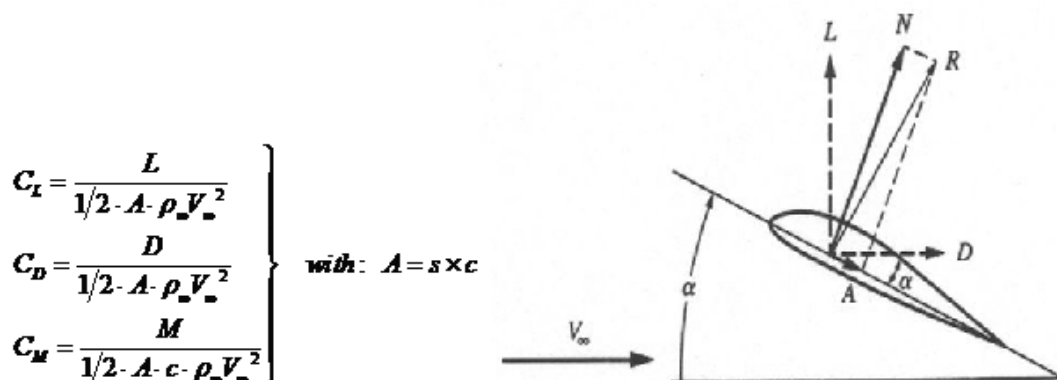


**Figure 1.8 :** Definition and representation of the aerodynamic coefficients

We will now give a few explanations about the origin of these quantities. First of all we should state that a wing's aerodynamic force may be separated into lift and drag

components that intersect with its chord line at the centre of pressure. No aerodynamic moments exist at the centre of pressure since the line of action of the aerodynamic forces passes through this point. The moment measures the tendency of the wing to rotate about its centre of gravity, under the action of the aerodynamic forces. Let us explain the origin of the two pressure and viscous components of the lift and drag forces, by taking the total drag force as an example. As fluid flows past a wing, it will tend to drag it along in the direction of fluid flow which slows it down. The drag comprises two components, the first one being the pressure drag. It is based on the pressure difference between the upstream and downstream surfaces of the wing, and corresponds to the resultant of resolved forces normal to the surface of the wing. The second component, namely the skin friction drag, results from the viscous shear of the fluid flowing over the surface of the wing. It is the resultant of resolved forces tangential to the surface. The total drag on the wing is known as the profile drag and is the sum of the pressure and skin friction drag. Let us formulate the procedure allowing us to calculate the lift and drag forces. The first step is to calculate the pressure (*press*) and skin friction (*skin*) forces in the normal (*n*) and tangential (*t*) directions:

$$\left. \begin{aligned} F_{press\_t} &= \iint_{wing} P \times n_{wing} [X] \quad , \quad F_{skin\_t} = \iint_{wing} X_{shear} \\ F_{press\_n} &= \iint_{wing} P \times n_{wing} [Y] \quad , \quad F_{skin\_n} = \iint_{wing} Y_{shear} \end{aligned} \right\} \begin{aligned} F_t &= F_{press\_t} + F_{skin\_t} \\ F_n &= F_{press\_n} + F_{skin\_n} \end{aligned} \quad (1.11)$$

In correspondence to Figure 1.8 above, the tangential and normal forces are referred to as *A* and *N* respectively. By combining these two, the resultant force *R* is obtained. The drag and lift are the projection of *R* along the horizontal and vertical axis respectively, thus depending on the angle of attack of the airfoil with respect to the incoming flow. The lift and drag can be obtained directly to the tangential and normal forces and inversely:

$$\left\{ \begin{aligned} L &= -F_t \cdot \sin \alpha + F_n \cdot \cos \alpha \\ D &= F_t \cdot \cos \alpha + F_n \cdot \sin \alpha \end{aligned} \right. \quad \left\{ \begin{aligned} F_n &= L \cos \alpha + D \sin \alpha \\ F_t &= D \cos \alpha - L \sin \alpha \end{aligned} \right. \quad (1.12)$$

This is the procedure we will later adopt in order to obtain the performance parameters as they are based on the aerodynamic coefficients. Indeed, the pressure and shear stress will be made available from the CFD analyze. We will now briefly

mention about the dependence of the force and moment coefficients on the flow conditions. The characteristics of the NACA 0012 airfoil are represented on Figure 1.9 for  $Re = 10^6$  and  $M = 0,1$ .

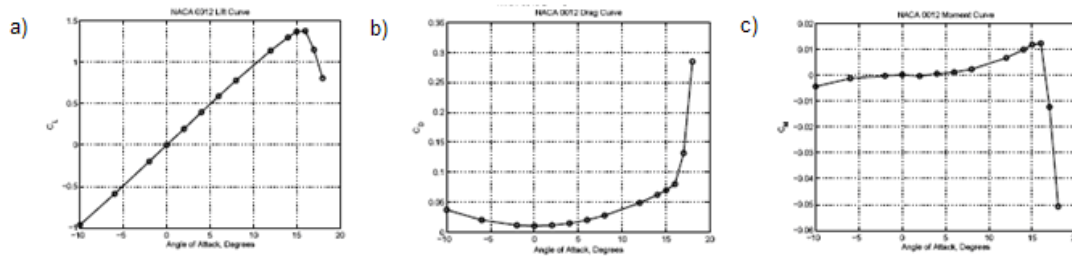


**Figure 1.9 :** Aerodynamic coefficients with respect to the angle of attack a)  $C_L / \alpha$  b)  $C_D / \alpha$  c)  $C_M / \alpha$

Let us consider the variation of the lift coefficient versus the angle of attack on Figure 1.9 a). We observe that when  $\alpha$  increases so does the lift, along with the suction force present on the upper surface, as the flow is accelerating more and more. However, at very high angles the lift suddenly drops, related to the separation of the boundary layer mentioned previously. Around  $\alpha = 16^\circ$  the wing is said to have stalled. Simultaneously we see on Figure 1.9 b) that the drag dramatically increases in the separation region, with a significant contribution coming from the pressure drag. For lower angles, the pressure drag is much less and the skin friction drag dominates. The drag is minimized at zero angle of attack. Finally, on Figure 1.9 c) the behaviour of the moment coefficient is plotted and indicates very well the occurrence of stall. We see that the wing pitches up prior to the boundary layer separation and then dramatically pitches down as the wing stalls due to the sudden loss in lift.

### 1.3.3 Reynolds-number effects

We have already mentioned about many of the Reynolds number effects related to MAVs, however we shall make a summary of their impacts. In the type of applications we are looking into it is clear by now that the small size of the MAVs associated to their low flight speeds, brings us to consider low-Reynolds numbers. Consequently, the viscous effects are much higher than for conventional aircraft applications, resulting in a thicker boundary layer. The shear stress present along the surface is more important and so will be the skin friction. From these statements, we can easily conclude that the skin friction component of the lift and drag forces is



much higher at low Reynolds numbers. In addition, the flow often remains laminar on a large portion of the wing and can degrade the performance of the wing if a long laminar separation bubble appears. Indeed, this is more and more likely to occur as the Reynolds number decreases.

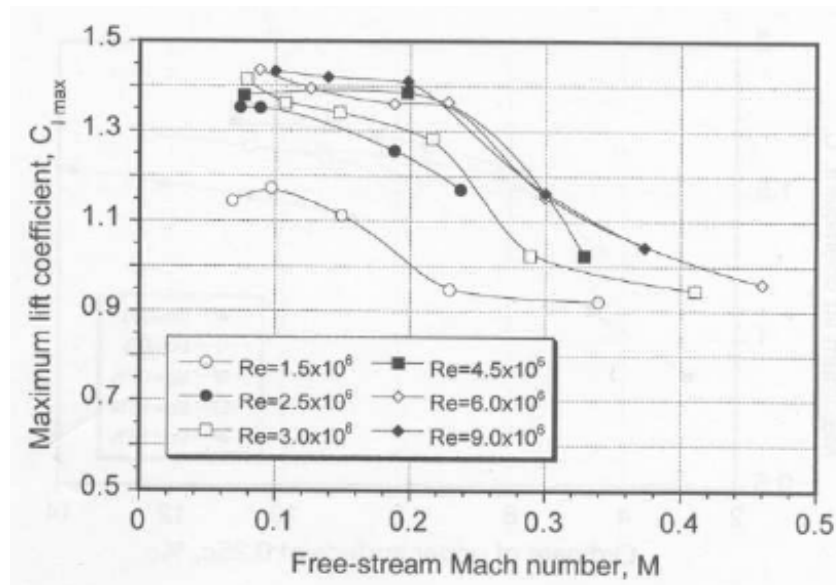


**Figure 1.10 :** Effect of the Reynolds-number on the maximum lift coefficient [7]

On Figure 1.10 above, the maximum lift coefficient for the NACA 64-210 is plotted as a function of the free-stream Mach number for several Reynolds numbers. Its value clearly decreases along with the Reynolds number due to the fact that separation occurs at lower angles of attack. This last observation adds up to the other undesirable effects related to low-Reynolds numbers. The characteristic L/D ratio decreases, showing how flight at low-Reynolds numbers is much less efficient than at higher values since the available power is a limiting factor at small scales.

### 1.3.4 Static and dynamic stall types

#### 1.3.4.1 Static stall

The static stall of a wing is a basic phenomenon which refers to the sudden major loss in lift, increase in drag and change in pitching moment at a specific angle of attack known as the stall angle. We have seen that for low-Reynolds numbers, stall is associated to the separation of the boundary layer due to the viscous effects. It results in a recirculation region on the upper surface, where the pressure is higher than in the

attached flow case, therefore leading to the loss in lift force. These can be of two different types and an airfoil may present stall characteristics of more than one kind.

The *trailing edge stall* is usually associated to thick airfoils. The section is characterized by a leading edge with a large radius of curvature, therefore limiting the amount of suction as well as the negative pressure values along the airfoil. Thus the boundary layer tends to remain attached for reasonable angles of attack. However, as the incidence increases, flow separation may appear close to the trailing edge and move towards the leading edge as the angle further increases. Full-stall is delayed whereas the drag starts to increase significantly well before. This causes the lift curve to flatten due to the progressive reduction of the effective amount of lifting surface. An example of the progression is given on Figure 1.11 a).

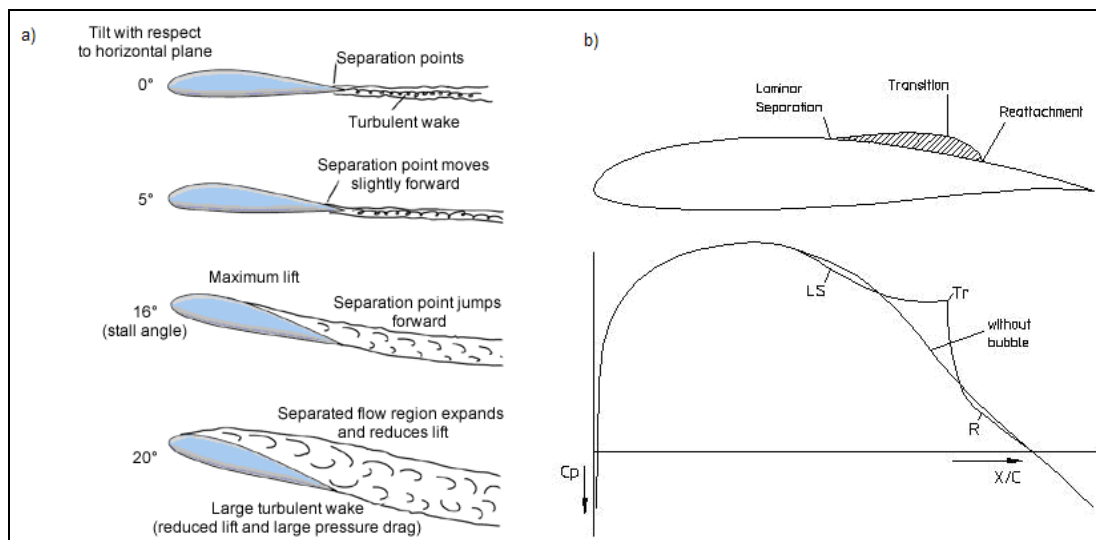


**Figure 1.11 :** a) Progression of the trailing-edge stall b) Reattachment of the LSB

The airfoil may also experience a *leading edge stall* often observed for thinner profiles which present a much smaller radius of curvature at the leading edge. At first, the energy might be sufficient to allow the boundary layer to reattach as turbulent; this situation is illustrated on Figure 1.11 b). As the angle becomes larger, so does the extent of the laminar separation bubble, the reattachment point moves downstream towards the trailing edge. The lengthening of the laminar separation bubble causes the lift slope to flatten. As it further increases the adverse pressure gradient is high enough to prohibit reattachment, at which point the airfoil is fully-stalled. This is known as the ‘bursting’ of the laminar separation bubble and as its name indicated it is a much more abrupt phenomenon.

### 1.3.4.2 Dynamic stall

Unlike for static stall cases, dynamic stall occurs when the airfoil is subjected to an unsteady motion that includes a time-dependent angle of attack. This is typically the case for flapping airfoils. This phenomenon is a non-linear unsteady aerodynamic effect that takes place when the incidence is changing rapidly. The pronounced features of the process are vortex shedding and the delay of stalling. The rapid change causes a concentrated vortex to form in the leading-edge region. The reasons associated to the creation of the vortex will be discussed in detail later while presenting the historical development achieved for flapping airfoils. This vortex then separates and convects downstream over the airfoil. It induces a pressure wave that further increases the lift force and this for an angle superior to the static stall angle. However, once the vortex passes beyond the trailing edge, the lift collapses and the airfoil is back to a normal stall situation. When the airfoil pitches down reattachment is initiated starting from the leading edge to the trailing edge until the flow is fully attached.

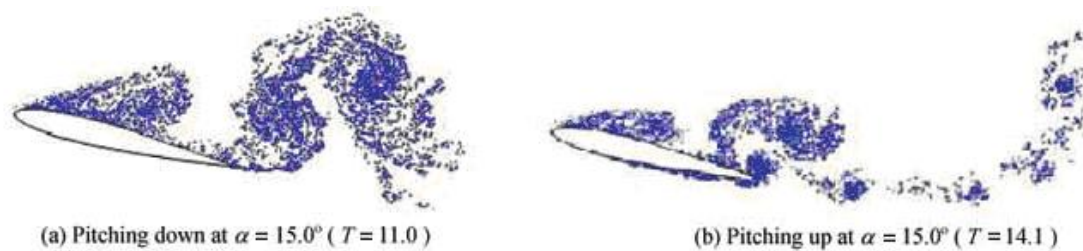


**Figure 1.12 :** Vortex shedding taking place during dynamic stall

This process is repeated periodically, thus creating a vortex shedding pattern as illustrated on Figure 1.12. Dynamic stall can be a way to improve the wing's manoeuvrability since the power available increases with the dynamically induced lift increase. These advantages will be mentioned again as we present results of previous studies in the section of this chapter.

### 1.3.5 Vortex shedding allowing thrust generation

Knoller [8] and Betz [9] in 1909 and 1912 respectively, were the first to observe that a pitching and plunging airfoil creates an angle of attack such that an aerodynamic force is generated. Let us consider Figure 1.13 down below.

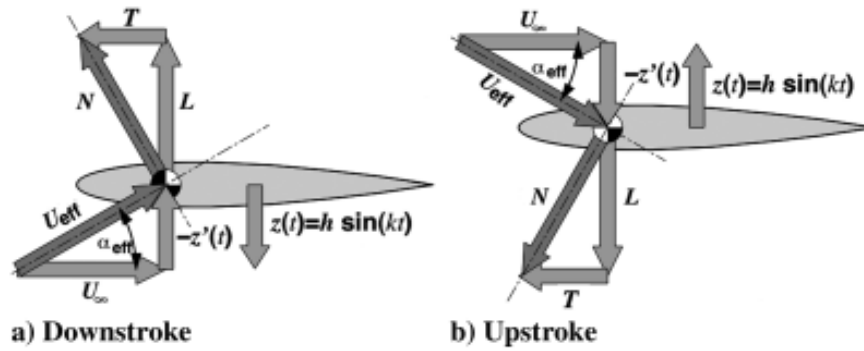


**Figure 1.13** : First theory describing the generation of thrust from a flapping airfoil. They used quasi-steady arguments by considering an airfoil that is flying with the velocity  $U_\infty$  and descending with the velocity  $w$  such that the airfoil acquires a certain incidence with respect to the flow defined by the following angle of attack:  $\alpha = w/U_\infty$ . A pressure difference is created between the upper and lower surfaces of the airfoil that results into the generation of a force  $N$ . It decomposes into lift and thrust components. During both the downstroke and upstroke movements of the wing, positive thrust components are created so that the time averaged thrust force  $T$  is positive. Katzmayr [10], by positioning a stationary wing into a sinusoidal oscillating wind stream, verified the Knoller-Betz effect experimentally in 1922. However, the theory of Knoller-Betz did not take into account the vorticity that is shed into the wake of the airfoil and Birnbaum [11] realized that they had omitted a critical aspect of the flow physics describing airfoil flapping, namely the shedding of starting vortices at the airfoil's trailing edge. By investigating the problem he showed that it was governed by the ratio of two characteristic speeds. He was the first to introduce the similarity parameter  $k$  that we previously defined. A few years later, Birnbaum identified the condition leading to flutter or to thrust generation and suggested an alternative solution to conventional propeller, by the use of a plunging airfoil. In their book, Kuchemann and Weber [12] commented that the propulsive efficiency of a flapping airfoil is much greater than a classic propeller model due to the disadvantageous trailing vortex system that is generated by the propeller.

We now wish to fully understand what is physically occurring when the airfoil's incidence suddenly changes. As the speed or the incidence of an airfoil is modified, a so called starting vortex is formed close to its trailing edge. Let us first consider a symmetric airfoil at zero degrees incidence. On Figure 1.14, the upper and lower boundary layers present clockwise and anticlockwise vorticity respectively.

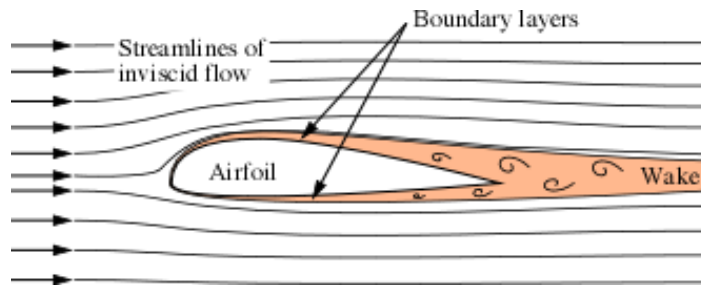


**Figure 1.14 :** Surface and wake vortex sheet

At the trailing edge the two boundary layers merge and form a wake. Whenever the angle of attack suddenly changes, a larger amount of vorticity is created on both the upper and lower surfaces. However, the amounts that up to now were the same between the clockwise and anticlockwise vortices become unbalanced. The change in angle of attack results as we know in lift production but also in a change of circulation bound to the airfoil.

Prandtl [13] is considered to be the pioneer in the field of unsteady low-speed airfoil flows. The approach he presented in 1922 consisted in neglecting the effect of viscosity and therefore to solve the Laplace equation as the governing equation. His study was based on Kelvin's theorem that states that any change in lift has to be accompanied by the detachment of a vortex from the airfoil's trailing edge.

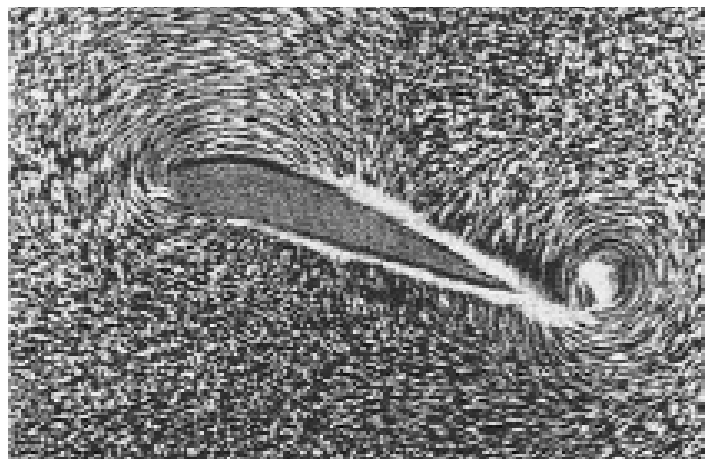


**Figure 1.15 :** Starting Vortex resulting from a sudden incidence change

Indeed, according to the theorem, the total vorticity in the region surrounding the airfoil must remain zero. When the aircraft wing starts moving, it sheds a vortex which therefore leads to the generation of an equivalent circulation of opposite sign that provides the swirl required for the creation of lift. Indeed, if for example a positive angle difference is introduced, the anticlockwise vorticity of the lower

boundary layer dominates for a certain time. After accumulating at the trailing edge, the anticlockwise vortex separates and is shed from the trailing edge. Figure 1.15 above was obtained experimentally and illustrates this phenomenon.

Prandtl pointed out that consequently, any change in lift is necessarily accompanied by a vortex that detaches from the airfoil's trailing edge. In order to solve the incompressible flow past an airfoil subject to small amplitude sinusoidal oscillations, Prandtl used a small perturbation approach therefore limiting the analysis to flat plates, oscillating with small amplitude.

In the following years, Gottingen and Theodorsen [14] at NACA Langley developed solutions for incompressible inviscid flows past thin oscillating airfoils. They were based on Prandtl's original small perturbation proposal, still of great value today. The solution showed to be valid for the complete reduced frequency range.

Based on Theodorsen's flat-plate theory, in 1936 Garrick [15] provided the first numerical prediction of thrust force and propulsive efficiency of oscillating airfoils. His formulations were at first valid for a pure plunge motion and suggested that the thrust is proportional to the product of frequency squared and the plunge amplitude squared. We now know that the airfoil sheds a vortical wake of a certain wavelength. During one oscillation, the vortex shed from the trailing edge travels a distance  $U_\infty/2\pi f$ , such that the reduced frequency also compares the wavelength to the airfoil chord. Figure 1.16 represents the vortical wake for two different reduced frequency values.

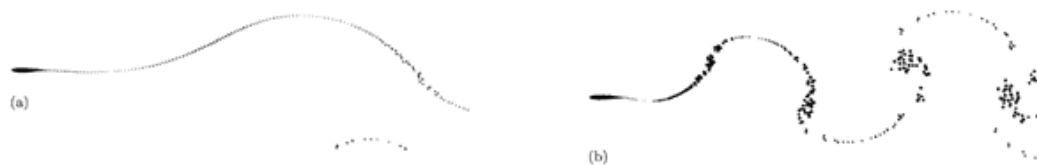


**Figure 1.16 :** Vortical wake induced by sinusoidal plunge oscillation a)  $k = 0.5$  b)  $k = 1.0$

As expected, the higher the reduced frequency, the smaller the wavelength. Indeed, on Figure 1.16 b) the reduced frequency is increased up to 1.0 compared to the first situation where it was equal to 0.5. As the vortical wavelength is reduced to half of its value on Figure 1.16 a), we observe that the unsteadiness of the flow has considerably increased.

In 1935, Von Karman and Burgess [16] modelled the wake of the flow past bluff bodies at low Reynolds numbers, by an infinite row of alternating vortices. Indeed, as we mentioned already, every change in angle of attack will produce a starting vortex that is then shed from the trailing edge. Sinusoidal plunge motion therefore produces a vortex street. This representation is known as a von Karman Vortex Street and led to a theoretical explanation of the generation of thrust and drag by observing the location and orientation of the shed vortices. In a situation where the flow is flowing from the left, the upper row of vortices will rotate clockwise and the lower row counter clockwise. As a result a momentum deficit is introduced in the wake compared to the upstream flow and the airfoil experiences a so called ‘drag producing wake’.

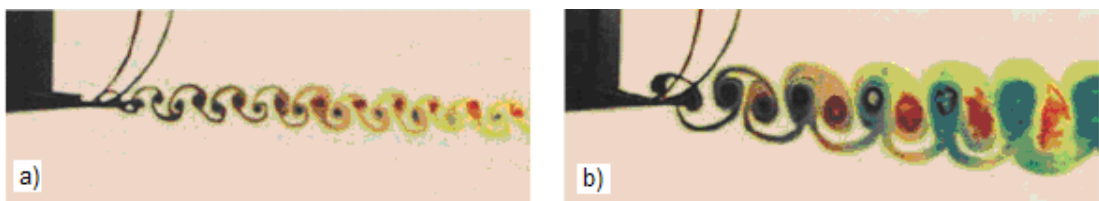


**Figure 1.17 :** a) Drag producing wake for a stationary NACA0012 airfoil b) Thrust producing wake for a NACA0012 airfoil undergoing pure plunging motion

The experimental results collected by Lai and Platzer [17] illustrate the case just described on Figure 1.17 a). In contrast, as the airfoil undergoes a sinusoidal plunging motion it produces a wake in which the upper and lower row of vortices rotate counter clockwise and clockwise respectfully. This introduces a momentum surplus in the wake compared to the upstream flow. Consequently the airfoil is placed in a configuration referred to as a ‘thrust producing wake’ as illustrated on Figure 1.17 b).

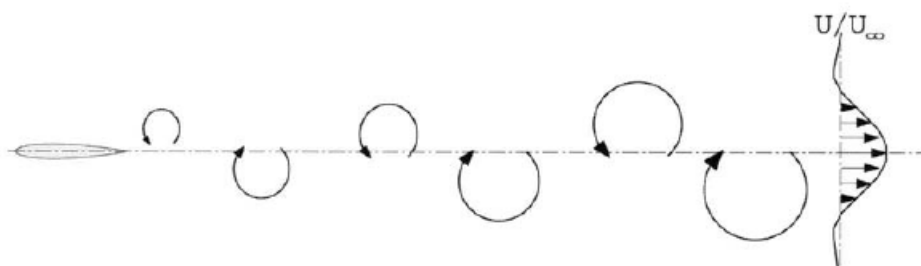


**Figure 1.18 :** Vortex Street indicative of a jet-like flow

The flapping airfoil is acting like a ‘jet-engine’. As the flow is being entrained between the two vortex rows, the time-averaged velocity distribution can be

observed on Figure 1.18. It is plotted in a plane perpendicular to the airfoil, and a jet-like velocity profile is obtained.

In the 1960's, thanks to the increasing computer resources, the next big advance in the analysis of unsteady flows was achieved since large systems of linear equations could be solved in a reasonable amount of time. Therefore the limitations imposed by the small disturbance theory were removed and the effects of airfoil shapes and amplitudes could be taken into account. Nevertheless, the potential flow assumption was still retained.

It was Hess and Smith [18] that were the pioneers of the Panel method capable of modelling inviscid steady incompressible airfoil flows. The airfoil geometry effects are taken into account by distributing a number of sources and vortices all along the airfoil surface. By satisfying the tangency condition for every panel as well as satisfying the Kutta condition that insures that the pressure difference at the trailing edge is zero, a system of equations for the unknown source and vortex strengths is obtained.

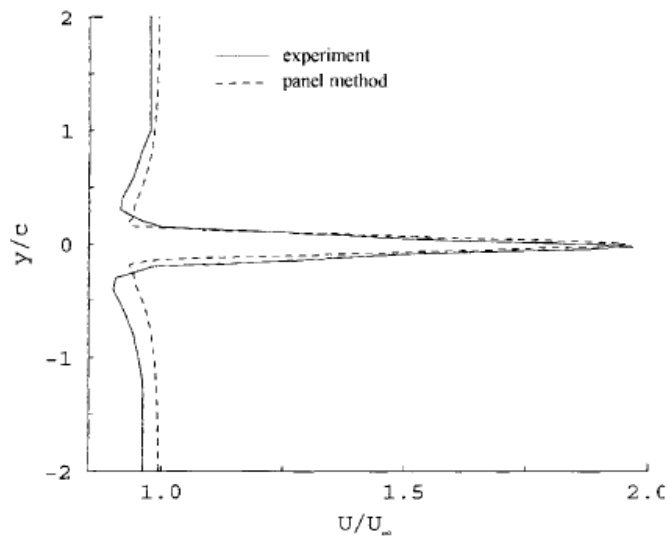


**Figure 1.19 :** Comparison of time-averaged velocity profiles

K.D Jones, CM. Dohring and M.F. Platzer [19] have compared the experimental results to those provided by the inviscid unsteady panel method. As we can see on Figure 1.19, the velocity profiles are in remarkable agreement.

Later in the 1960's, it was realized that the computation of the viscous effects could be greatly improved by using finite difference solutions, for instance the viscous-



inviscid interaction methods enabled to predict separation bubbles and lift and drag characteristics of airfoils subject to an incompressible steady flow.

Finally, in the 1980's, it became possible to drop the inviscid flow assumption and to achieve flow solutions based on the Navier-Stokes equations. The Reynolds-averaged Navier-Stokes equations could be solved, implemented with the most appropriate turbulence model. As a result of the important developments that took place in the last few decades, three methods can be used to analyse low-speed airfoil flows, namely Panel methods, Viscous-inviscid interaction methods and Navier-Stokes methods.

## **1.4 Previous Work on Unsteady Low-Speed Aerodynamics**

Since aerodynamicists provided an explanation for the thrust generation of oscillating airfoil, many numerical analyzes and experimental studies have investigated the effect of the flapping parameters on the propulsive efficiency and thrust generation. Our aim is to now review the progress of CFD analysis in the area of flapping wing aerodynamics, while also considering some experimental works as references. We will first of all present the studies that have been undertaken on pure plunge and pitch motions and finally the research that concerns combined pitching and plunging motions. We will see that both the computational and experimental studies have investigated the effect of flow parameters such as the Reynolds number ( $Re$ ) but also the kinematic parameters such as the reduced frequency ( $k$ ), the amplitudes of the motions and the phase difference between pitching and plunging ( $\varphi$ ), on the thrust generation and propulsive efficiency. The objective was to determine the optimum values of flapping frequency and flapping amplitude that would either generate a maximum thrust coefficient with a reasonable propulsive efficiency or the opposite.

### **1.4.1 Plunging airfoils**

The earliest studies concerning flapping airfoils were restricted to pure plunging airfoils. Indeed, it is very instructive to observe the changes that occur in the vortex shedding of an airfoil that is oscillating in a pure plunge mode.

We recall Garrick's prediction of thrust and efficiency based on the incompressible potential flow assumption and Kutta condition imposed at the trailing edge. His

formulations were functions of the reduced frequency  $k$  and of the maximum non-dimensional flapping velocity  $kh$ . He demonstrated that airfoils undergoing a pure plunging motion would generate thrust which would always be proportional to the square of the maximum non-dimensional flapping velocity  $kh$ . However, for a reduced frequency smaller than four ( $kh < 4$ ), an additional dependence on  $k$  exists.

Tuncer and Platzer [20] have investigated the flow past the NACA 0012 airfoil using a Navier-Stokes solver for a Reynolds number of  $3 \times 10^6$ . The reduced frequency was taken as  $k \in [0.2 - 3]$  and the plunging amplitude as  $h \in [0.1 - 0.4]$ . The maximum propulsive efficiency was found to be obtained for a maximum non-dimensional flapping velocity of 1.2. They also investigated the effect of positioning a stationary airfoil in tandem with the oscillating one, separated by two chord lengths. This had a significant impact on the maximum efficiency and thrust coefficient that were increased by 40 % and 33 % respectively.

Jones et al. [21] in 1997 used a 2D incompressible panel code to solve the flow around several airfoil sections. The values of reduced frequency were taken as  $k \in [0.01 - 10]$  and the plunging amplitudes considered were  $h \in [0.1 - 0.4]$ . They noticed that changing the thickness of the airfoil had very little influence on the behaviour of the propulsive efficiency and thrust generation. Therefore the values of  $k$  and  $h$  that maximize these parameters were found to be the same for all of the airfoil section considered.

Lai and Platzer [22] explored the flow field downstream of the NACA 0012 airfoil that was oscillating sinusoidally in pure plunge.

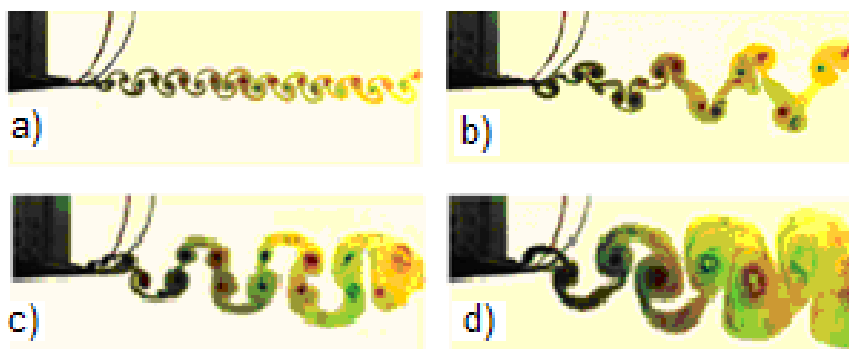


**Figure 1.20 :** Transition from normal to reverse Karman vortex street as  $kh$  increases  
a)  $kh = 0$  b)  $kh = 0.1$  c)  $kh = 0.2$  d)  $kh = 0.4$

They performed dye flow visualization and single-component laser Doppler

velocimetry. As we can see on Figure 1.20, a certain value of  $kh$  needs to be exceeded for the transition from a drag-producing Karman vortex street to an *inverse* Karman vortex street to occur. This limit was found to be approximately equal to  $kh = 0.25$ . They also showed that the separation region that develops in the trailing edge region is crucial and requires a viscous flow analysis. Indeed, an unsteady panel method would eliminate the trailing edge separation region. In addition, at a Reynolds number of 20 000, multiple vortices per half cycle were revealed experimentally and also predicted by the Navier-Stokes solver. At the contrary, the inviscid solution totally eliminates them. As far as the Navier-Stokes calculations are concerned, the turbulence model under-predicted the extent of the separation region, whereas the laminar model led to realistic results.

Windte et al. [23] investigated the flow field experienced by an airfoil undergoing pure plunge motion. The start- and stop-vortices that are shed at the TE and convect in the main flow were observed. These vortices induce velocities on the airfoil which lead to a phase shift between the force and motion, caused by viscous effects. The phase shift grows as the reduced frequency  $k$  increases. Figure 1.21 a) shows that  $C_x$  coefficient always remains positive and therefore no net thrust is ever produced. Just like Kussner [24] proved for the inviscid flow around a flat plate, the efficiency decreases as  $k$  increases. Without any propulsive device, they concluded that flying at  $Re = 6000$  using pure plunge motion is impossible.

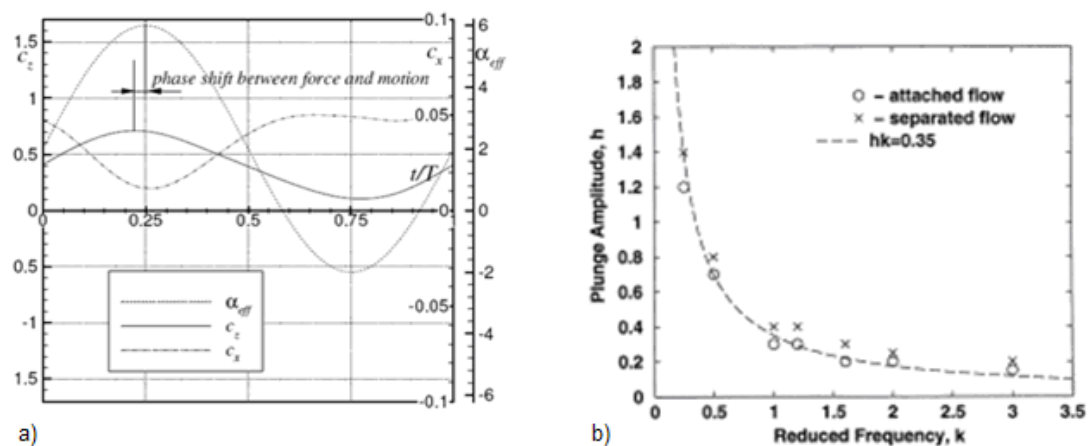


**Figure 1.21 :** a)  $C_x$ ,  $C_z$  and  $\alpha_{eff}$  for one plunge period b) Division of the  $h$ - $k$  plane at  $k = 0.35$

In 1998, the study of Tuncer et al. [25] consisted in a computational investigation of the effect caused by dynamic stall on a flapping airfoil. The flow experienced by the

NACA 0012 airfoil was solved with a 2D compressible Navier-Stokes solver at a Reynolds number of  $10^6$ . Their first result showed that the thrust increases with increasing frequency and amplitude of oscillation. They showed that the maximum non-dimensional flapping velocity  $kh$  should be kept under 0.35 to avoid dynamic stall which causes the efficiency and thrust to drop dramatically. This value was found to hold for a wide range of reduced frequencies and amplitudes as shown on Figure 1.21 b). As we can see, the flows on the left-hand side of this limit remain attached and at the contrary those on the right-hand side are separated which corresponds to a stalled-flow. Under these conditions, the dynamic stall is present and the loss in performance is consistent with expectations. Therefore, as long as  $kh$  is smaller than this critical value, a large reduced frequency and a small plunging amplitude can be selected or the opposite. However, as shown by the experimental results obtained by Lai and Platzer [22] presented previously,  $kh$  has to remain large enough for the case to maintain a thrust-producing *reverse* Karman vortex street.

This study was completed by Platzer et al. [26], that made calculations with a Navier-Stokes solver at a Reynolds number of 20 000. Their observations were based on the behaviour of the thrust and efficiency as a function of the reduced frequency and amplitude of oscillations. The following two graphs compare Garrick’s linear theory to panel code results for both planar (Garrick’s wake) and deforming wake (allowing shed vorticity to evolve in time), as well as Navier-Stokes analyses performed by Lewin and Haj-Hariri [27] and Young [28].

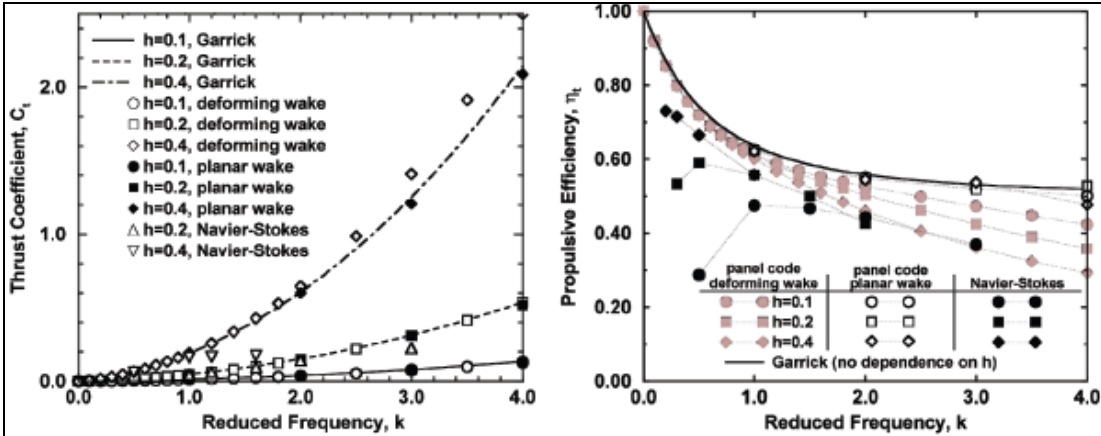


**Figure 1.22** : Thrust coefficient and propulsive efficiency as a function of the reduced frequency

We observe from Figure 1.22 that while the thrust increases with the reduced frequency  $k$ , the propulsive efficiency that is of equal interest is decreasing. On one

hand, as  $k$  increases more starting vortices are being shed and therefore the induced thrust force is more important. On the other hand, it also leads to shortening the wavelength of the wake vortices. Consequently, the vortices remain closer to the airfoil for a longer period. Due to this increased interaction, the efficiency drops. To conclude we may say that although the plunging motion of the airfoil at high frequency generates high thrust values, the power requirement increases much faster than the thrust. Considering the critical value of  $kh$  equal to 0.35, the question is to determine the best combination of frequency and amplitude. Platzer et al. argued that the best configuration is to operate at a high frequency and low amplitude in order to minimize the effect of the leading-edge vortex. Lewin and Hariri numerically examined the flow experienced by an elliptical plunging airfoil at a Reynolds number of 500. In agreement, they found that by varying the reduced frequency  $k$ , the leading edge vortices have an important impact on both the thrust and efficiency of the airfoil. On Figure 1.23, we may observe how the LEV created during the upstroke and positioned underneath the airfoil is going to evolve during downstroke. As we can see, it advects downstream and interacts with the TEV that rotates in the opposite direction.

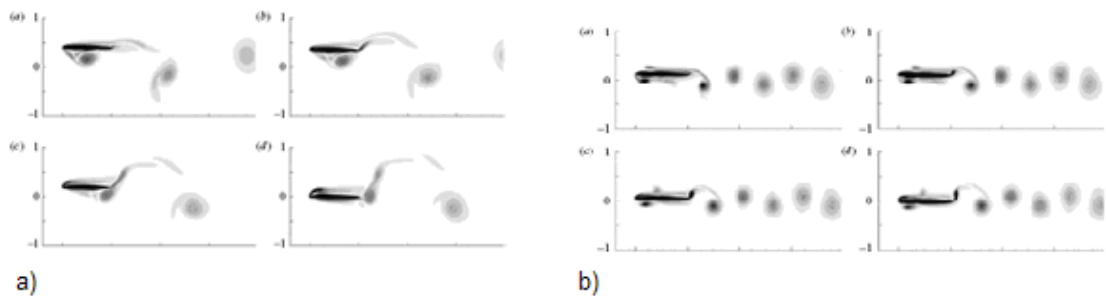


**Figure 1.23** : a) Vorticity field for  $k = 2$  (downstroke) b) Vorticity  $k = 6.667$  (downstroke)

Eventually, the LEV, its secondary vortex and the TEV form a single vortex. For a higher frequency, the LEV reaches the trailing edge just as the TEV is being created, such that the vortex deposited into the wake is much weaker. Whenever the LEV detaches and interacts with the TEV, the forces acting on the airfoil drop substantially. As the frequency increases further, the LEV remains near the leading edge during a substantial part of the stroke as seen on Figure 1.23 b). Its strength diminishes by dissipation due to its interaction with the airfoil. The LEV being dissipated instead of shed produces large increases in efficiency. These results are in

agreement with Gustafson and Leben that stated that the vorticity contained in the LEV is partly recaptured by the airfoil. It also appeared that the transition regions were characterized by asymmetric and aperiodic flows. In addition, they observed that for high values of  $k$  and  $kh$ , the simulations produced aperiodic results. The first one to observe these deflected vortex wakes was Bratt [29]. Jones et al. [19] commented on the nonsymmetric vortex shedding and compared the experimental results to those provided by the panel code.

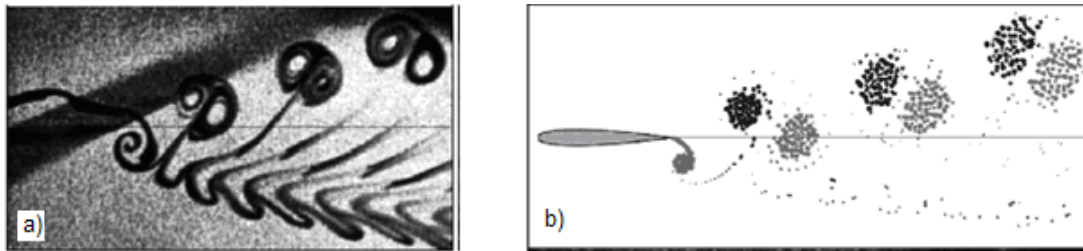


**Figure 1.24 :** a) Flow visualization b) Panel code prediction,  $kh = 1.5$

As we can see by comparing Figure 1.24 a) to b), the panel mode was able to predict this phenomenon which suggested that this kind of vortex shedding was due to inviscid effects.

Young and Lai also investigated the effect of leading edge flow separation and showed that not only  $kh$  had to be considered as a controlling parameter but also  $k$  needs to be taken into account independently. In 2007, Ashraf et al. [30] solved the flow field around a NACA 0012 airfoil by using an unsteady compressible Navier-Stokes solver (CFD package *Fluent*). A much wider range of frequencies and amplitudes were considered, such that  $k = 0.5$  to 24 and  $h = 0.0125$  to 48. Their results confirm the observations of Young and Lai as we can observe on Figure 1.25.

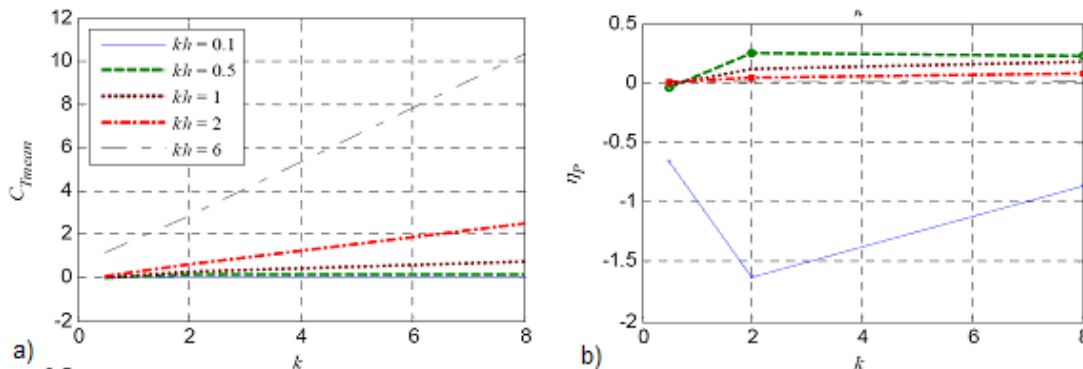


**Figure 1.25 :** a) Variation of  $C_{Tmean}$  with  $kh$  for  $h = 0.175$  b) Variation of  $\eta_p$  with  $kh$  for  $h = 0.175$

Indeed the values taken by  $\eta_p$  &  $C_{Tmean}$  depend on both the reduced frequency and maximum non-dimensional plunging velocity. It was also confirmed that operating at high frequency and low plunging amplitude is more advantageous rather than the opposite. This avoids leading edge separation that results in a very low propulsive efficiency.

#### 1.4.2 Pitching airfoils

According to Garrick's [15] prediction of thrust generation based on Theodorsen's method, for a purely pitching airfoil thrust is only generated above a certain reduced frequency  $k$  that depends on the pivot point location. For instance if the pitching axis is located at  $1/4 \cdot c$ , then the critical value corresponds to:  $k = 3.25$ . Figure 1.26 a) illustrates the theoretical results he obtained:

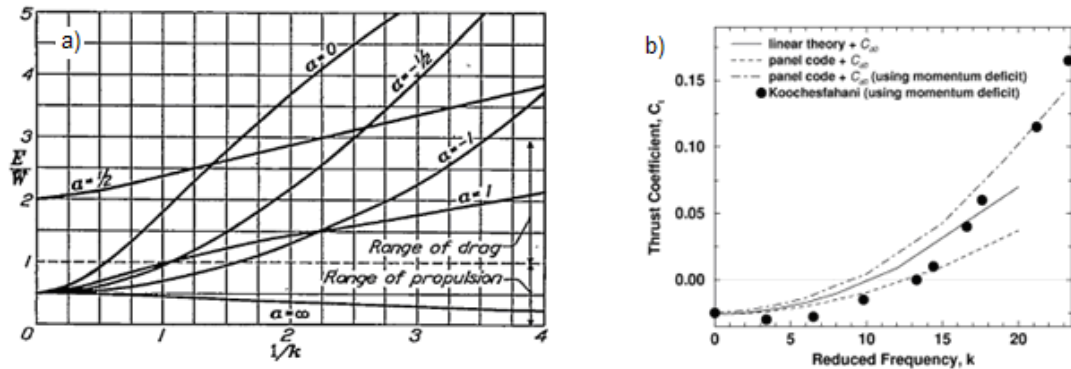


**Figure 1.26 :** a) Ratio of  $E/K$  as a function of  $1/k$  [15] b) Experimental verification of Garrick's predictions [31]

The ratio  $E/K$  represents the energy per unit time released in the wake to the work per unit time that is required to maintain the oscillations. For thrust to be generated, which corresponds to  $E/W \in [0;1]$ , the reduced frequency  $k$  has to be very large (small  $1/k$ ). For any values outside of this range, drag is produced. These results were then experimentally verified by Koochesfahani [31] as we may observe on Figure 1.26 b). Due to the lower level of thrust generated, not many studies have investigated the behaviour of pure pitching airfoils. There has not been much work done on the effect of the important parameters that govern this motion alone. Amongst them, the mean pitching angle, the Reynolds number and pitch axis location may be critical. Sarkar and Venkatraman [32] have investigated the influence of various flow and airfoil motion parameters on the behaviour of the wake

and thrust generated. They have investigated the effect of the reduced frequency  $k$ , the pitching amplitude  $\alpha_1$ , the mean angle of attack  $\alpha_m$  and the location of the pitching axis, on the mean thrust coefficient  $C_{T\_mean}$ . To solve the flow, the incompressible Navier-Stokes equations were used and the unsteadiness was simulated thanks to a discrete vortex technique. The Reynolds number was fixed to  $10^4$ , two pitch amplitudes were selected such that  $\alpha_1 = 2.5^\circ$  and  $5^\circ$  and the mean angles of attack that were considered were:  $\alpha_m = 0^\circ, 5^\circ, 10^\circ, 15^\circ$ . The frequency of oscillation  $\omega$  varied between 5 and 10 since smaller values do not produce any thrust.

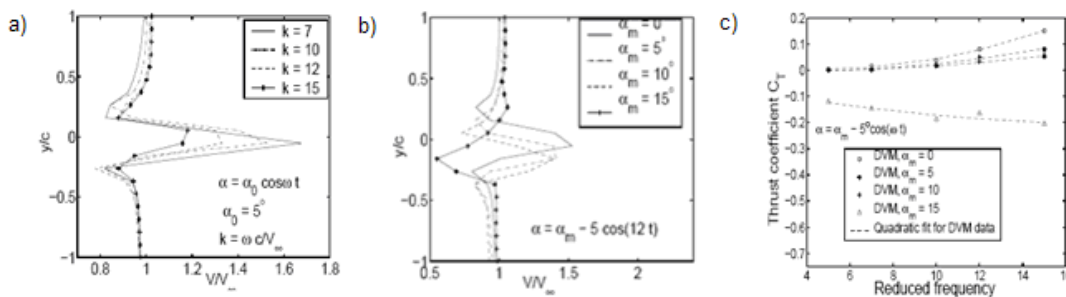


**Figure 1.27 :** Results collected by [32] a) Frequency variation b)  $\alpha_0$  variation c)  $C_T$  Vs.  $k$

The results are presented on Figure 1.27 from a) to c). The first two illustrate the mean velocity profiles which are indicative of the momentum excess or deficit on the airfoil thus indicating net drag or thrust. These plots show firstly that the thrust increases as the reduced frequency becomes higher and secondly that the opposite effect is obtained when the mean angle of attack increases since the thrust decreases, eventually for  $\alpha_m = 15^\circ$  drag was obtained. These results are confirmed on Figure 1.27 c). The conditions to obtain a jet-like pitching airfoil have shown to be relatively constraining.

While presenting the purely plunging airfoils, we mentioned that Katzmayr [10] had experimentally verified the Knoller and Betz effect. In reality he performed two different experiments. The first one simulating pure plunging consisted in holding an airfoil stationary in an oscillatory flow, and the results were satisfactory. In the second one, the airfoil was pitching in a uniform flow and at the contrary it proved to be unsuccessful since no thrust was measured. When it comes to an airfoil undergoing pure pitch oscillations it is essential to take into account the flutter



phenomena that are potentially disastrous. Let us consider an airfoil mounted on torsion spring in a two-dimensional flow, subject to this motion about its leading edge as shown on Figure 1.28 a).

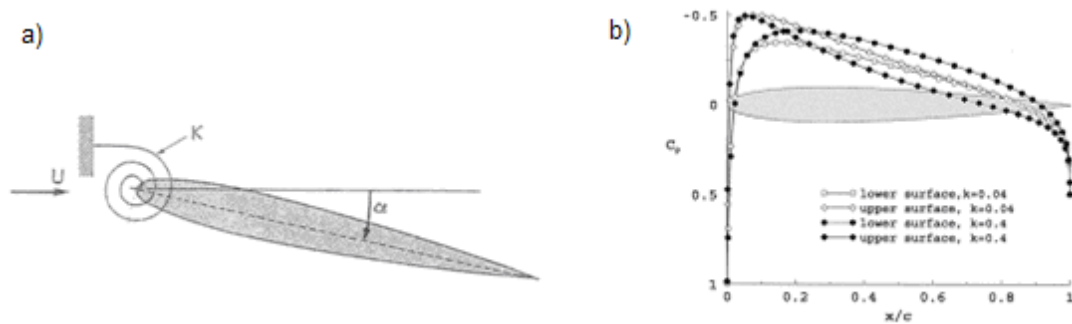


**Figure 1.28 :** a) Rigid airfoil in pure pitch b) Pressure distributions (pitching motion)

As the airfoil is put into motion, starting vortices are being shed from the trailing edge and affect the pressure distribution plotted on Figure 1.28 b). The NACA 0012 airfoil is a symmetric airfoil and therefore at zero angle of attack the upper and lower pressure distributions would coincide. However, when the airfoil is excited into a pitching oscillation, this motion and the starting vortices induce a lag effect on the pressure distributions such that the upper and lower distributions differ.

In the case of a low reduced frequency ( $k = 0.04$ ), the pressure exerted on the upper surface is less than on the lower surface. This is a direct consequence of the lag effect, and at low frequencies only vortices of same sign are inducing these pressures. Consequently, the motion is reinforced at each pitching cycle due to the induced moment that is in the direction of the motion. This case is referred to as a dynamically unstable ‘flutter’ motion. At the contrary, for higher frequencies, both the clockwise and counter clockwise vortices affect the pressure distributions, such that a positive damping moment is created.

To conclude we may say that it is critical to accurately predict the vortex shedding taking place. The flutter phenomenon may induce disastrous consequences and has to be avoided.

### 1.4.3 Combined pitching and plunging airfoil

Birds, flying animals or insects do not solely use a pure plunging or pitching motion to fly but at the minimum combine pitching and plunging. In the case of many insects for instance, the movement is actually more complex since the wings flip

during the cycle. However we are limiting the scope of this study to simple forward flight. Indeed, all examples of flapping wing propulsion in nature combine both motions, although as we have just seen throughout the presentation of plunging airfoils, both are not required for producing thrust; however it enhances the propulsive performance. As a result of this combination we will see that the number of parameters controlling the movement increases. For instance, the phase angle between pitch and plunge motions is critical and so are their amplitudes. To better understand the interest that the flapping mode for oscillating airfoils represents, let us observe what physically occurs as far as the effective angle of attack is concerned. Indeed, it is a key parameter and indicates whether the airfoil is creating thrust or extracting power from the flow.

The first systematic approach for analysing flapping-wing propulsion of airfoils combining pitching and plunging was achieved thanks to Garrick's [15] linear approach. Indeed, the following equation was able to predict the thrust coefficient  $C_t$  while taking the two degrees of freedom into account:

$$C_t = \pi k_G^2 (C_{t\alpha} + C_{th} + C_{tc}) \quad (1.13)$$

The coefficients  $C_{t\alpha}$ ,  $C_{th}$  and  $C_{tc}$  represent the contributions of pitch, plunge and combined effects respectively, on the thrust. We will now present as we did for the pure plunging motion, the recent experimental and numerical studies of the flow over a 2D combined pitching and plunging motion.

In 2001, Jones et al. [33] compared the thrust, power and efficiency computed by Garrick's linear theory to theirs obtained with the panel code. These parameters are plotted on Figure 1.29 a) as a function of the phase angle  $\varphi$  between the pitching and plunging motions. We note that the two horizontal lines represent the thrust coefficient and efficiency for an airfoil undergoing a pure plunging motion. As expected these performance parameters are highly dependent on the phase angle. For values approximately between 60 and 165 degrees, the efficiency  $\eta_t$  exceeds the corresponding value  $\eta_{tp}$  of a pure plunge motion.

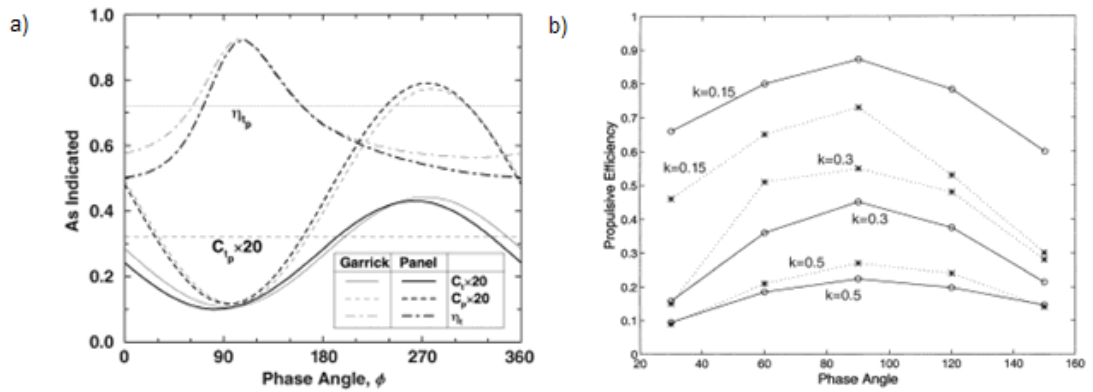


**Figure 1.29 :** a) Numerical predictions as a function of  $\phi$  [33] b)  $\eta_p$  as a function of  $k$  and  $\phi$  [34]

It is within this range that the advantages of a combined motion appear, resulting in enhanced performance of the airfoil. The highest value of  $\eta_i$  is achieved when pitch leads plunge by about 90 degrees. Indeed, Tuncer et al. [34] came to the same conclusion. They investigated the flow over the NACA 0012 airfoil at a Reynolds number of  $10^5$  for which the pitching amplitude was  $\alpha_1 = 10^\circ$  and the plunging amplitude was  $h = 1$ . The aim of this study was to determine the optimum phase angle, for which the reduced frequency would vary in the range  $k \in [0.3; 1]$ . The results showed that the peak in propulsive efficiency is independent of the frequency and always appears at  $\phi$  equal to 90 degrees. In any case, it is the pitching motion that has to lead the plunging motion. These results could be compared to those collected by Isogai et al. [35] that carried out their own computations under the same conditions. The propulsive efficiency is plotted as a function of the phase angle  $\phi$  and the reduced frequency  $k$  for both sets of results on Figure 1.29 b). Again this result is confirmed since the optimum efficiency always occurs when the pitching leads the plunging by about 90 degrees.

Young and Lai [28] also studied the combined motion of an oscillating airfoil. Their computational conditions were chosen identical to those of Anderson et al. [36] in order to compare the results to experimental data. The objective was to investigate the effects of Strouhal number on the thrust generation and propulsive efficiency of the NACA 0012 airfoil. Figure 1.30 shows the case where the plunge amplitude is equal to 0.75, the pitch amplitude is 15 degrees, the phase angle is 90 degrees and the Reynolds number is 40 000.

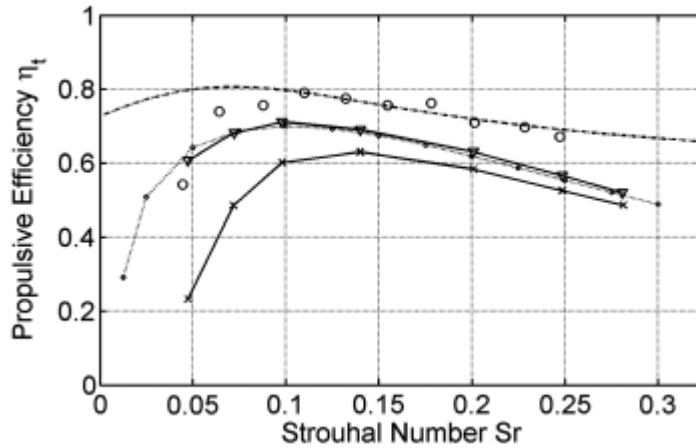


**Figure 1.30 :** Propulsive efficiency as a function of Strouhal number [28]

The Navier-Stokes and experimental results both indicate a peak in propulsive efficiency for Strouhal numbers within the interval  $[0.1; 0.2]$ . However, they also showed that the Strouhal number alone is insufficient to characterize the efficiency of flapping airfoils. Firstly, an optimal Strouhal number does not select an optimum frequency since both the frequency and plunging amplitude can vary to fix the Strouhal number.

Most importantly, the leading-edge vortex shedding has a significant impact on the propulsive efficiency. To better understand the role of the unsteady aerodynamics on the selection of a preferred range of frequencies, Z. Jane Wang [37] focused on the frequency selection process in forward flapping flight. The optimal flapping was defined as being the one that produces the maximum thrust coefficient. The Reynolds number dependence was expected to be relatively weak, therefore the parameter was fixed to 1 000. Two Strouhal numbers were defined:

$$St_a = fA/u_0 \quad \text{and} \quad St_c = fc/u_0 \quad (1.14)$$

$St_a$  measures the ratio of the maximum flapping and forward velocities and  $St_c$  is the usual dimensionless flapping frequency. We will see that both parameters are necessary to select an optimal flapping frequency.  $St_a$  was shown experimentally to be a scaling variable, at first it was held constant while  $St_c$  varied. First of all, some general observations were made. The thrust and lift coefficients were computed for different Strouhal numbers. It was shown that for  $St_c$  equal to 4, the trailing-edge

vortex is too weak and a drag-producing wake is obtained. As  $St_c$  decreases, the trailing-edge vortex grows and we switch to a thrust-producing wake. Finally, as  $St_c$  further decreases the leading-edge vortices start shedding which reduces the thrust force since they have the opposite sign to the trailing edge-vortex. Figure 1.31 illustrates the vorticity contours for the thrust-producing Strouhal numbers.

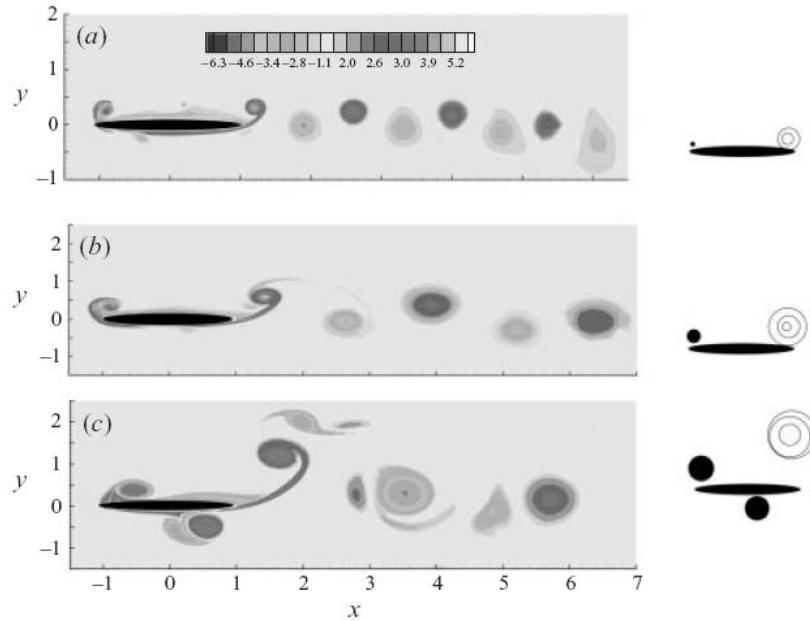


**Figure 1.31 :** Contour plot of the wake vorticity for different  $k$  values [37] a)  $St=2.0$ , b)  $St=1.0$ , c)  $St=0.5$ .

The intermediate value of  $St_c$  equal to 1 led to the optimal thrust and efficiency. To better understand these vortex dynamics, the vortices' growth and the forces were observed. Firstly, the time-dependent lift coefficient was computed to illustrate the unsteady behaviour of the airfoil.

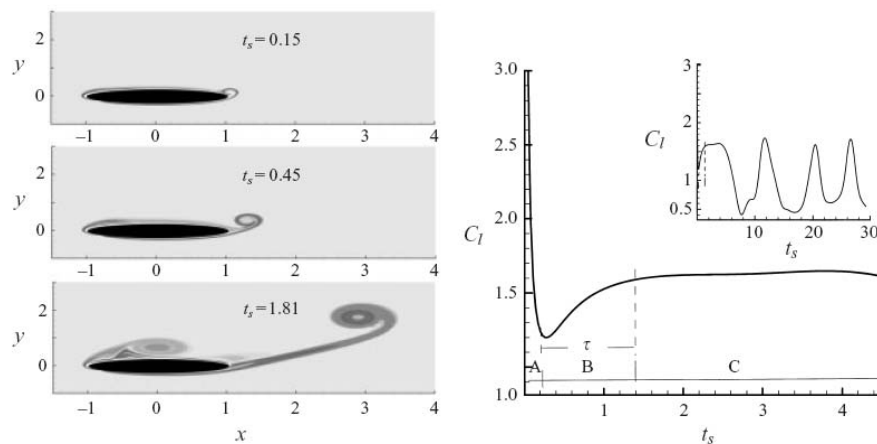


**Figure 1.32 :** Vorticity contour plot and  $C_L$  for  $\alpha = 40^\circ$  and  $Re = 1000$  [37]

On Figure 1.32 we observe its evolution as well as the vorticity contour plot. The behaviour of  $C_l$  indicates three different regions. Region A corresponds to the diffusion of the boundary layer vorticity just after the impulsive start, region B represents the growth of the trailing edge vortex and formation of the attached leading edge vortex. In region C, the lift reaches a quasi-steady state while the vortices are convected downstream. At a much later time, the leading and trailing vortices interact which leads to the von Karman wake corresponding to the ups and downs of the lift force, illustrated top-right. The characteristic time  $\tau$  is of major importance, and it clearly appears that the airfoil needs to flap slowly enough for the vortex to have sufficient time to grow. The importance of the leading-edge vortex was investigated by varying the angle of attack. It was shown that when the leading-edge vortex remains attached it induces a lower pressure region which increases the lift. For instance, when  $\alpha$  is taken as 4.5 and 72 degrees, both leading and trailing-edge vortices are shed leading to less lift, unlike the case where  $\alpha$  is equal to 42.5 degrees and the leading-edge vortex is bound. Figure 1.33 illustrates the thrust window for different angles of attack.

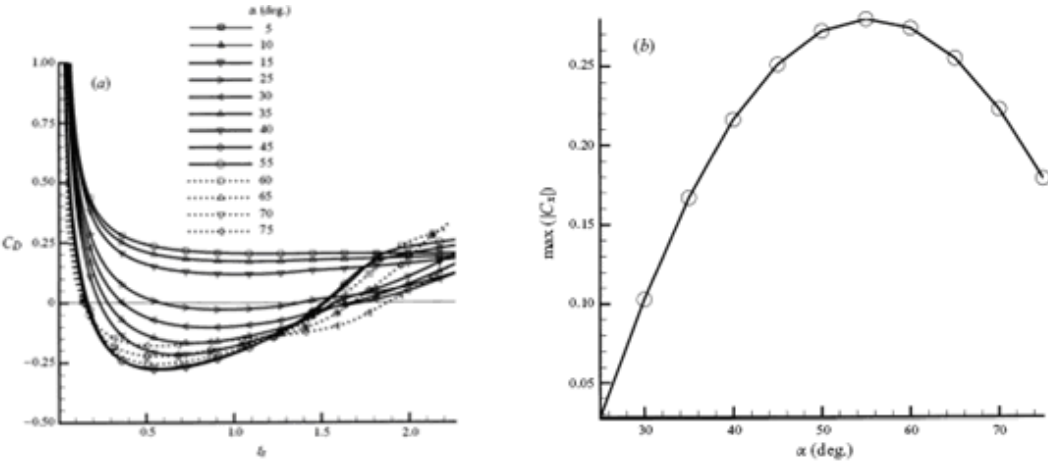


**Figure 1.33 :** a) Evolution of  $C_D$  in time ( $\Delta\alpha$ ) [37] b) Evolution of  $C_x$  as a function of  $\alpha$  [37]

On Figure 1.33 a), it appears that thrust is only produced above a certain angle of attack, equal to 20 degrees in this case (negative values of  $C_D$  are required). The thrust force generated is time-dependent and can be maximized across the stroke. Indeed, it only occurs within a certain time window, equal to  $t_s \in [0.2; 1.5]$ . Physically, the lower bound corresponds to the necessary time required for the sufficient growth of the trailing-edge vortex. As for the upper bound, it is the time

scale from which the leading-edge vortex is no longer attached and starts to shed. Figure 1.33 b) shows the maximum angle at which the thrust starts to drop as a consequence of this shedding process. By collecting all this information, we deduce that the maximum angle of attack should be contained in the interval  $45^\circ$ - $60^\circ$  to obtain a high thrust as seen on part a) of the figure. This range is equivalent to selecting a Strouhal number contained in  $[0.16; 0.27]$  which is in agreement with other studies. Secondly, the time taken by the stroke should be well contained in the thrust window. This second requirement imposes restrictions on the selected frequency. Coming back to the previous observations, we recall for instance that  $f$  equal to 2 Hz ( $St_c = 4$ ) would produce drag instead of thrust. This can now be explained since this frequency would mean that  $t_s$  is smaller than the lower bound characterizing the thrust window. Finally, the propulsive efficiency is dependent on both  $St_a$  and  $St_c$  as shown on the following Figure 1.34:

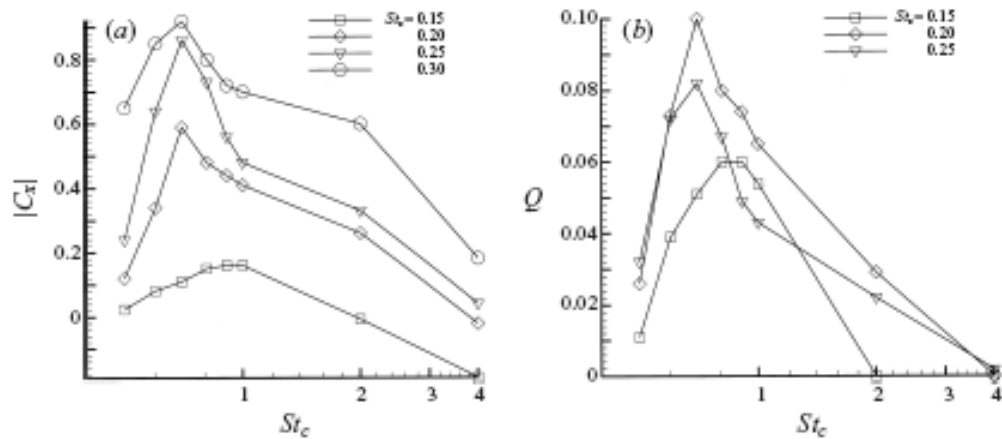


**Figure 1.34 :** Thrust and efficiency as functions of  $St_c$  for various  $St_a$  values [37]

Its behaviour is similar to the thrust since peaks are observed within a certain  $St_c$  interval. The dependency of these optimum  $St_c$  values with  $St_a$  is relatively weak. We may conclude by saying that the optimum flapping frequency  $St_c$  for a fixed  $St_a$  will be chosen according to the two time scales that govern the growth of the trailing-edge vortex and the shedding of the leading-edge vortex.

All these series of results were later confirmed by other studies. Guglielmini and Blondeaux [38] extended these investigation and studied the Low Reynolds number effects over a flapping NACA 0012 airfoil, by means of numerical solution of the vorticity equation. The calculations were undertaken for a Reynolds number of 1100.

The highest efficiencies were of about 0.45 for high pitching amplitudes between 30° and 40° and for  $kh$  within the range  $[0.94; 1.25]$  which corresponds to Strouhal numbers around  $[0.3; 0.4]$  as we can see on Figure 1.35.

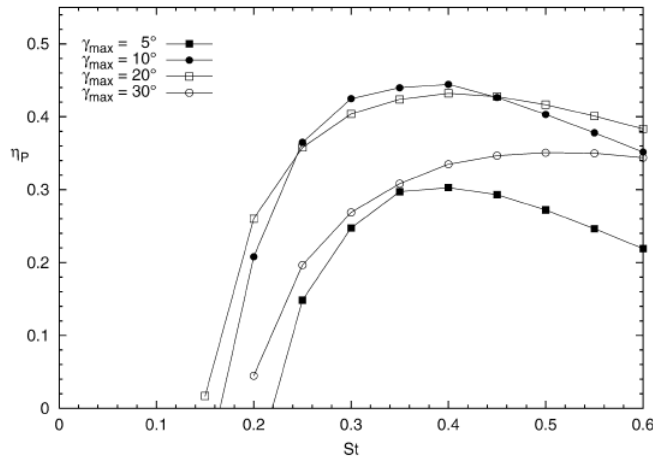


**Figure 1.35 :** Propulsive efficiency as a function of St for several angles [38]

As had been proved by Anderson et al. [36] the curves are characterized by a slow decrease once the maximum Strouhal number  $S_{t_{max}}$  is exceeded whereas the  $\eta_p$  drops quickly for smaller values. The flow visualizations confirmed that high efficiencies and significant thrust values are accompanied by the generation of moderately strong leading edge vortices, which then amalgamate with the trailing edge vortices. Consequently, the vortex structures result in a reverse Karman street. Again it was shown that the phase angle is critical since it determines the timing of the formation and shedding of the leading edge with the trailing edge vortices of same sign, shed at the trailing edge. They found that the maximum propulsive efficiency is obtained at a phase angle of 80 degrees. An investigation of the effect of different flapping parameters was undertaken. The pitching axis was varied from -0.5 to 2 chord lengths and the location maximizing the efficiency was found to be 1/3 chord lengths from the leading edge. Finally, the Reynolds number was increased up to 3300 and a 20% increase in efficiency was obtained compared to the previous  $Re$  of 1100.

For the same Reynolds number of 1100, Ramamurti and Sandberg [39] computed the flow around the NACA 0012 airfoil using an incompressible Navier-Stokes solver. The pitching axis was fixed to  $\frac{1}{4}$  of the chord length. Their results indicated that  $kh$  was more of a critical parameter than  $k$ . The phase angle was varied from 30 to 140



degrees and the optimum values to maximize the propulsive efficiency and thrust were found to be 90 and 120 degrees respectfully.

Young and Lai [40] investigated the flow past the NACA 0012 airfoil in flapping motion for Reynolds numbers in between 20 000 and 40 000. Navier-Stokes computations were presented and the main focus was brought on the mechanisms that influence the efficiency of these oscillating airfoils. Indeed, it has been shown up to now that optimum propulsive efficiencies exist within the range  $0.2 < St < 0.4$ . Therefore, in this study the effects of flow separation were investigated, by restricting the case to large-amplitude pitching and plunging motions. The evolution of the propulsive efficiency as a function of the Strouhal number was once again found to be identical to previous studies and we may refer to Figure 1.35 for instance. Young and Lai stated that for lower  $St$  values, the drop in efficiency is partly caused by the increasingly large viscous drag. As for the peak in propulsive efficiency, its magnitude and Strouhal number at which it occurs are influenced by many mechanisms. As we know already, the leading-edge separation will reduce the efficiency at higher Strouhal numbers, but it may have the same effect at lower Strouhal number, depending on the motion. As for the flow separation, it depends on the reduced frequency that limits the time available for vortex formation and convection of the vortex. For the peak itself, its magnitude, width and location depend on the type of motion considered. It may emerge at any location within the range [0.1; 0.4]. We may conclude by saying that the Strouhal number alone has proved to be insufficient when it comes to characterizing the aerodynamics of flapping airfoils, especially when leading or trailing edge separations are present.

Read et al. [41] performed experiments on the NACA 0012 airfoil to determine the propulsive efficiency that produces high thrust values. The variation of the principal parameters was undertaken such as the plunge amplitude, Strouhal number, angle of attack and phase angle. At first the plunge amplitude was fixed to 0.75 and the phase angle to 90 degrees. A study of the effect of the pitch amplitude and  $kh$  parameter was made and it was shown that the highest efficiency, equal to 0.715, is obtained for  $\alpha_1 = 15^\circ$  and  $kh = 0.502$ . However the resulting thrust coefficient was found to be very small  $C_T = 0.18$ . Therefore, they then tried to obtain high thrust with

reasonable efficiency values. Very high values up to  $C_T = 2.43$  were obtained with an efficiency of 0.49 for the following conditions:  $kh = 1.88$ ,  $\alpha_1 = 35^\circ$  and  $\varphi = 100^\circ$ .

A better compromise between propulsive efficiency and thrust values was obtained for  $kh = 1.25$ ,  $\alpha_1 = 20^\circ$  and  $\varphi = 90^\circ$ . Finally one of the objectives of this study was to assess the capabilities of the airfoil to produce lateral forces for manoeuvring purposes. Side force coefficients of 5.5 were measured, which would allow the airfoil to have very satisfactory manoeuvring capabilities.

To systematically search for the optimum conditions, Tuncer and Kaya [42] coupled the Navier-Stokes solver to a numerical optimization algorithm. The optimization procedure was based on the steepest decent method. The objective function was defined as the thrust and/or propulsive efficiency of a pitching and flapping airfoil, such that the resulting solutions are maximized values of this function. The optimization parameters were chosen to be the amplitudes of the pitching and plunging sinusoidal motions, as well as the phase angle between them. Parallel processors were used to solve the problem. Figure 1.36 part a) tabulates the optimization cases and starting conditions and part b) the results.

Case	$\beta$	$h_0$	$\alpha_0$	$\phi$
1	0.0	0.5	5	30
2	0.5	0.5	5	30
3	1.0	0.5	5	30
4	0.0	0.5	25	60
5	0.0	1.0	5	60
6	0.0	1.0	25	90
7	1.0	0.5	25	60
8	1.0	1.0	5	60
9	1.0	1.0	25	90

Case	$h_0$	$\alpha_0$	$\phi$	$C_T$	$\eta$ [%]
1	1.60	23.5	103.4	1.41	28.3
2	1.36	29.6	97.8	1.08	44.1
3	0.45	15.4	82.4	0.08	58.5
4	1.73	23.8	100.7	1.44	25.4
5	1.52	26.9	87.2	1.27	33.4
6	1.55	28.6	94.9	1.45	35.9
7	0.57	21.0	86.7	0.13	63.8
8	0.60	22.8	86.1	0.13	64.8
9	0.83	35.6	86.5	0.18	67.5

**Figure 1.36 :** a) Optimization cases and starting conditions [42] b) Optimization results [42]

We note that  $\beta$  controls the performance criteria considered by the objective function. For  $\beta = 1$  it is set to a maximized propulsive efficiency,  $\beta = 0$  to a maximized thrust coefficient and for  $\beta = 0.5$  both are to be maximized at the same time which means a compromise is to be made. By observing the instantaneous particle traces, the results could be related to the physics of the flow. The thrust could be maximized for large plunging amplitudes that lead to the formation and shedding of large leading edge vortices. At the contrary, the propulsive efficiency is increased by reducing the

plunging amplitude and the effective angle of attack. This avoids the formation of leading edge vortices which correlates the previously established observations.

The results that were obtained throughout this literature survey of plunging, pitching and flapping airfoils are all summarized in the tables that can be found in Appendix A.

#### 1.4.4 Three-dimensional flow effects

The extension to three-dimensions is accompanied by several additional flow features that are neglected in two-dimensional flows. The simplification is easily made numerically by only considering an airfoil section in the  $(x-y)$  plane. This is also possible experimentally by placing endplates at the extremities of the wing which will eliminate any wing tip effects as if the wing was of infinite span. We should however mention that totally suppressing the corner flow effects created by the endplates is impossible but three-dimensional approximations can be achieved by averaging several spanwise measurements.

The main effect of a three-dimensional finite wing is the formation of vortices at the tips of the wing. These are unavoidable because of the difference in pressure that exists between the upper and lower surface. Due to the fact that pressure is a continuous function these must equalize at the wing tips.

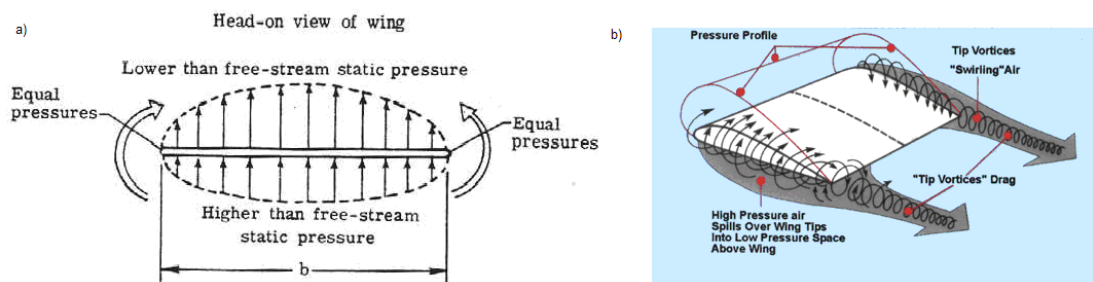


**Figure 1.37 :** a) Equalizing of pressure at the wing tips b) Tip vortices in three-dimensions

This is made possible by the movements of air particles around the tips, from the region of high pressure to the region of low pressure corresponding to the lower and upper surfaces of the wing respectively in the case of positive lift. The air movement is shown on Figure 1.37 a). Combined to the incoming free-stream flow, an inclined inward flow movement is created on the upper surface and an inclined outward one on the lower surface. The spanwise effects dominate at the tips and slowly damp out

as we get closer to the mid-span plane where tip vortices have little effect and the flow characteristics are close to two-dimensional. The inclination of the flow results in the formation of helical air movements illustrated on Figure 1.37 b) and known as vortices that form around the quarter-chord of the wing and gain strength along the chord. In three-dimension, these combine into two cylindrical vortices referred to as ‘tip vortices’, rolling towards each other in the wake of the wing and eventually dissipating further away. The spanwise lift distribution is of course affected by the pressure differences in the third dimension and a loss in lift may be observed at the wing tips. The tip vortices introduce downwash in the wake within the wingspan, due to the inward movement of the vortices. At the contrary, upwash is observed outside of the vortex system as the air moves upwards. These effects are represented on Figure 1.38.

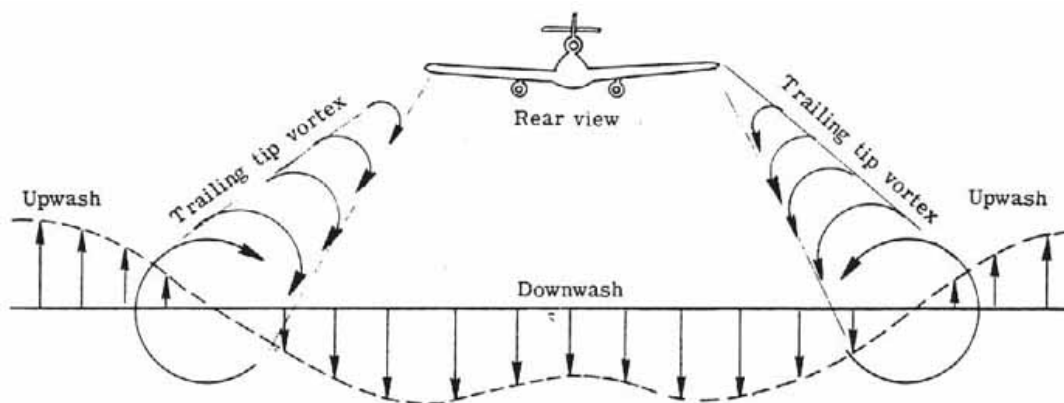


**Figure 1.38 :** Tip vortex system in the wake of an aircraft

This last remark does not apply to MAVs but for conventional scale aircrafts, the disturbances caused by the tip vortex system in the wake of the plane needs to be taken very seriously. Indeed, if another plane flies through it, it can experience strong downwash forces and have a large tendency to roll over. Between takeoff and landings, appropriate distances are to be respected as tip vortices can extend up to eight kilometres and still have a strong effect.

There has been significant work done in order to expand the results valid for two-dimensional unsteady aerodynamics into the third dimension. At first, they were limited to High-Reynolds number flows. Back then, the existing methods fell into three different categories: first of all, blade-element-type computations, for which the model is represented by a number of two-dimensional entities, secondly lifting-line computations for which the model is represented by filaments of vorticity bound

along the span and finally panel codes, where the model is represented by panels along which singularities are distributed.

More recently, the Euler and Navier-Stokes approaches became available and are now able to solve the three-dimensional flow features that are generated by finite-span flapping wings. The full study of the problem in all three dimensions can provide us with a more realistic understanding of the flow physics that occur in the thrust generation of flapping wings. Indeed, the finite-span effects cannot be omitted. We will now present the results that have been obtained in previous works in order to highlight the structure of the flow.

Neef and Hummel [43] investigated the three-dimensional flow past a NACA 0012 airfoil with an aspect ratio of 8, using Euler solutions. They chose to flap the wing about its root section with a pitching axis positioned at the leading edge. The only difference with the two-dimensional case as far as the pitching and plunging motions are concerned is that their amplitudes are now dependent on not only time but also the lateral coordinate  $y$ . The leading edge in the  $y$  direction is represented by a straight line, the angle with respect to the  $(x-y)$  plane is defined as the flapping angle:

$$\psi(t) = \psi_1 \cos(2\pi ft) \quad (1.15)$$

The twisting angle is increasing along the span and therefore depends on both time and  $y$ . As for the pitching and plunging motions, an angle difference may be defined between the flapping and twisting angles which can vary along the span. In this case the angle  $\Phi$  was fixed to 90 degrees such that the flapping angle is given by:

$$\alpha(y^*, t) = \alpha_1(y^*) \cos(2\pi ft + \Phi), \text{ where: } \alpha_1(y^*) = \alpha_{1,tip} \frac{y^*}{b} \text{ and } \Phi = 90^\circ \quad (1.16)$$

The aim was to reproduce the flight conditions of large birds, therefore the parameters were fixed accordingly:  $\psi_1 = 15^\circ$  and  $k = 0.1$ . Also we should mention that these conditions insure that the flow remains attached throughout the flapping cycle. The mean angle of attack  $\alpha_0$  and twist amplitude  $\alpha_{1,tip}$  varied linearly in the  $y$  direction. Figure 1.39 a) represents the wing geometry while b) gives us a few pressure distributions along the span.

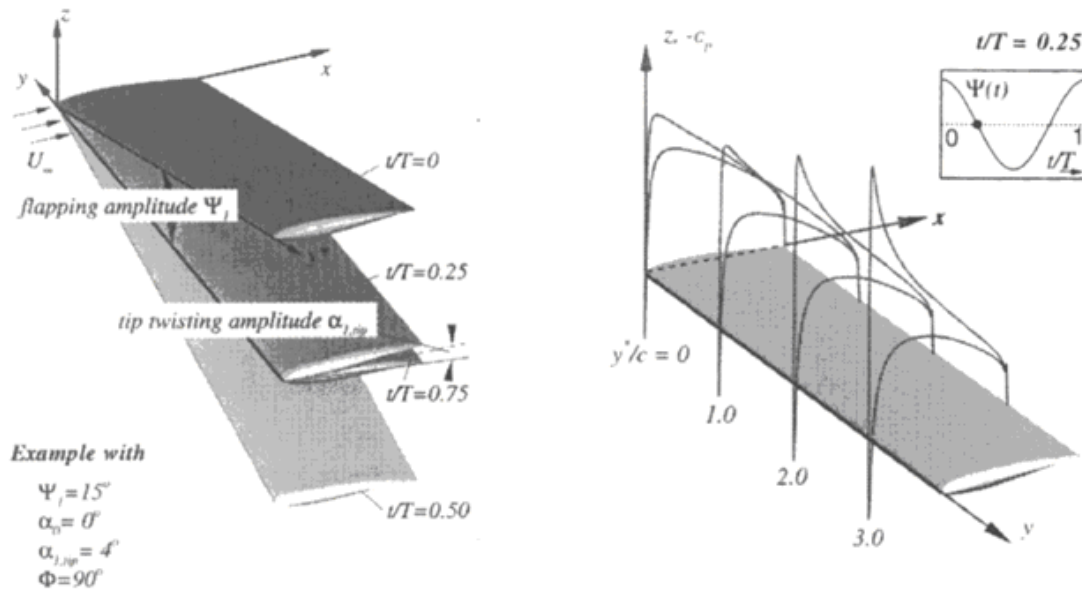


**Figure 1.39 :** a) Wing geometry and parameters [43] b) Pressure distributions along the span [43]

Considering that the effective angle of attack increases along the span, higher differences in  $C_p$  values are found as we get closer to the wing tip. In general the values of propulsive efficiency are lower in the three-dimensional case. Indeed, the two-dimensional method of calculation overestimates efficiency, because it takes into account only the energy of cross-stream wake vorticity (parallel to the direction of motion). In reality, due to the effective angle of attacks, instantaneous tip vortices are formed behind the wingtip. These vortices lead to a loss in energy which decreases the efficiency.

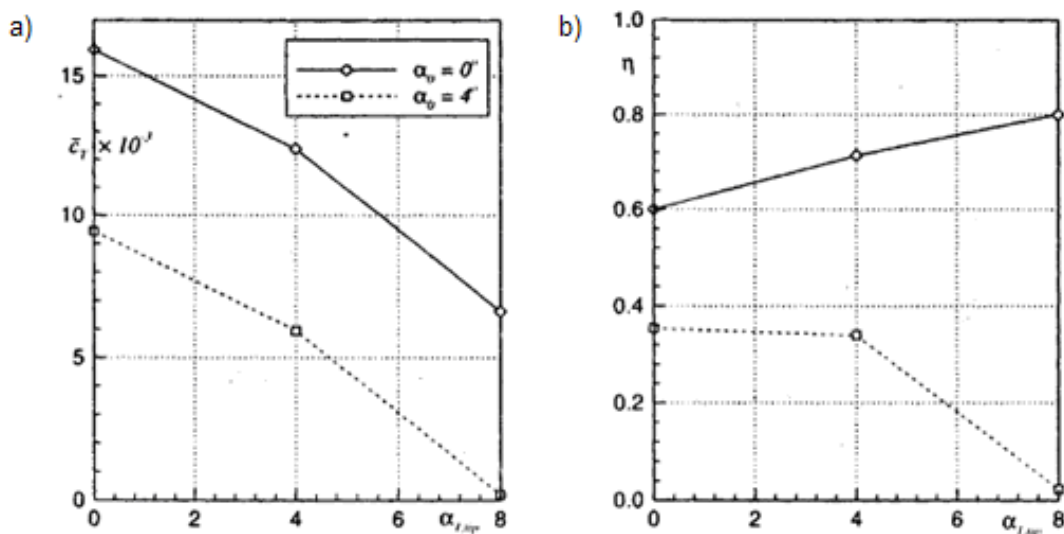


**Figure 1.40 :** a) Effect of twisting on  $C_T$  [43] b) Effect of twisting on  $\eta_P$  [43]

As the effective angle increases, additional lift is generated leading to a large induced drag and associated tip vortex that further decreases the efficiency and thrust output. This can be observed on Figure 1.40 a) and b) that represent the thrust coefficient and efficiency respectively. It was shown that by choosing the appropriate kinematic parameters, thrust generation is nevertheless possible. Also, by selecting low-frequencies it is possible to considerably reduce the interference between the starting and stopping vortices and the unsteady vortex system caused by the finite span.

Hall and Hall [44] under similar conditions used a vortex lattice method combined with a variational method computing the minimum power circulation distribution along the span. They showed that the configuration minimizing the energy losses caused by the vortex system is optimized when the flapping frequency is such that the wing flaps slightly less than once per wingspan forward. This corresponds to Strouhal numbers within the range  $[0.2 ; 0.4]$ . The flow structure behind a heaving and pitching finite span-wing was observed by Von Ellenrieder [45] using dye flow visualisation technique. These experiments highlighted the presence of vortex rings that are being shed. Blondeaux et al. [46] undertook Navier-Stokes computations for comparison to these experiments and confirmed these observations. Figure 1.41 a) and b) illustrate plan and side views respectively, computed for one of the isosurfaces.

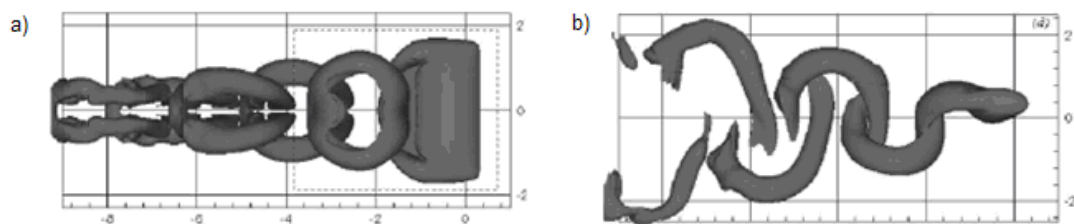


**Figure 1.41 :** a) Plan view of 3D flapping airfoil [46] b) Effect of twisting on  $\eta_p$  [46]

As we can see on part a), the three-dimensional wing generates a series of vortex rings of alternating sign. Figure 1.42 represents schematically this particularity of the flow structure.

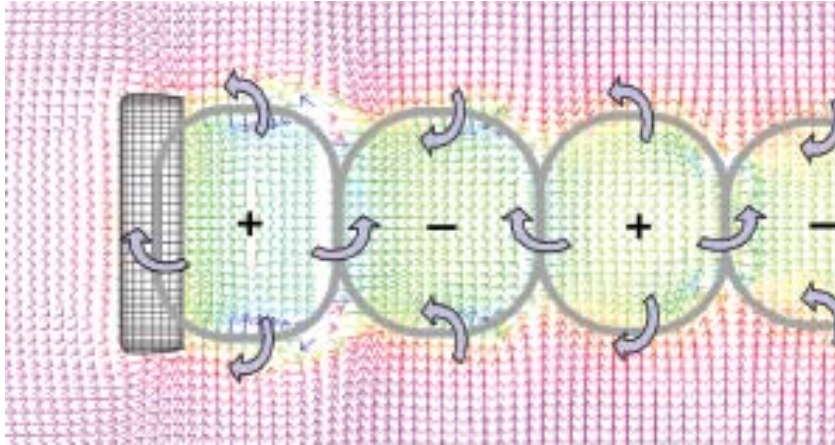


**Figure 1.42 :** Shed vorticity behind a three-dimensional flapping wing

By observing these shed vortices from a mid-span view, the figure indicates that the pattern corresponds to a reverse Karman vortex sheet.



## **2. METHODOLOGY APPLIED TO THE COMPUTATIONAL ANALYSIS**

The objective of this study consists in solving computationally the flow around a given geometry consisting in a flat-plate. The model was chosen in common with other studies which will perform an experimental investigation of the flow. Indeed as we have previously pointed out, it is not simple to correctly model the flow at such low Reynolds numbers. Thus it can be very valuable to compare the two sets of results. In future studies, the aim will be to make use of the 2D or 3D experimental data in order to validate the numerical simulations.

They are several steps that need to be fulfilled to properly perform a CFD Analysis. First of all, an appropriate mesh must be generated around the geometry such that the flow features can accurately be resolved. We may add that reducing the computational effort required to solve the flow, especially in our case which is three-dimensional, is fundamental. While presenting the geometry of the model, we will see that it is possible to considerably reduce the size of the problem by applying the appropriate assumptions. The technique employed to create the mesh will be presented in detail and we will give the important parameters characterizing it. Following this, we will present a brief introduction on Computational Fluid Dynamics focusing on the method we will be using, namely the Finite Volume Method. From the basic principles of conservation, we will develop the mathematical basis leading to the governing equations of fluid flow. Although the low Reynolds number flows under consideration are mainly laminar, it will be shown that these low Reynolds number effects are better represented by including turbulence modeling. Indeed, we will be solving flows in which transition takes place across laminar separation bubbles. Thus the numerical approach must include transition prediction and allow other flow features to be correctly predicted by our computational set-up. In addition to the appropriate turbulence model for these particular flow effects, we will explain what the various possibilities are as far as the wall treatment is concerned and what led us to choose the near-wall approach. Finally, we will conclude on the methodological aspect of the project by going through the setting up procedure of the simulation. Our CFD problem will be defined in terms of initial and

boundary conditions. The implementation of the boundary conditions will be described such that the flow physics combined to the simplifying assumptions are incorporated into the model. The parameters that were used to define the unsteady simulation in the CFD code FLUENT will be summarized. Finally, the flapping motion was applied to the model by making use of a user-defined function. The procedure used to prescribe the unsteady motion will be explained. This chapter will give us the general methodology that is to be respected in order to prepare the CFD simulation suitable to our problem. To solve the flow for a particular case, all these steps must be carried out, applied to the specific flow conditions and motion parameters.

## 2.1 Generation of the Mesh

### 2.1.1 Definition of the model

The geometry that was tested consists of a flat plate of 117 mm chord. Its thickness is of 2.7 mm and all edges are rounded with a radius of 1.350 mm. The technical drawing of the geometry that will be used in the experiments is the following:

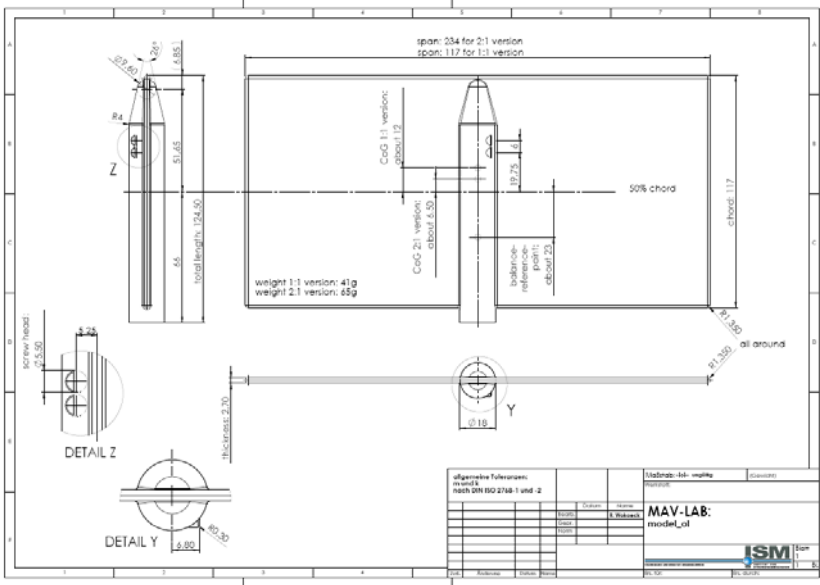


Figure 2.1 : Technical drawing of the flat-plate geometry

As can be seen on the drawing of Figure 2.1, the experimental model presented a cylindrical part along the center line of the flat plate useful solely for its positioning. Therefore it is not relevant to us and has not been represented in the numerical model. We may add that on the above drawing, the span of the model is not precisely

given, instead two possible widths are specified, 117 and 234 mms. We have chosen to simulate the flow around both models in order to investigate the effect that the aspect ratio has on the results. For the parameter variations however, these are performed based on the 2:1 width scale model that is for an aspect ratio equal to 2.

In addition, we consider the geometrical attributes of the model in order to eventually simplify the problem to be solved. Indeed, the flat plate is symmetric. As we consider it positioned such that the main direction of the incoming flow is along the x-axis, it appears sufficient to represent only half of the flat plate. This operation consists in cutting the plate along one of its central axis (x-axis for instance). This implies necessarily that the main stream flow is to be specified along this same axis. The plane used to divide the plate into two identical parts will need to be defined as a symmetric plane in order to counter for this simplification. We will later mention about the boundary conditions in further detail once the mesh generation approach has been presented.

### **2.1.2 Presentation of Gridgen**

For the generation of the mesh surrounding the flat plate, we decided to use the software Gridgen. Since 1984, Gridgen has been used to create three dimensional grids for complex geometries in a production environment. The software origins are in the demanding US aerospace industry where it has a great reputation. It is known for creating high quality grids which is vital for reliable simulations. Due to the enhanced quality of the mesh, it leads to more accurate solutions and faster convergence. Now days, the software is used worldwide in aerospace, automotive, power generation, chemical process and many other industries for which CFD is an integral part of the design process. Gridgen is not limited to any type of geometry, and the resulting mesh can be exported to any type of analysis software to carry out computational fluid dynamics or finite element analyzes for example. We will start by describing the framework that allows any modification to spread throughout the various levels that define the mesh. Indeed, as we construct it we will always be working on a certain level of the data hierarchy of Gridgen, corresponding to one of the four types of data.

The foundation of the data hierarchy is the database. It corresponds to the geometry data that defines the shape of the model around or on which the grid is to be

generated. Typically, the database, consisting of points, curves surfaces ...etc, is created thanks to a computer aided design software and then imported to Gridgen. In our problem, the flat plate's geometry does not rely on a database as it is created by various operations such as translations, revolutions ...etc, that we will later describe.

The other three grid entities of Gridgen's hierarchy are connectors, domains and blocks. These elements are listed in their hierarchical order. Indeed, connectors are at the first level, and correspond to curves along which the grid points are distributed. For these to be completely defined, the shape of the segments composing the curve and the number of grid points must be defined. In addition, the point distribution needs to be specified, for instance we might decide to have a uniform distribution of points or to apply a certain distribution depending on the connector.

Gridgen's mid-level grid elements are domains that represent surface grids. Any type of domain is based on connectors which is why these cannot be created before completely defining its connectors. These can either be structured or unstructured depending on whether quadrilateral or triangular cells are more advantageous. A structured domain is delimited by four edges, each of them composed of one or more connectors. The points are projected to the opposite edge so the two sets of edges must necessarily have the same number of points  $i$  and  $j$ , the minimum and maximum values. Therefore the domain is an array of  $I \times J$  elements. On the other hand, the perimeter of an unstructured domain is defined by an outside edge and possibly an interior edge if it contains holes.

Finally, at the top of the hierarchy are blocks that are based on the previous level of Gridgen, consisting of domains. These represent volume grids in our case since we are constructing a three-dimensional grid. Once again, these may either be structured or unstructured. In the case where it is structured, the block will be composed of  $I \times J \times K$  number of hexahedral elements. As for an unstructured block, it consists of tetrahedral cells or a combination of tetrahedral cells and pyramids. As soon as this highest level of Gridgen's hierarchy of grid elements is fulfilled, the boundary conditions can be specified. While setting them, the groups of domains to which the same type of boundary conditions will be applied should be created. The domains within a certain group are selected and a specific boundary condition can be chosen such as '*velocity inlet*' or '*wall*' if we have selected all the domains composing the geometry's surface. It is actually not mandatory at this stage to decide on the type of

boundary condition since this can be done once the grid is exported to the analysis software, however we should at least regroup the domains and create a custom boundary condition. The last step is to export the grid to the appropriate analysis software which in our case is the 3D version of Fluent.

### 2.1.3 Grid generation technique

The mesh surrounding the flat plate has been generated with the software *Gridgen* that we have just briefly introduced. To obtain the final three-dimensional model and the mesh surrounding it, successive operations had to be undertaken. As mentioned in the previous paragraph, instead of importing the model and from there generating the mesh, we have created the geometry and the grid simultaneously. We will now present the procedure step by step, as well as the important mesh parameters such as the dimensions of the computational domain, the height of the first mesh from the plate's surface, etc... At this stage of the project two meshes were generated for an aspect ratio of 1 and referred to as '*flat\_plate.gg*' and '*flat\_plate\_finer.gg*' and corresponding to the coarser and finer grid respectively. These will be used to perform the grid dependence study that consists in determining how sensitive the results are to the grid. Whenever a certain parameter differs between the two, both values will be specified. We should highlight however that the grid generation technique is identical in both cases, only certain parameters are modified to make the grid '*flat\_plate\_finer.gg*' finer than '*flat\_plate\_finer.gg*'. We will now describe one after the other the various steps that led us to the final mesh.

Let us first of all present the three necessary steps. The objective in the first step was to generate the 2D domain later used to create the rounded-edge that defines the tip of the flat-plate. Indeed, we may obtain such a geometry by rotating a half section of the flat-plate. The following figures created in *Catia* give us an idea of the revolution operation that is carried out in the second step. These have been included to illustrate the 2D half section of the flat-plate on Figure 2.2, and the 3D geometry that is obtained as a result of the operation, on Figure 2.3, as these could be hardly distinguished in the real *Gridgen* mesh.

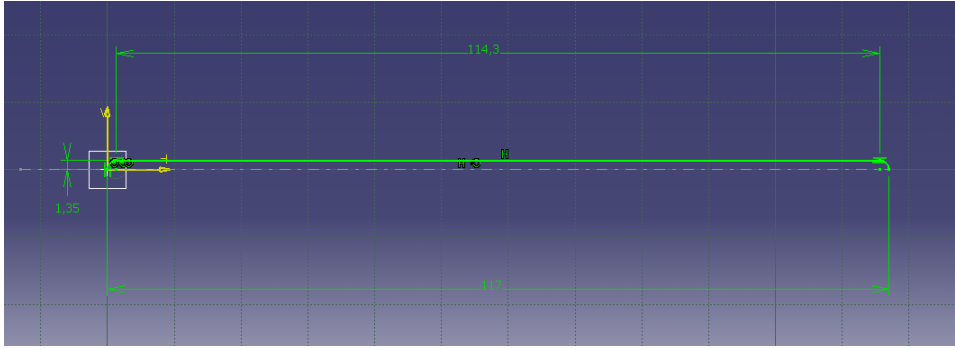


**Figure 2.2 :** Half section of the flat-plate model

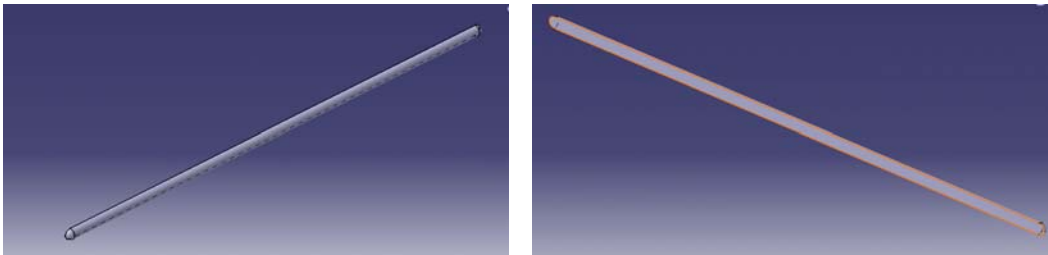


**Figure 2.3 :** a) Flat-plate tip after rotation of the 2D section b) Inside view of the rounded edge

In the final step, the top and bottom surfaces of the flat-plate in the span-wise direction were created. This could be done by translating the flat surface of the rounded edge shown on Figure 2.3 b) by a distance equal to half of the full span. As we can see, the edges that define the domain have been highlighted in orange. By applying these three steps successively, the full geometry of the numerical model, from the tip to the symmetry plan, was defined as shown on Figure 2.4. Once again this is only an illustration of what we obtain in Gridgen.

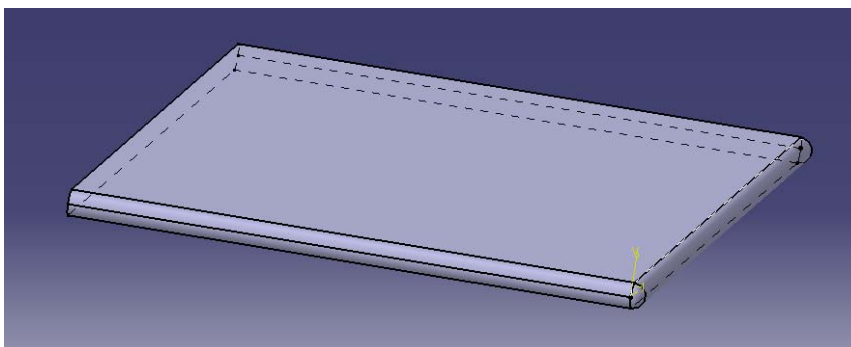


**Figure 2.4 :** Final geometry after applying the translational operation ( $AR = 1$ )

Now that the method applied to obtain the final geometry has been explained, we will focus on the mesh that was generated. However we should always bear in mind that these were achieved simultaneously.

### 2.1.3.1 Extrusion from the 2D section

In this first step, the half 2D flat-plate section was obtained but only at the very end. Indeed, we now have to concentrate on obtaining a good quality grid and this especially holds for the region surrounding the flat-plate surface since it will present the strongest flow gradients. As we have seen in the first part of this report, we expect the unsteady flow to develop a reversed von Karman Vortex street in the wake of the flat-plate due to the shedding of leading and trailing edge vortices. Therefore, the grid close to the surface and in the wake must be defined with great attention; otherwise these flow features will not be accurately predicted. To insure that these are captured correctly, the grid elements must remain small enough. Of course, considering the geometry it is evidently better to create a structured domain in the close surrounding of the flat-plate and needless to say that the quadrilateral cells should remain as square as possible by limiting their skewness. The best way to achieve these objectives appeared to be by making use of the extrusion tool of Gridgen. The structured domain was therefore generated by extrusion from an edge, corresponding to the edge of the complete flat-plate section, as shown on Figure 2.5 below.

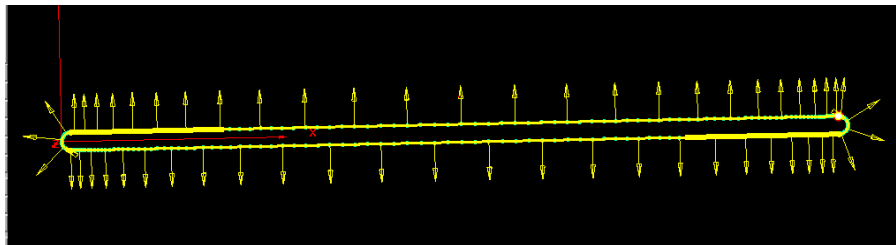


**Figure 2.5 :** Extrusion from the edge of the flat-plate section

At this point, the extrusion parameters had to be specified. These are critical values since the viscous effects related to the boundary layer must be correctly resolved. To do so, the first mesh must be at an appropriate distance from the surface. This depends on the wall treatment and can be calculated accordingly. This aspect of the mesh will be thoroughly discussed in a later section that focuses on the wall approach. Here we will only specify the values assigned to the first height. The second important parameter to enter is the growth rate applied from one mesh to the other. Figure 2.6 illustrates the extrusion process and the importance that should be given to the growth rate:

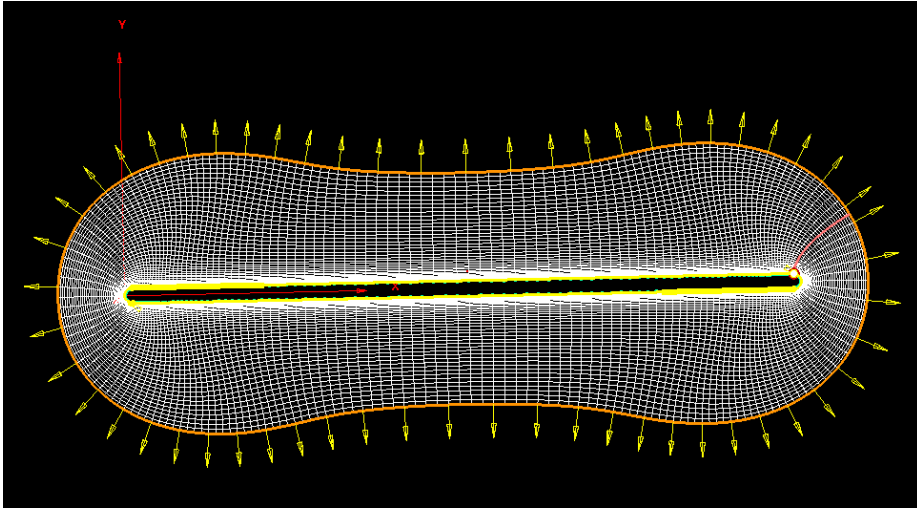


**Figure 2.6 :** Extrusion operation and growth rate

This parameter must be fixed depending on how stretched we allow the elements to be. Close to the surface these must remain very small, but since the first height is so small we should allow the cells to stretch rapidly for the first few iterations, the growth rate is therefore fixed to about 1,1. As soon as these have attained the maximum size that we would allow in the region very close to the surface, they should not increase any further and a growth rate close to 1 is applied. Naturally, as we get sufficiently far from the model, the growth rate slowly increases since the elements can slowly get larger without affecting the results. We will later summarize these numbers for both meshes. We recall that only half of the flat-plate section is useful, so once the extrusion processes is completed, we delete half of the domain as it is symmetric. After extrusion, the resulting mesh around the half geometry is represented on Figure 2.7.

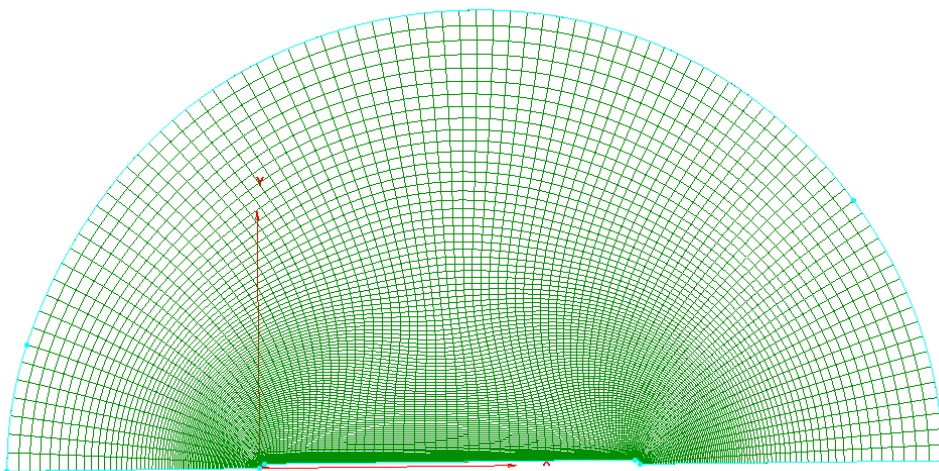


**Figure 2.7 :** Mesh surrounding the half flat-plate resulting from the extrusion process



In the next two figures we have zoomed in that region, first Figure 2.8 part a) shows us the mesh around the complete 2D section of the flat-plate and part b) focuses on the leading edge. We observe that the quadrilateral elements are of good quality as they are not at all skewed, and leave the flat-plate surface orthogonally which is crucial. In addition, we may comment on the point distribution that was applied along the flat-plate connectors. The number of points had to be limited as much as possible since it spreads across the entire domain first in 2D and then in 3D once steps 2 and 3 are carried out. As a result, these numbers can make a huge difference on the total number of nodes of the final grid. For these reasons only 65 points were created on the upper and lower connectors and 22 along the leading edge. However, at the trailing edge we had to bear in mind that the number of points should be high enough to have a sufficient concentration in the wake of the plate since these spread to downstream of the model. Consequently, we defined 33 points along the trailing edge. The points were distributed in such a way that their number would increase as we get closer to the leading and trailing edge since those regions are where the higher flow gradients will appear.

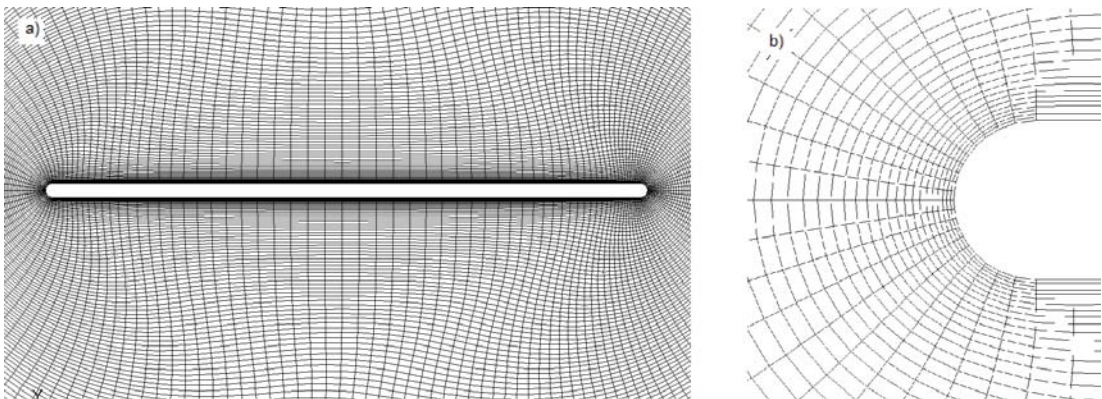


**Figure 2.8 :** a) Mesh surrounding the flat-plate model b) Mesh around the LE

At this stage, the size of the computational domain was decided as the other domains defining the 2D grid around the half flat-plate section are based on those outside connectors. We know that the free-stream conditions are theoretically at an infinite distance from the airfoil. Evidently, while the geometrical characteristics of the CFD domain are to be defined, the outer boundaries have to be fixed at a finite distance from the profile. When CFD calculations are undertaken, the dimensions of the CFD domain are of major importance. We will be imposing boundary conditions on those edges, corresponding to the free-stream conditions. Consequently, if they are not

carefully defined, it will affect the results irreversibly. We could be positioning them very far from the model in order to approach real conditions but at a great cost. The computational effort would be unnecessarily high since time and memory would be wasted. A distance too large is not desired but on the other hand if it is too small we will be introducing errors into the solution. This leads us to choose reasonable dimensions for the CFD domain, for which we know the error is acceptable. As we know, the presence of the flapping plate will particularly affect the flow in its wake. Considering these features, the distance between the plate and the downstream boundary should be large enough. We have positioned it 13 chord lengths away from the model, at a distance of 1521 mm. As for the upstream boundary, it does not need to be so far, it was defined at 5 chords lengths that is 819 mm away. Our references indicated that the following distances are sufficiently far not to affect the results. Figure 2.9 corresponds to the 2D mesh that was obtained at the end of step 1. This is the grid that is used directly in step 2 and rotated around the x-axis.

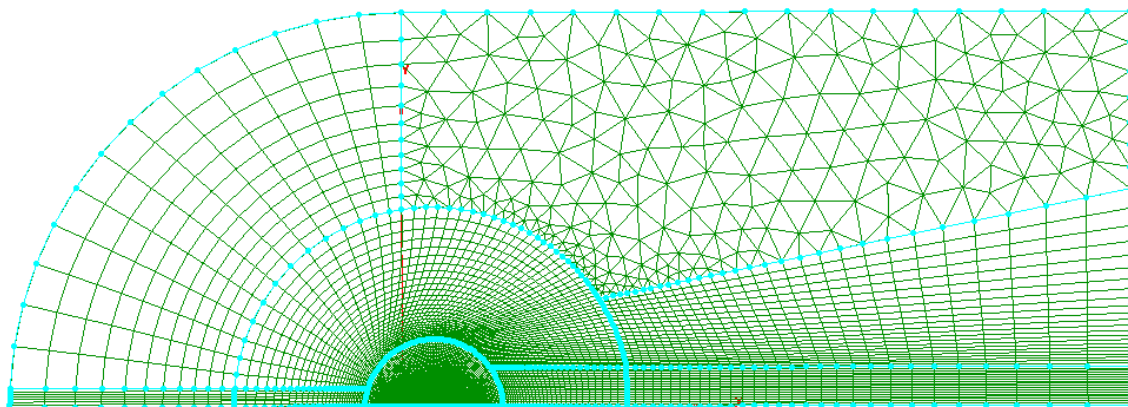


**Figure 2.9 :** 2D mesh obtained at the end of step 1

We may make a few comments on the reasons that brought us to create several domains the way we did on the above picture. The half circular domain at the center results from the extrusion process. This fine region was limited to less than 1 chord length in radius since we are trying to limit the number of nodes as much as possible. However, the mesh must remain fine especially in the wake of the flat-plate. To do so, we created a second circular structured domain. This was done since we could control the point distribution along the outside connector. Thus, the appropriate starting intervals were set and as we get closer to the trailing edge, an increasing density of points could be defined. The rectangular band downstream of the flat-plate

was needed so that enough points would be conserved all across the wake. The rectangular domain upstream on the other hand was created for a different reason. Indeed, while applying the rotation in step 2, the domains in contact with the rotational axis (x axis), need to be structured. The rest of the front part of the 2D mesh was completed by a structured domain also since the number of points in that region was low. At the contrary, it appeared that filling the space downstream with a structured domain would be too costly. This is due to the important number of nodes that had to be created in the downstream direction so that enough nodes are present in the wake. Necessarily these would have to be projected to all the radial connectors including those in the front part of the grid of course. This can be avoided by creating an unstructured domain instead which decreases significantly the final number of nodes. Finally, the link between the domains and particularly those in contact with the circular ones could be very much improved by applying Gridgen's elliptic solver. As we can see on Figure 2.10 a), as it is now some of the elements at the domain boundaries are very distorted.

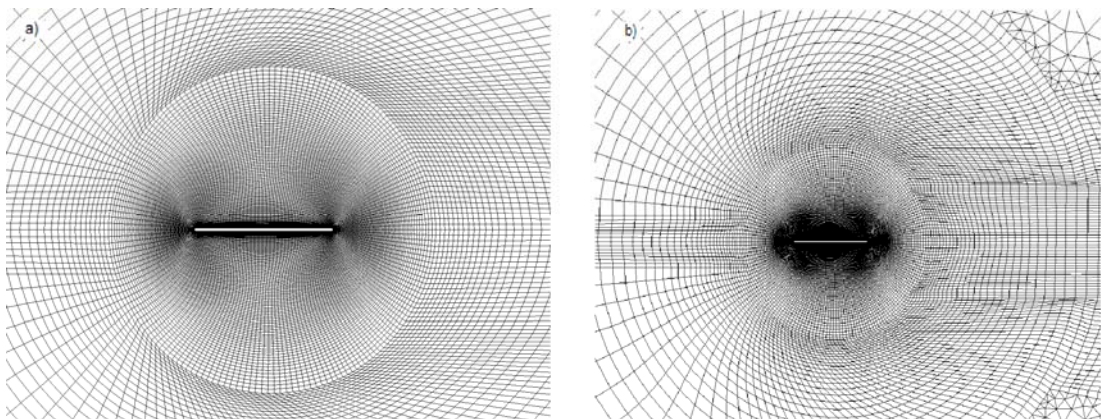


**Figure 2.10 :** a) Mesh before applying the elliptic solver b) Mesh after applying the elliptic solver

To improve the grid quality in those regions we may apply various grid methods available to structured domains. One of them and the easiest to use is the elliptic PDE method that is based on an iterative solution of the elliptic partial differential Poisson equation. As we can see on Figure 2.10 b), after applying it for about 40 iterations to the two circular structured domains, the smoothness, clustering and orthogonality of the grid has been greatly improved. Step 1 of the grid generation methodology is now complete and we may go on to step 2.

**2.1.3.2 Creation of the flat-plate tip by revolution**

In this second step, the final grid obtained previously and represented on Figure 2.9 was used. Up to now we have only completed the second hierarchical level of Gridgen by creating the domains. The analysis software, that is Fluent 3D, has been selected already, therefore to create blocks we must generate volume elements. We recall that a revolution of this 2D mesh is necessary to create the round edge that constitutes the tip of the flat-plate. It is by carrying out this operation represented on Figure 2.11 that the first block is created.

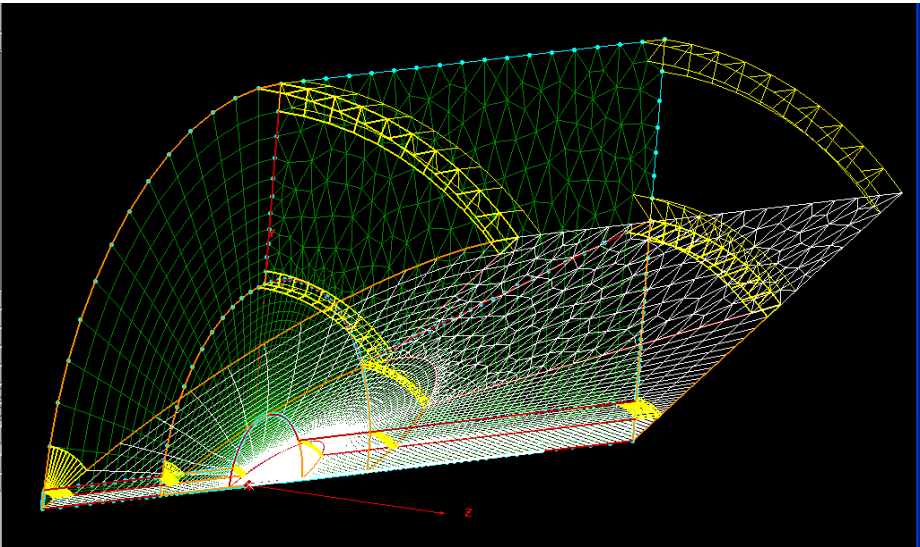


**Figure 2.11 :** Rotation of the 2D mesh surrounding the half flat-plate section

The extrusion tool of Gridgen’s highest hierarchical level is chosen and all the domains contained in the 2D mesh are selected.

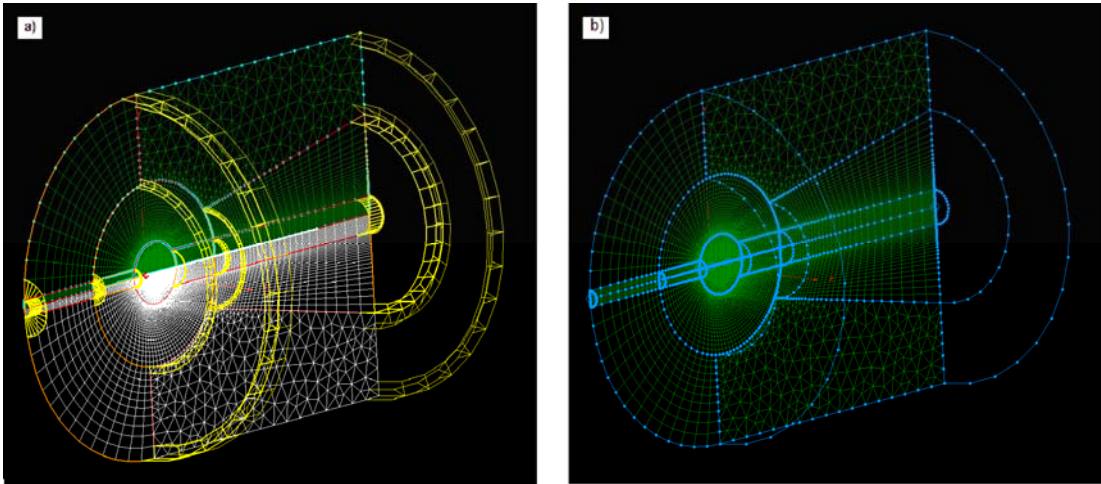


**Figure 2.12 :** a) Total rotational angle of 180 degrees b) Block resulting from the revolution operation

At this point all the extrusion attributes need to be specified. First of all the type of extrusion was chosen to be a rotation. The rotation axis is the x-axis and the total rotation angle is equal to 180 degrees. An important parameter is now fixed, that is the number of iterations performed to reach the total angle. This number is particularly important since our objective is to accurately capture the tip vortices forming in the region surrounding the rounded edge of the flat-plate. We should add that it naturally affects the total number of nodes, and different numbers were chosen for the *'flat\_plate\_finer.gg'* and *'flat\_plate\_finer.gg'* meshes. It was fixed to 16 and 20 respectively. On Figure 2.12 a) and b) we observe first of all the extrusion process achieved by rotation of the 2D mesh for 180 degrees and secondly the block that was obtained by revolution.

### 2.1.3.3 Flat-plate surface by translation

The rectangular top and bottom surfaces of the flat-plate are created in this last step that leads to the final grid used for the computations. It is once again thanks to the extrusion tool that we create this second block. However, the extrusion is carried out by translation this time, and the selected domains are all those contained in the x-y plane of the mesh obtained at the end of step 2. These are highlighted on Figure 2.13 taken as we were carrying out the translation operation. The translational direction is also indicated corresponding to the z-axis.

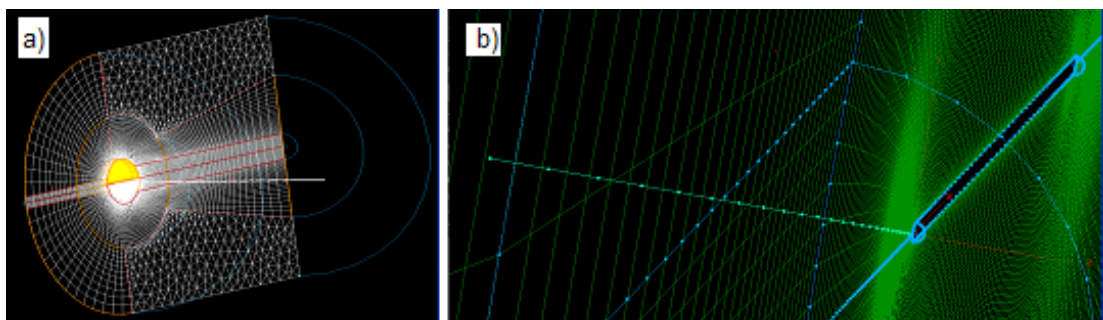


**Figure 2.13 :** a) Selected domains to be translated b) Sub-connector used during the translation operation

As the extrusion attributes, the total distance must be specified which corresponds to half of the span. As it was the case for the revolution, the number of iterations determines the translation interval applied until this distance is reached. However, we have used a different approach since the points must be concentrated towards the tip of the flat-plate in order to capture the tip effects. In the advance settings, it is

possible to define a sub-connector along which the translation is carried out. We have therefore chosen the connector that goes from the tip plane to the symmetry plane separated by a half-span distance. It is orientated in the z direction and goes along the leading edge with (x,y) equal to (0,0). The advantage of defining a sub-connector is that the translational interval does not have to remain uniform. By selecting it while defining the advance attributes, the extrusion follows its point distribution. The number of points and the starting interval had to be decided while creating the connector. Depending on the grid, different numbers were entered, equal to 25 and 35 for the number of nodes and the intervals were fixed to 0,3 and 0,15 mm for the coarse and fine grid respectively. As a result, the geometry is finally completed as shown on Figure 2.14.

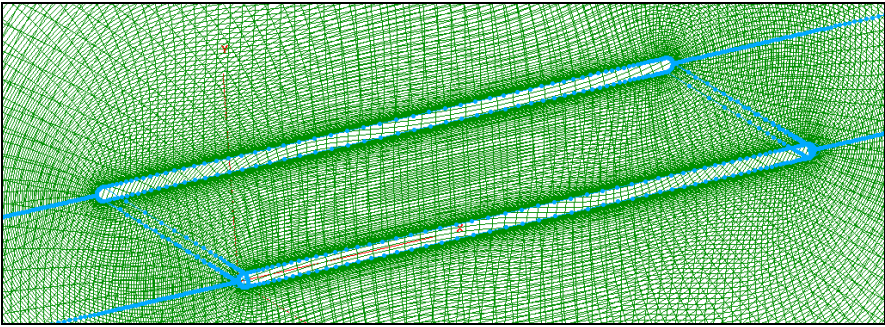


**Figure 2.14 :** Projection of the 2D flat-plate section along the sub-connector

The final grid is obtained, Figure 2.15 was taken for the grid *'flat\_plate.gg'* but for such a global view of the mesh there is no noticeable difference with the finer one.

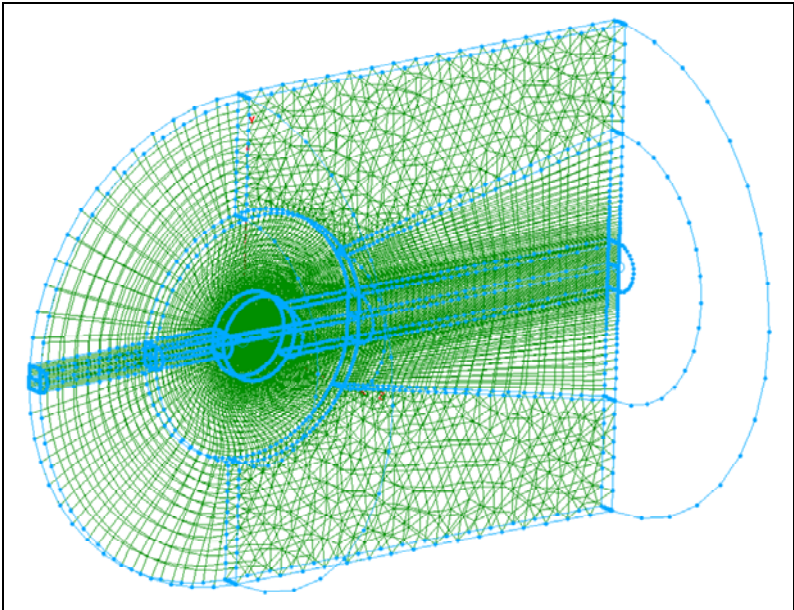


**Figure 2.15 :** View of the final grid

The characteristics that distinguish the two grids are summarized in Table 2.1 below. For each step, the important parameters are mentioned. The *coarse mesh* and *finer mesh* refers to 'flat\_plate.gg' and 'flat\_plate\_finer.gg' respectively.

**Table 2.1:** Characteristic parameters of the coarse and fine grids

		COARSE Mesh	FINER Mesh
<b>step 1: 2D EXTRUSION</b>	<b>First height</b>	0,1 mm	0,05 mm
	<b>Growth rate - N° of iterations</b>	1,1 - 20	1,1 / 30
		1,01 - 40	1,01 / 50
		1,025 - 25	1,025 / 12
	1,05 - 12	1,05 / 14	
<b>step 2: REVOLUTION</b>	<b>Type of distribution</b>	uniform	uniform
	<b>N. of iterations</b>	16	22
<b>step 3: TRANSLATION</b>	<b>Type of distribution</b>	sub-connector	sub-connector
	<b>Sub-connector: N° of points</b>	25	35
	<b>Sub-connector: starting interval <math>\Delta s</math></b>	0.3 mm	0.15 mm
<b>NUMBER OF CELLS</b>		836 224	1 247 310
<b>NUMBER OF NODES</b>		837 180	1 244 390

## 2.2 Finite Volume Method

### 2.2.1 Introduction to Computational Fluid Dynamics

The use of computational fluid dynamics to solve internal and external flows has dramatically increased in the last decade. About twenty years ago, solving fluid flow problems numerically was mainly conducted in research environments but following the wide spread availability of computers combined to the increasing efficiency of solution algorithms, commercial CFD codes have been developed and are now widely used in research, design and development in industry. Computer-based simulations are nowadays used for the analysis of all kinds of systems that involve fluid flow, heat transfer and associated phenomena such as chemical reactions. We may give a few examples:

- marine engineering: loads on off-shore structures
- environmental engineering: distribution of pollutants

- external/internal environment of buildings: wind loading, heating and ventilation
- meteorology: weather prediction
- turbomachinery: flows inside compressors, diffusers etc.
- hydrodynamics of ships
- aerodynamic of air and ground vehicles: lift and drag forces
- biomedical engineering: blood flows through arteries and veins
- design of internal combustion engines

As we can see from the list above, the technique is very powerful and spreads across a wide range of application areas. CFD is progressively becoming a vital component in the design of products and processes. Over experiment-based approaches to the design of fluid systems, the use of CFD leads to a precious reduction in time and cost. For instance, systems that are impossible to study experimentally may be modeled and solved numerically. Very large volumes of results can be produced at virtually no cost, making parametric studies much easier to perform.

In this project we will be using the commercial code Fluent which just like any CFD code is structured around the numerical algorithms that are able to solve fluid flow problems. Like most of the currently available codes, it is based on the finite volume method. To make the program more user-friendly, it is equipped with a user-interface such that the input parameters may be entered, the algorithm run and once the simulation has ended, the results can be examined. Indeed, the code is composed of three elements namely a pre-processor, a solver and a post-processor. Thanks to the pre-processor, the user may specify the inputs of the flow problem through the user-interface and these are then transformed in a form that is suitable for the solver. At this point we should mention that the solver is based on one of the following numerical solution techniques: finite difference, finite element, spectral methods and the finite volume method. The differences rely on the way the flow variables are discretized and the discretisation techniques. The first two make use of local approximations that are gathered by means of point samples and simple piecewise functions respectively. On the other hand spectral methods are valid throughout the entire computational domain by approximating the unknowns using truncated Fourier



series or series of Chebyshev polynomials. Finally the last method which is of interest to us is fundamentally different. Indeed, the finite volume method is characterized by the formal integration of the governing equations of fluid flow over all the finite control volumes of the computational domain. The integral equations are then converted into a system of algebraic equations by replacing the terms by finite-difference approximations. The solution of the algebraic system is then recovered iteratively. In the next paragraph we will explain why the finite volume method is much more attractive and give the governing equations of the flow. The last element of the CFD code is the post-processor. It is also possible to post-process the data using a different program. In our case we have chosen to use the software EnSight. Since our calculations are unsteady, the appropriate variables such as velocity, vorticity or pressure are exported during the run. To avoid having an enormous and unnecessary amount of data, we have chosen to save these 50 times per period. This gives us more than enough information about the time variation of the flow properties throughout a cycle. The data visualization tools include domain geometry and grid display, contour plots, 2D and 3D surface plots, vector plots, particle tracking, etc. In addition, the post-processing may include animations. This feature can be especially useful for our problem in order to dynamically display the unsteady flow patterns.

### **2.2.2 Governing equations given in conservative form**

The governing equations of fluid dynamics can be obtained in various different forms which for a given CFD algorithm can make a huge difference. Indeed, the particular form of the equations can lead to success whereas using an alternate form may lead to oscillations resulting in incorrect results or instabilities. As we know, fluid dynamics is based on the three fundamental physical principles, which are the conservation of mass and energy as well as Newton's second Law. For resolving any fluid problem, we will be confronted to the mathematical statements of the corresponding governing equations of continuity, momentum and energy. Finite volume methods are closely related to finite difference methods. Often it is possible to interpret a finite volume method as a finite difference approximation to the differential equation. However, there is a major difference since they are derived on the basis of the integral form of the conservation law. By using a method in this form guarantees that the discrete solution will be conservative. The integral form forms the

basis for the mathematical theory of weak solutions. Especially in the treatment of discontinuities, the conservative form is much more advantageous. In these type of problems, particularly if a shock-capturing method is used, for which the shock naturally appears, the equations written in non-conservative form would experience the large discontinuity due to the large jump in density and be considerably affected. At the contrary, in the conservative form the mass flux remains constant across the shock. Consequently the finite volume approach is much more appropriate if a stable and accurate scheme is desired. Let us now derive the equations that are obtained in relation to the three conservation laws.

### 2.2.2.1 Mass conservation

This first law states that the mass of a fluid is conserved which brings us to consider the following mass balance:

$$\text{Rate of increase of mass in the fluid element} = \text{Net rate of flow of mass into the fluid element}$$

We consider a small element of fluid and denote the sides as  $dx, dy$  and  $dz$ . On Figure 2.16 are represented the mass flows that enter and exit the element.

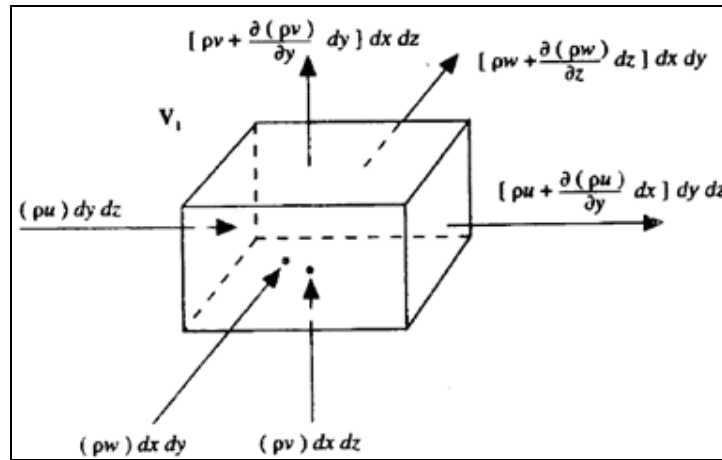


**Figure 2.16** : Mass flows in and out of the element [47]

Let us first write the net outflows in all three directions:

$$x - \text{direction} : \left[ \rho u + \frac{\partial(\rho u)}{\partial x} dx \right] dy dz - (\rho u) dy dz = \frac{\partial(\rho u)}{\partial x} dx dy dz \quad (2.1)$$

$$z - \text{direction} : \left[ \rho w + \frac{\partial(\rho w)}{\partial z} dz \right] dx dy - (\rho w) dx dy = \frac{\partial(\rho w)}{\partial z} dx dy dz \quad (2.3)$$

$$y - \text{direction} : \left[ \rho v + \frac{\partial(\rho v)}{\partial y} dy \right] dx dz - (\rho v) dx dz = \frac{\partial(\rho v)}{\partial y} dx dy dz \quad (2.2)$$

By summing all of these we deduce the Net mass flow:

$$\left[ \frac{\partial(\rho u)}{\partial x} + \frac{\partial(\rho v)}{\partial y} + \frac{\partial(\rho w)}{\partial z} \right] dx dy dz \quad (2.4)$$

The time rate of mass decrease corresponds to the following:

$$-\frac{\partial}{\partial t}(\rho dx dy dz) = -\frac{\partial \rho}{\partial t}(dx dy dz) \quad (2.5)$$

We then equate these two quantities and deduce:

$$\left[ \frac{\partial(\rho u)}{\partial x} + \frac{\partial(\rho v)}{\partial y} + \frac{\partial(\rho w)}{\partial z} \right] dx dy dz = -\frac{\partial \rho}{\partial t}(dx dy dz) \quad (2.6)$$

The above equation corresponds to:

$$\frac{\partial \rho}{\partial t} + \left[ \frac{\partial(\rho u)}{\partial x} + \frac{\partial(\rho v)}{\partial y} + \frac{\partial(\rho w)}{\partial z} \right] = 0 \quad (2.7)$$

The partial differential equation form of the continuity equation in conservation form is given as follow:

$$\boxed{\frac{\partial \rho}{\partial t} + \text{div}(\rho V) = 0} \quad (2.8)$$

### 2.2.2.2 Momentum conservation

Newton's second law states that the rate of change of momentum of a fluid particle is equal to the sum of the forces that are applied to the particle. This equality can be written as follows:

$$\boxed{\text{Rate of increase of momentum of the fluid particle} = \text{Sum of the forces on the fluid particle}}$$

In this section we will only derive the momentum equation in the  $x$ -direction but the procedure to obtain the two other equations in the  $y$  and  $z$  directions is identical. Figure 2.17 below illustrates the forces that are present in the  $x$ -direction:

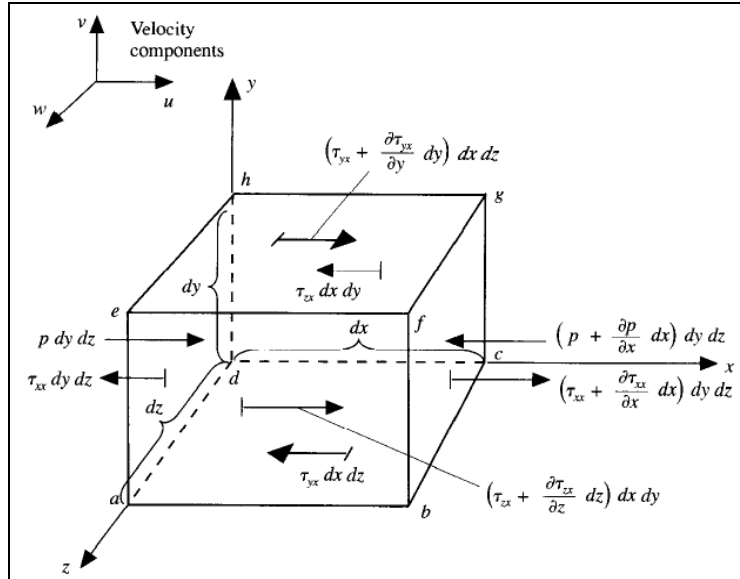


**Figure 2.17:** Forces in the  $x$ -direction [47]

The  $x$  component of Newton's second law is expressed as:  $F_x = m a_x$ . The force in the  $x$ -direction is a combination of the body forces and surface forces. The first kind acts from a distance and can be the gravity force, a centrifugal force or a magnetic force for example. The surface forces act directly on the surface of the fluid element and are of two types, firstly the pressure forces caused by the outside fluid surrounding the element and secondly the viscous forces related to the shear and normal stresses acting on the surface also due to the surrounding fluid. A common practice is to include the body forces in the source terms while the surface sources are kept separately. The rate of increase of momentum in  $x$  per unit volume is equal to the density times the time rate of change of the  $x$ -component of velocity  $u$ .

Therefore it is given by:  $\rho \frac{Du}{Dt}$ .

We may express the body force acting on the element as follows:

$$\text{Body force in the } x \text{ direction} = \rho f_x (dx dy dz) \tag{2.9}$$

where  $f_x$  is the  $x$ -component of the body force per unit mass acting on the fluid element. By adding-up all the forces that are represented on the figure above, we deduce the net surface force in the  $x$ -direction:

$$\begin{aligned}
& \left[ p - \left( p + \frac{\partial p}{\partial x} dx \right) \right] dydz + \left[ \left( \tau_{xx} + \frac{\partial \tau_{xx}}{\partial x} dx \right) - \tau_{xx} \right] dydz \\
& + \left[ \left( \tau_{yx} + \frac{\partial \tau_{yx}}{\partial y} dy \right) - \tau_{yx} \right] dx dz \\
& + \left[ \left( \tau_{zx} + \frac{\partial \tau_{zx}}{\partial z} dz \right) - \tau_{zx} \right] dx dy
\end{aligned} \tag{2.10}$$

We obtain the total force in the  $x$  direction by adding the net surface force and body force in the  $x$ -direction. It is denoted as  $F_x$  and corresponds to:

$$F_x = \left[ -\frac{\partial p}{\partial x} + \frac{\partial \tau_{xx}}{\partial x} + \frac{\partial \tau_{yx}}{\partial y} + \frac{\partial \tau_{zx}}{\partial z} \right] dx dy dz + \rho f_x dx dy dz \tag{2.11}$$

Finally, we deduce the momentum equation in the  $x$ -direction by equating the total force to the rate of increase of momentum. The three momentum equations are given as follows:

$x - direction$	$\rightarrow$	$\rho \frac{Du}{Dt} = -\frac{\partial p}{\partial x} + \frac{\partial \tau_{xx}}{\partial x} + \frac{\partial \tau_{yx}}{\partial y} + \frac{\partial \tau_{zx}}{\partial z} + \rho f_x$	<b>(2.12)</b>
$y - direction$	$\rightarrow$	$\rho \frac{Dv}{Dt} = -\frac{\partial p}{\partial y} + \frac{\partial \tau_{xy}}{\partial x} + \frac{\partial \tau_{yy}}{\partial y} + \frac{\partial \tau_{zy}}{\partial z} + \rho f_y$	
$z - direction$	$\rightarrow$	$\rho \frac{Dw}{Dt} = -\frac{\partial p}{\partial z} + \frac{\partial \tau_{xz}}{\partial x} + \frac{\partial \tau_{yz}}{\partial y} + \frac{\partial \tau_{zz}}{\partial z} + \rho f_z$	

### 2.2.2.3 Energy conservation

The third physical principle states that energy is conserved. This is nothing more than the first law of thermodynamics which says that:

$$\begin{array}{l}
\text{Rate of increase of energy of the} \\
\text{fluid particle}
\end{array} = \begin{array}{l}
\text{Net rate of heat added to} \\
\text{the fluid particle}
\end{array} + \begin{array}{l}
\text{Net rate of work done on} \\
\text{the fluid particle}
\end{array}$$

As previously, the rate of increase of energy is equal to the density multiplied by the time rate of change of the total energy  $E$ . There are two contributions to the energy,

the internal energy caused by the random molecular motion and the kinetic energy related to the translational movement of the element. Thus the total energy is equal to:  $E = e + V^2/2$ , such that the rate of increase of energy is equal to:

$$\text{Rate of increase of energy} = \rho \frac{D}{Dt} (e + V^2/2) \quad (2.13)$$

Let us first of all obtain an expression for the rate of work done by the surface forces on the fluid element. It corresponds to the product of the force and velocity component in the direction of the force. On Figure 2.18 further down are represented the energy fluxes in the  $x$ -direction. Below are given the net rate of work done by the pressure and the shear stresses in the  $x$ -direction:

$$\begin{aligned} \text{Net rate of work} \\ \text{due to pressure} \end{aligned} = \left[ up - \left( up + \frac{\partial(up)}{\partial x} dx \right) \right] dydz = -\frac{\partial(up)}{\partial x} dx dy dz \quad (2.14)$$

$$\begin{aligned} \text{Net rate of work} \\ \text{due to the shear stresses} \end{aligned} = \left[ \left( u\tau_{yx} + \frac{\partial(u\tau_{yx})}{\partial y} dy \right) - u\tau_{yx} \right] dx dz = \frac{\partial(u\tau_{yx})}{\partial y} dx dz \quad (2.15)$$

These quantities are obtained the same way for the two other directions, and by adding all of them up in addition to the body force contribution, we obtain the total net rate of work done on the fluid element:

$$\begin{aligned} & - \left[ \left( \frac{\partial(up)}{\partial x} + \frac{\partial(vp)}{\partial y} + \frac{\partial(wp)}{\partial z} \right) + \frac{\partial(u\tau_{xx})}{\partial x} + \frac{\partial(u\tau_{yx})}{\partial y} + \frac{\partial(u\tau_{zx})}{\partial z} + \right. \\ & \left. \frac{\partial(v\tau_{xy})}{\partial x} + \frac{\partial(v\tau_{yy})}{\partial y} + \frac{\partial(v\tau_{zy})}{\partial z} + \frac{\partial(w\tau_{xz})}{\partial x} + \frac{\partial(w\tau_{yz})}{\partial y} + \frac{\partial(w\tau_{zz})}{\partial z} \right] dx dy dz \\ & + \rho f \cdot V dx dy dz \end{aligned} \quad (2.16)$$

We now focus on the first term that is the net rate of heat added to the fluid element. It can be caused by volumetric heating such as the emission of radiations or heat transfer across the surface due to temperature gradients. It corresponds to the

difference between the rates of heat input and of heat loss. We will denote  $\dot{q}$  as the rate of volumetric heat addition per unit mass. Thus the volumetric heating of the fluid element is given by:  $\rho \dot{q} dx dy dz$

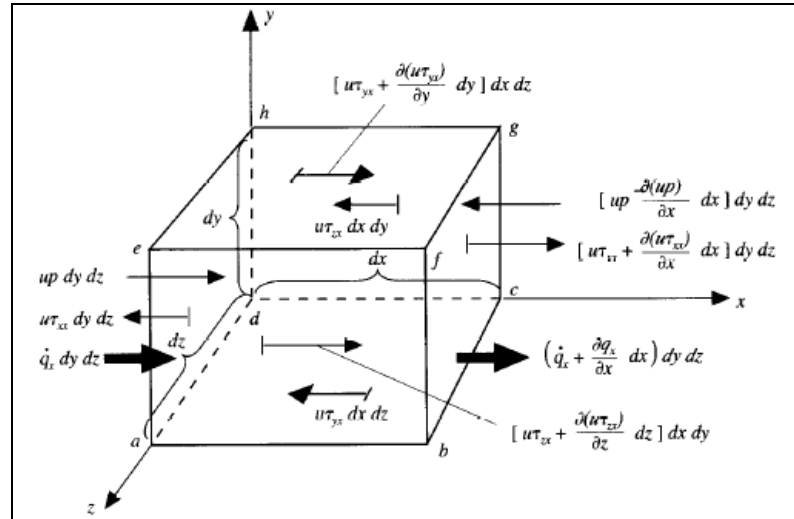


**Figure 2.18 :** Energy fluxes in the x-direction

By observing Figure 2.18 once again, we calculate the net heat that is transferred in the x-direction by thermal conduction:

$$\text{Net heat in the } x\text{-direction} = \left[ \dot{q}_x - \left( \dot{q}_x + \frac{\partial \dot{q}_x}{\partial x} dx \right) \right] dy dz = -\frac{\partial \dot{q}_x}{\partial x} dx dy dz \quad (2.17)$$

As we consider the heat transferred across all faces of the fluid element, the total heating by thermal conduction is obtained:

$$\text{Total heating of the fluid element by thermal conduction} = -\left( \frac{\partial \dot{q}_x}{\partial x} + \frac{\partial \dot{q}_y}{\partial y} + \frac{\partial \dot{q}_z}{\partial z} \right) dx dy dz \quad (2.18)$$

Finally, the net rate of heat added is the summation of the volumetric heating and the heating by thermal conduction. It is equal to:

$$\text{Net rate of heat added to the fluid element} = \left[ \rho \dot{q} - \left( \frac{\partial \dot{q}_x}{\partial x} + \frac{\partial \dot{q}_y}{\partial y} + \frac{\partial \dot{q}_z}{\partial z} \right) \right] dx dy dz \quad (2.19)$$

Fourier's Law of heat conduction states that the thermal conduction is proportional to the local temperature gradient with  $k$  the thermal conductivity such that:

$$\dot{q}_x = -k \frac{\partial T}{\partial x} \quad \dot{q}_y = -k \frac{\partial T}{\partial y} \quad \dot{q}_z = -k \frac{\partial T}{\partial z} \quad (2.20)$$

Therefore we may now express the term above in terms of temperature gradients:

$$\text{Net rate of heat added to the fluid element} = \left[ \rho \dot{q} + \frac{\partial}{\partial x} \left( k \frac{\partial T}{\partial x} \right) + \frac{\partial}{\partial y} \left( k \frac{\partial T}{\partial y} \right) + \frac{\partial}{\partial z} \left( k \frac{\partial T}{\partial z} \right) \right] dx dy dz \quad (2.21)$$

We have all the necessary terms that constitute the energy conservation equation. It is expressed as:

$$\rho \frac{D(e + V^2/2)}{Dt} = \rho \dot{q} + \frac{\partial}{\partial x} \left( k \frac{\partial T}{\partial x} \right) + \frac{\partial}{\partial y} \left( k \frac{\partial T}{\partial y} \right) + \frac{\partial}{\partial z} \left( k \frac{\partial T}{\partial z} \right) - \left( \frac{\partial (up)}{\partial x} + \frac{\partial (vp)}{\partial y} + \frac{\partial (wp)}{\partial z} \right) + \frac{\partial (u\tau_{xx})}{\partial x} + \frac{\partial (u\tau_{yx})}{\partial y} + \frac{\partial (u\tau_{zx})}{\partial z} + \frac{\partial (v\tau_{xy})}{\partial x} + \frac{\partial (v\tau_{yy})}{\partial y} + \frac{\partial (v\tau_{zy})}{\partial z} + \frac{\partial (w\tau_{xz})}{\partial x} + \frac{\partial (w\tau_{yz})}{\partial y} + \frac{\partial (w\tau_{zz})}{\partial z} + \rho f \cdot V \quad (2.22)$$

#### 2.2.2.4 Navier-Stokes equations

To summarize we may say that the equations that we have derived are the three fundamental principles on which fluid dynamics is based. We will be taking into account the viscous effects, therefore friction, thermal conduction and mass diffusion



need to be included in the governing equations. All of these are dissipative phenomena and have been represented in the derivations we have carried out except for the mass diffusion. This transport quantity appears in flows that contain different chemical species as it is the case for chemically reacting flows for instance or non-homogeneous mixtures. This does not apply to our problem which is why the equations have been simplified. To conclude let us give these again as a system of equations that we refer to as the Navier-Stokes equations (for viscous flows). These are valid for an unsteady, three-dimensional and compressible viscous flow:

### Continuity equation

$$\frac{\partial \rho}{\partial t} + \nabla \cdot (\rho V) = 0$$

### Momentum equations

$$x - \text{component} : \frac{\partial(\rho u)}{\partial t} + \nabla \cdot (\rho u V) = -\frac{\partial p}{\partial x} + \frac{\partial \tau_{xx}}{\partial x} + \frac{\partial \tau_{yx}}{\partial y} + \frac{\partial \tau_{zx}}{\partial z} + \rho f_x$$

$$y - \text{component} : \frac{\partial(\rho v)}{\partial t} + \nabla \cdot (\rho v V) = -\frac{\partial p}{\partial y} + \frac{\partial \tau_{xy}}{\partial x} + \frac{\partial \tau_{yy}}{\partial y} + \frac{\partial \tau_{zy}}{\partial z} + \rho f_y$$

$$z - \text{component} : \frac{\partial(\rho w)}{\partial t} + \nabla \cdot (\rho w V) = -\frac{\partial p}{\partial z} + \frac{\partial \tau_{xz}}{\partial x} + \frac{\partial \tau_{yz}}{\partial y} + \frac{\partial \tau_{zz}}{\partial z} + \rho f_z$$

### Energy equation

$$\begin{aligned} \frac{\partial}{\partial t} [\rho(e + V^2/2)] + \nabla \cdot [\rho(e + V^2/2)V] = \rho \dot{q} + \frac{\partial}{\partial x} \left( k \frac{\partial T}{\partial x} \right) + \frac{\partial}{\partial y} \left( k \frac{\partial T}{\partial y} \right) + \frac{\partial}{\partial z} \left( k \frac{\partial T}{\partial z} \right) \\ - \left( \frac{\partial(u\tau_{xx})}{\partial x} + \frac{\partial(v\tau_{yy})}{\partial y} + \frac{\partial(w\tau_{zz})}{\partial z} \right) + \frac{\partial(u\tau_{xy})}{\partial x} + \frac{\partial(v\tau_{xx})}{\partial y} + \frac{\partial(u\tau_{yz})}{\partial y} + \frac{\partial(v\tau_{xy})}{\partial z} \\ + \frac{\partial(v\tau_{xy})}{\partial x} + \frac{\partial(v\tau_{yy})}{\partial y} + \frac{\partial(v\tau_{zy})}{\partial z} + \frac{\partial(w\tau_{xz})}{\partial x} + \frac{\partial(w\tau_{yz})}{\partial y} + \frac{\partial(w\tau_{zz})}{\partial z} + \rho f \cdot V \end{aligned}$$

## 2.2.3 Turbulence modeling

### 2.2.3.1 Introduction

Almost all fluid flow which we encounter in daily life is turbulent. The flow around bluff bodies such as cars, aeroplanes, buildings...etc, are turbulent. The flow within combustion engines, in both piston and gas turbine engines as well as combustors, is

highly turbulent. Air movements in rooms are also turbulent, at least along the walls where wall-jets are formed. Thus, while computing the fluid flow, it will almost always appear to be turbulent. In our case the boundary layer that develops over the flat-plate might also become turbulent as it reattaches and the turbulent trailing vortices should also be correctly modeled. So what is the nature of turbulence? It can first of all be considered as a broadband existing over a wide range of spatial and temporal scales. Turbulence is not at all a bad thing for many applications. For instance, it is helpful in most combustion engines since it efficiently mixes the fuel and the oxidizer. It is also much better able to resist boundary layer separation and wing stall in aircraft applications. However, it comes with a high friction drag penalty. Turbulent flows have a certain number of characteristics that we can briefly describe.

First of all, turbulent flows are '*irregular*', random and chaotic. The flow consists in a spectrum of different scales known as eddy sizes. The largest eddies are of the order of the flow's geometry, for instance the boundary layer thickness with length scale  $l$  and velocity scale  $U$ . The scales extract kinetic energy from the mean flow. The large scales interact with slightly smaller scales to which the kinetic energy is lost. It is through this cascade process that kinetic energy is transferred from the larger scales to the smaller scales. The smallest scales where dissipation occurs are called Kolmogorov scales. At this level, the friction forces become larger and most of the kinetic energy transferred from the larger scales is finally dissipated into internal energy. The characteristic scales of these small eddies are the velocity scale  $\nu$ , the length scale  $l$  and the time scale  $\tau$ . Since the kinetic energy is destroyed by the viscous forces, we naturally suppose that viscosity plays a part in determining these scales. Also we know that the amount of energy to be dissipated is  $\varepsilon$ . Therefore, we assume that these scales are determined by both viscosity  $\nu$  and dissipation  $\varepsilon$ .

The '*diffusivity*' of turbulent flows increases. Consequently, the spreading rate of boundary layers, jets, etc. increases as the flow becomes turbulent. On one hand in a laminar boundary layer, the flow takes place in layers as exchanges of mass and momentum only occur between adjacent layers on a microscopic scale. On the other hand a turbulent boundary layer is marked by mixing across the layers, now occurring at a macroscopic scale. If the flow experiences adverse pressure gradient at

the wall it will cause the flow to slow down. In the case of a turbulent boundary layer, separation is delayed since the velocities are higher at the wall. The velocity distribution takes longer to reach the inflection point that characterizes the transition to separation.

Turbulent flow occurs at '*high Reynolds numbers*'. For example the transition to turbulent flows in pipes occurs when  $Re_D \approx 2300$ , and in boundary layers at  $Re_x \approx 100000$ . Although we will be simulating flows at low Reynolds numbers the laminar transition bubble and the vortices require the modeling of turbulence.

The flow is always '*three-dimensional*'. However, simplification to two-dimensions can be very helpful for the understanding of certain problems, but does remove some important physical mechanisms. It is usually recognized as significantly different from the full turbulence problem.

It has a '*dissipative*' aspect as we briefly introduced while presenting the large and smaller scales. It causes the kinetic energy to transfer from the large eddies to the small eddies. This process of transferred energy from the largest turbulent scales to the smallest is called cascade process.

Finally, even though turbulent flow is composed of small scales as well, they are much larger than the molecular scale and we can treat the flow as '*continuum*'.

### 2.2.3.2 Turbulence models

It is necessary to decompose the instantaneous variables into a mean value and a fluctuating value.  $\bar{X}$  represents the time-averaged part and is independent of time for a steady mean flow, whereas  $x$  is the fluctuating part. For example, the pressures and velocities are rewritten as:  $P = \bar{P} + p$  &  $U_i = \bar{U}_i + u_i$ .

Indeed, this decomposition is useful because while measuring the flow, we are interested in the mean values of these variables and not their time history. For numerical resolutions, if the flow was always to be considered as time dependant, which is always the case since turbulent flows are unsteady by nature, it will require a very fine resolution in time. Therefore, when experimental and numerical results are compared, it is the mean values of pressure, temperature..., etc. that we compare. For instance, the pressure probes' computerized system is automatically averaging

the values in time, just like the steady numerical simulation is doing. To solve the flow, the Navier-Stokes equations are considered:

$$\frac{\partial \rho}{\partial t} + (\rho U_i)_{,i} = 0 \quad (2.23)$$

$$\frac{\partial \rho U_i}{\partial t} + (\rho U_i U_j)_{,j} = -P_{,i} + [\mu(U_{i,j} + U_{j,i} - \frac{2}{3} \delta_{ij} U_{k,k})]_{,j} \quad (2.24)$$

As far as the notations are concerned, ‘ $i$ ’ and ‘ $j$ ’ indices refer to the term’s derivative with respect to  $x_i$  and  $x_j$  respectfully. The next step is to replace the decomposed variables into equations (2.23) and (2.24). We make the assumption that the flow is incompressible, meaning that density does not depend on pressure. We obtain the time averaged Navier-Stokes equations:

$$\frac{\partial \rho}{\partial t} + (\rho \bar{U}_i)_{,i} = 0 \quad (2.25)$$

$$\frac{\partial \rho \bar{U}_i}{\partial t} + (\rho \bar{U}_i \bar{U}_j)_{,j} = -\bar{P}_{,i} + [\mu(\bar{U}_{i,j} + \bar{U}_{j,i} - \overline{\rho u_i u_j})]_{,j} \quad (2.26)$$

The dilatation term of equation (2.24) was neglected due to incompressible effects and an additional stress term  $\overline{u_i u_j}$  appears in (2.26) due to turbulence, created by the fluctuating velocities existing within the flow. This term, called the *Reynolds stress tensor* is unknown and needs to be determined to close the equation system. Indeed we have ten unknowns (3 velocity components, 6 stresses and the pressure) for only four equations (continuity equation and the 3 components of the momentum equation). This is known as the *closure problem*. To close the equation system, several levels of approximations can be used, thus generating different types of turbulent models that we will now briefly describe.

For zero-equation models, an assumption is needed to relate the Reynolds stresses to the velocity gradients via the turbulent viscosity. This relation is called the *Boussinesq assumption* and allows us to replace the Reynolds stress tensor by the product of the turbulent viscosity times the velocity gradients. The turbulent viscosity is often referred to as *eddy viscosity* and leads to *eddy viscosity models*. The particularity of these models is that they do not require the solution of any additional

equation and are calculated directly from the flow variables. These models are very useful for simple flow geometries or initial phases of a computation but are too simple for general situations. They are not able to account properly for convection and diffusion of turbulent energy.

For one equation models, a transport equation is solved for a turbulent quantity which is usually the turbulent kinetic energy. The equation for the turbulent kinetic energy  $k = 1/2 \overline{u_i u_i}$  is derived from the Navier-Stokes equations after making several simplifications which assume that the viscosity is steady, incompressible and constant. A second turbulent quantity is obtained and usually it is the unknown turbulent length scale that is needed. As for the turbulent viscosity it is again calculated thanks to the Boussinesq assumption.

For two equation types of model, two transport equations are solved which describe the transport of two scalars, usually the turbulent kinetic energy  $k$  and its dissipation  $\varepsilon$ . The eddy viscosity is obtained from  $k$  and  $\varepsilon$ . Finally, the Reynolds stress tensor is again obtained by assuming a certain assumption relating the tensor to the velocity gradients and the eddy viscosity.

Up to now, eddy-viscosity based models have been dominating in the context of industrial flow computations. However, the required degree of accuracy and the flow complexity are both becoming increasingly challenging. For example situations where separation is combined with flow control in highly curved surfaces need more complex models. Standard eddy-viscosity models usually under predict separation tendency. Indeed, the Boussinesq assumption appears to be rather crude. For Reynolds stress models, the aim is to remove the linear Boussinesq hypothesis, and replace it with a more general anisotropy relation. Up to then, the production model of the eddy-viscosity based models was insensitive to system rotation. This new and more precise assumption allows the Reynolds stress models to get much closer to the flow physics occurring in reality.

The order in which we have listed these different types of turbulence models has its importance since they are becoming more and more complex and expensive in terms of computational time. We have chosen to use the  $k-\omega$  turbulence model as it has proved to be very accurate for these types of flows.

## 2.2.4 Wall treatment

The numerical approach we use close to the wall is of major importance because large gradients in temperature and velocity occur in that region. Consequently, walls are the main source of turbulence. Near them, the flow is fully turbulent; while further away the turbulence is increasingly intermittent. The boundary layer can be divided into three layers.

### 2.2.4.1 Viscous sublayer

At the wall the turbulent fluctuations have to disappear completely so that the no slip boundary condition is satisfied. Therefore, in a region very close to the wall called the *viscous sublayer*, the fluctuations are assumed to be very small and the time averaged flow must approximately respect this condition, expressed as follows:

$$\nu \frac{d^2 \bar{u}}{dy^2} \approx 0 \quad , \quad \text{after integration :} \quad \bar{u} = \nu \left( \frac{d\bar{u}}{dy} \right)_w \quad (2.27)$$

We will need a variable depending on the velocity gradient and the viscosity, it is called the friction velocity and is defined as:  $u_\tau = \sqrt{\nu \left( \frac{d\bar{u}}{dy} \right)_w}$

We can now define a dimensionless velocity  $u^+$  and a distance normal to the wall  $y^+$  according to the key variables affecting the flow close to the wall flow behavior. Finally, the mean velocity expressed above is rewritten:

$$u^+ = \frac{\bar{u}}{u_\tau} \quad \text{and} \quad y^+ = \frac{y u_\tau}{\nu} \quad \Rightarrow \quad u^+ = y^+ \quad (2.28)$$

This approximation can be applied with good accuracy as long as  $y^+ < 8$ .

We may add that in the viscous sublayer, molecular viscosity makes the flow behave close to laminar.

### 2.2.4.2 Buffer region

Prandtl showed that in this inner region known as the buffer region, viscosity and

friction velocity are still at the same scale than the turbulence. Indeed, the wall is still quite close and therefore the size of the turbulent eddies is limited. Consequently, a direct relation between the two dimensionless variables still exists. Just like previously for the viscous sublayer, a law could be determined experimentally, and appears to be a good fit to this delimited region:

$$u^+ = f(y^+) \Leftrightarrow u^+ = \frac{1}{\kappa} \ln y^+ + b \quad (2.29)$$

$$\text{with: } 0.2\delta > y^+ > 30, \quad \begin{cases} \kappa : \text{von Karman constant} \\ b : \text{additive constant} \\ \delta : \text{boundary layer thickness} \end{cases} \quad (2.30)$$

The exact values of the constants are still being debated and greatly depend on the Reynolds-number range. Within the buffer layer, the laminar and turbulent properties of the flow are both important.

### 2.2.4.3 The outer layer

The outer region of the boundary layer has an edge velocity equal to  $U$  the free-stream velocity. The outer layer is fully turbulent and the turbulent properties play the major role. An outer law for this region has also been developed and is given by this relation:

$$\frac{\bar{u} - U}{u_\tau} = g\left(\frac{y}{\delta}\right) \quad (2.31)$$

Figure 2.19 represents the behavior of  $u^+$  as a function of  $y^+$ , according to the three layers:

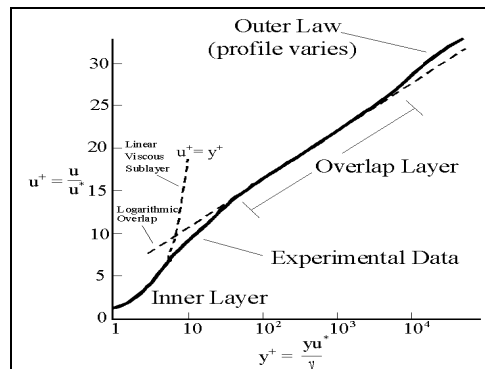


**Figure 2.19 :** Decomposition of the boundary layer into three layers

We will be using the CFD program *Fluent* during our study. The software provides a wide range of modelling capabilities, and for these turbulence conditions, a choice has to be made on what is the best suited turbulence model but also the near wall approach to adopt.

#### 2.2.4.4 Near-wall modelling approach

They are two approaches to solving the near wall problem. These are also illustrated on Figure 2.20.

- Wall function approach, the flow is not solved but given by a function called *wall function*.
- Enhanced wall treatment approach, the mesh is very fine and the flow solved everywhere.

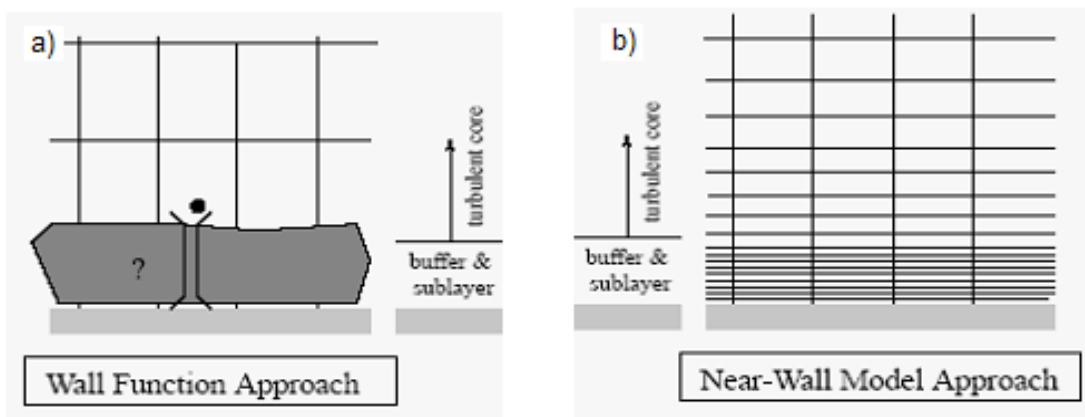


**Figure 2.20 :** a) Wall function approach b) Near-wall model approach

Firstly, let us start by introducing the wall functions. In our simulation, we will be applying a certain turbulence model to capture the turbulent effects (separation bubble...). However, the region it is really valid for initially is far from the wall, known as ‘core flow’. In the “wall function” approach, the turbulent models are not modified for solving the region close to the wall since we do not resolve it. Instead, we use semi-empirical formulas called wall-functions for mean velocities and scalars whereas formulas are more appropriated for evaluating the turbulent quantities. The link between the near-wall-cell solution variables and the respective quantities at the wall are respected. In the software *Fluent*, two different wall functions exist.

The *standard wall function* utilizes a linear law for the mean velocity close to the wall, which then becomes logarithmic further away. One of its major and most



restrictive assumptions is that it assumes local equilibrium by stating that the production of kinetic energy is equal to its dissipation rate. Therefore, this assumes that the wall conditions are directly dissipating the just produced turbulent energy. If we consider these assumptions, it seems like the standard wall functions are most adapted for cases where the viscosity-affected region does not need to be resolved or at least when we are not especially interested in that region. Furthermore, this method becomes less reliable as soon as the hypothesis become non valid of course. When strong pressure gradients occur which is our case, turbulence effects are present in the near-wall region. Consequently, we are in a non-equilibrium situation and we may conclude by saying that the standard wall functions are not suitable to our problem.

The *Non-equilibrium wall function* is particularly recommended for complex flows, where important pressure gradients, rapid changes...etc, occur. Indeed, the log-law used to determine the mean velocity is sensitized to pressure gradient effects. A two layer base allows for computation of turbulent kinetic energy in wall adjacent cells, so that viscous and turbulent layers may be treated correctly. However, the modified wall functions only partly account for the effects of pressure. This technique becomes less reliable when severe pressure gradients that lead to separation occur. Indeed, in this situation we depart too much from the conditions.

The second possible approach is to apply an enhanced wall treatment. The previous near-wall approaches have shown to be unrealistic for the Standard wall functions and unreliable in the case of modified wall functions. Although they are much more 'economic' they are not adapted to our problem. Therefore, we must use the near-wall modelling approach. In this case, there is no separation between regions since the turbulence model will be solving the flow all across the boundary layer until the surface. An enhanced wall treatment will be computationally more costly since it is accompanied by a considerable refinement of the mesh. The mesh needs to be much closer to the wall so that the modified turbulent model is implanted right into the viscous sub-layer of the boundary layer. These modifications have to be global so that they adjust automatically according to the distance from the wall. Indeed, this single model has to be valid everywhere, near the wall and in the core flow. We may conclude by saying that this approach provides us with the necessary precision and is the best-suited method for our problem. Thus, the *transitional flow option* will be

enabled. As a result, the wall shear stress is obtained from the laminar stress-strain relationship. The corresponding mesh guidelines for this option are to considerably refine the boundary layer mesh. The first cell is required to be contained in the viscous sub-layer, that is: *At the wall adjacent cell*  $\rightarrow y^+ \approx 1$

However, a higher  $y^+$  is acceptable as long as it is well inside the viscous sub-layer:

$$y^+ < 5$$

#### 2.2.4.5 Calculation of the first mesh height

Now that the near-all approach has been chosen, we can follow the requirements in terms of mesh refinement and calculate the appropriate distance between the flat-plate surface and the first cell. At this point we need to consider the flow conditions that will be applied in this project. More precisely the Reynolds number is the parameter of interest. It is fixed to 60000 and is kept constant throughout the study. Let us start by giving the necessary parameter values and then derive the calculation procedure that provides us with the value of the first height. The flow and geometric parameters are given by equation (2.32).

$$\begin{aligned} \text{Free-stream air conditions} & \begin{cases} \rho = 1.225 \text{ kg / m.s} \\ \mu = 1.7894 \times 10^{-5} \text{ kg / m}^3 \end{cases} \\ \text{Reynolds-number} & \rightarrow \text{Re} = 60000 \\ \text{Chord length} & \rightarrow c = 0.117 \text{ m} \end{aligned} \quad (2.32)$$

Based on the Reynolds number definition and knowing the flat-plate length and the free-stream air conditions, we may deduce the free-stream velocity:

$$\text{Re} = \frac{\rho U_\infty c}{\mu} \Rightarrow U_\infty = \frac{\text{Re} \mu}{\rho c}, \quad U_\infty \approx 7.491 \text{ m/s} \quad (2.33)$$

The dimensionless wall distance and the distance to the nearest cell are related by the friction velocity and the local kinematic viscosity. In turn the friction velocity depends on the wall shear stress that can be calculated from the skin friction coefficient. All these relations are expressed as follows:

$$\begin{aligned}
y^+ &= \frac{u_*}{\nu} y \\
u_* &= \sqrt{\frac{\tau_w}{\rho}} \\
\tau_w &= \frac{1}{2} \rho C_f U_\infty^2
\end{aligned}
\left\{ \begin{array}{l}
u_* \text{ Friction velocity (m.s}^{-1}\text{)} \\
\nu \text{ Local kinematic viscosity (m}^2/\text{s)} \\
y^+ \text{ Dimensionless Wall distance} \\
y \text{ Distance to the nearest cell (m)} \\
\tau_w \text{ Wall shear stress (Pa)} \\
C_f \text{ Skin friction coefficient} \\
\rho \text{ Fluid density}
\end{array} \right. \quad (2.34)$$

We undertake a coarse calculation in order to get an idea of the order of magnitude of the skin friction coefficient. From it we can deduce an estimated value for the wall shear stress. This simulation is run for a mean-angle of attach of 8 degrees as it will be the most common value throughout the study. The distribution of skin friction coefficient over the flat-plate surface is represented on Figure 2.21:

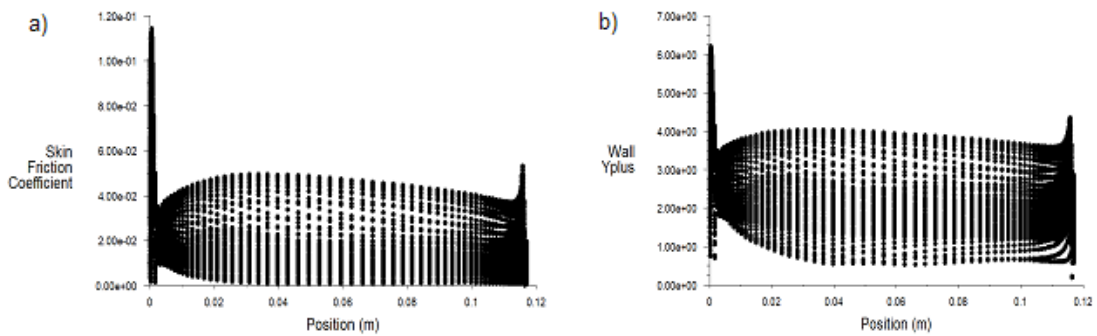


**Figure 2.21 :** a) Skin friction over the flat-plate surface b)  $y^+$  values over the flat-plate surface

From the  $C_f$  values plotted above we observe that the maximum values around 0,12 appear at the leading-edge, however the wall friction is more than twice as small on the rest of the surface without ever exceeding 0,05. In order to limit the size of the mesh, we consider that  $y^+$  values around 5 are satisfactory. We proceed with the calculation for which we obtained the following values:

$$\left. \begin{array}{l}
C_f = 5 \times 10^{-2} \\
\tau_w = 1.7185 \\
u_* = 1.1844
\end{array} \right\} y^+ \approx 5 \Rightarrow y \approx 6.2 \times 10^{-5} \text{ m} \quad (2.35)$$

We have rounded up the value of  $y$  to  $10^{-4}$  and generated the mesh 'flat\_plate.gg' based on this value. After setting-up the simulation parameters and running the case

for a sufficient number of iterations, the  $y^+$  values along the flat-plate surface were plotted on Figure 2.21 b). These appear to be satisfactory since the maximum value is about 6 at the leading-edge whereas  $y^+ \in [0;4]$  along all the rest of the geometry. The effect of this first height will be investigated in the mesh sensitivity analysis as the value is divided by two and fixed to 0.05 mm for the finer mesh 'flat\_plate\_finer.gg'.

## 2.3 Set-Up of the Computational Fluid Dynamic Simulation

### 2.3.1 Implementation of the Boundary Conditions

Any CFD problem is defined in terms of initial and boundary conditions. At the end of the grid generating procedure, the exterior surfaces were grouped according to the type of boundary conditions that would later be applied. Consequently, once the mesh exported to Fluent these need to be specified. On Figure 2.22, the various boundary conditions are represented.

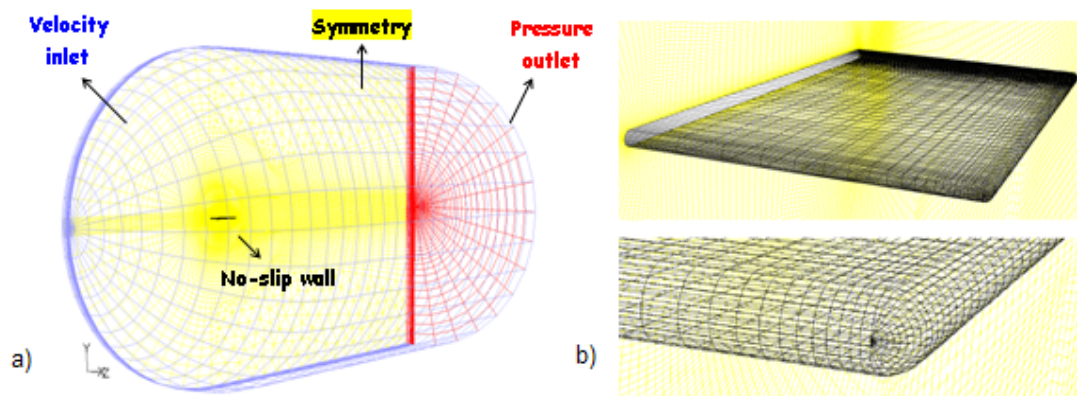


**Figure 2.22 :** a) Boundary conditions applied to the CFD domain b) No-slip wall BC at the flat-plate surface

First of all the distribution of all flow variables needs to be specified at the inlet boundaries. These correspond to the surfaces at the entrance and around the model. They are represented in blue on Figure 2.22 a) and the boundary condition was defined as *Velocity inlet*. The velocity components in all three directions were to be assigned. The mean angle of attack between the flow and the flat-plate is assigned through this boundary condition. In conjunction with the inlet boundary condition, a pressure outlet boundary condition is prescribed to the surface at the exit of the domain shown in red. Indeed, the outlet is located far away from the geometrical

disturbances in order to reach a fully developed state where no changes occur in the flow. It is then possible to assign a constant pressure to the surface corresponding to the free-stream atmospheric pressure. A no-slip wall boundary condition is imposed on the surface of the flat-plate represented on Figure 2.22 b) and finally the mid-span section highlighted in yellow is defined as a symmetric plane.

### **2.3.2 Implementation of the Flapping Motion**

The flapping motion is implemented in the CFD simulation by defining a user defined function (UDF). This feature of Fluent allows us to customize the software so that it fits to our particular problem. Many variables or Fluent models can be accessed through these functions. The UDF is to be programmed and is dynamically loaded to the solver. The source file is written in the C programming language using any text editor and is saved with a .c extension. The code is defined using DEFINE macros that are supplied by Fluent Inc. The first line of the code includes the udf.h file that allows Fluent macros or DEFINE macros to be included during the compilation of the source code. In our case the UDF is compiled (cannot be interpreted) and hooked to the Fluent solver. The process is composed of two separate steps. First of all, a shared object code library is built and then loaded to Fluent. Identically to the Fluent executable itself, the UDF is built with a script called *Makefile* that invokes the C compiler contained in the system such that the object code library is built. After being compiled, the UDF becomes selectable and the function name can be chosen.

As we know, the pitching and plunging motions control the angle of attack and the vertical position of the wing respectively. We are able to impose these through a UDF thanks to the fact that the angular and vertical velocities of the domain can be modified. Let us include one of the UDF source codes as an example. We will first of all explain the commands that are used and then derive the calculations that led us to obtaining the values of this particular case. However, the procedure is to be repeated each time the motion is modified as the kinematic parameters are affected and the UDF is to be updated.

```

#include "udf.h"

DEFINE_CG_MOTION(airfoil, dt, vel, omega, time, dtime)
{
omega[2]=-4.801889198*cos(32.0125946*time);
vel[1]=-1.872736787*cos(32.0125946*time+1.57079633);
Message("time %f, omega %f, vel %f \n", time, omega[2], vel[1]);
}

```

We have used the `DEFINE_CG_MOTION` macro. It is used to control the behaviour of a dynamic mesh. It defines the function referred to as the centre of gravity motion and is activated in the Dynamic Zones panel. The motion of a particular dynamic zone is specified by providing Fluent with the linear and angular velocities at every time step. The node positions of the selected dynamic zone are updated based on these two velocities. In our case, we want the entire domain to perform the flapping motion; therefore the UDF is applied to all surfaces and boundaries of the CFD domain such that it behaves as a non-stationary rigid body. This method has the advantage of avoiding any mesh deformation which would deteriorate the quality of the grid. As we can see, the macro contains six arguments. The first one, *airfoil*, corresponds to the name of the UDF. It is then followed by *dt* which stores the dynamic mesh attributes. These first two attributes are passed by the solver to the UDF. Finally *vel*, *omega*, *time* and *dtime* refer to the linear and angular velocities, the current time and the time step respectively. The UDF on the other hand attributes the linear and angular velocity values as a function of the current time and returns their values to the solver.

Let us now calculate the two velocities as a function of time. In this example, the relevant parameters are the following:  $k = 0.25$  ,  $\lambda = 0.6$  ,  $\alpha_0 = 8^\circ$

We recall that for a Reynolds number of 60 000, a chord length of 0.117 m and the fluid taken as air, the free-stream velocity considered throughout the project is the following:  $U_\infty \approx 7.491 \text{ m/s}$

In addition, the non-dimensional plunge amplitude is held constant and is taken as:  $h = 0.5$  . The corresponding dimensional pitching amplitude is therefore:

$$z_1 = hc \quad , \quad z_1 = 0.5 \times 0.117 \quad \Rightarrow \quad z_1 = 0.0585 \text{ m} \quad (2.36)$$

Consequently, while varying the amplitude ratio it is the pitching amplitude  $\alpha_1$  that will change. Finally, the phase angle between pitching and plunging is held constant such that:  $\varphi = 90^\circ$ , with pitch leading plunge.

We have first of all determined the period and the angular frequency given by equation (2.37) following which the pitching amplitude was calculated in equation (2.38). We then deduced the corresponding pitch and plunge equations (2.39) and finally the equations for the linear and angular velocities (2.40).

$$T = \frac{\pi c}{kU_\infty} \quad , \quad T = \frac{\pi \rho c^2}{k \operatorname{Re} \mu} = \frac{\pi \times 1.225 \times 0.117^2}{0.25 \times 60000 \times 1.7894 \times 10^{-5}} \Rightarrow T = 0.1962723 \text{ s}$$

$$\omega = 2\pi f \quad , \quad \omega = \frac{2\pi k U_\infty}{\pi c} = \frac{2 \times 0.25 \times 7.49044715}{0.117} \Rightarrow \omega = 32.01259465 \text{ rad / s}$$
(2.37)

$$\alpha_1 = 2k\lambda \cdot \frac{z_1}{c} \quad , \quad \alpha_1 = 2 \times 0.25 \times 0.6 \times \frac{0.0585}{0.117} \Rightarrow \alpha_1 = 0.15 \text{ rad} \approx 8.6^\circ$$
(2.38)

$$z(t) = z_1 \cdot \cos(\omega t) \quad \Rightarrow \quad \begin{cases} \alpha(t) = 0.1396 + 0.15 \cdot \cos(32.0126 \times t + 1.5708) \\ z(t) = 0.0585 \cdot \cos(32.0126 \times t) \end{cases}$$
(2.39)

$$\frac{d\alpha(t)}{dt} = -4.8019 \times \sin(32.0126 \times t + 1.5708)$$

$$\frac{dz(t)}{dt} = -1.8727 \times \sin(32.0126 \times t)$$
(2.40)

However, if these two parameters are defined in the UDF based on the above equations, the kinematics of the flat-plate does not match with the desired motion although the amplitudes are correct. After performing several trials, it was proved that small modifications had to be undertaken for the numerical motion to be identical to the exact one:

$$\frac{d\alpha(t)}{dt} = -4.8019 \times \cos(32.0126 \times t)$$

$$\frac{dz(t)}{dt} = -1.8727 \times \cos(32.0126 \times t + 1.5708)$$
(2.41)

Thus, these equations are written in this form in the UDF. The same procedure is repeated as soon as one of the relevant parameters is modified.

### 2.3.3 Fluent parameters

Up to this point, we have discussed in detail about the turbulence model and the wall-approach that have been selected. Now that the boundary conditions have been presented, we will now give all the other parameters that need to be chosen in order to complete the pre-processing of the simulation. The parameters or values that are not specified were not modified, thus the default settings of Fluent apply. Figure 2.23 summarizes all the setting-up of the CFD simulation:

<b>MODEL</b>	<b>SOLVER</b>	solver	segregated	
		formulation	implicit	
		space	3D	
		time	unsteady	
		unsteady-formulation	2nd order implicit	
	<b>ENERGY</b>	gradient option	cell-based	
		energy equation	deactivated	
		<b>VISCOUS MODEL</b>	model	kw
			kw-model	SST
			kw-options	transitional-flows
<b>MATERIAL</b>	<b>NAME</b>		air	
	<b>PROPERTIES</b>	constant density (kg/m <sup>3</sup> )	1,225	
		constant viscosity (kg/m.s)	1,7894E-05	
<b>OPERATING CONDITIONS</b>	<b>PROPERTIES</b>	operating pressure (Pa)	101325	
<b>DYNAMIC MESH</b>	<b>PARAMETERS</b>	smoothing	deactivated	
		<b>ZONES</b>	type	rigid body
		to all surfaces: CG location (m)	X = 0,02925	
			Y = 0 Z = -115,65 (AR = 2) / -57,15 (AR = 1)	
<b>USER-DEFINED FUNCTIONS</b>	<b>COMPILED</b>	buid / load	udf.c	
<b>REPORT</b>	<b>REFERENCE VALUES</b>	length	0,117	
		area	0,013689 (AR = 2) / 6,8445e-3 (AR=1)	
<b>SOLVE</b>	<b>CONTROL SOLUTIONS</b>	pressure-velocity coupling	SIMPLE	
		discretization	2nd order upwind	
	<b>RESIDUAL MONITORS</b>	continuity criteria	1,0E-03	
		x-velocity criteria	1,0E-05	
		y-velocity criteria	1,0E-05	
		z-velocity criteria	1,0E-05	
		k criteria	1,0E-05	
	<b>FORCE MONITORS</b>	CD: force vector	X = cos( $\alpha$ 0)	
			Y = sin( $\alpha$ 0)	
			Z = 0	
		CL: force vector	X = -sin( $\alpha$ 0)	
			Y = cos( $\alpha$ 0)	
			Z = 0	
		CM: moment center	X = 0,02925	
			Y = 0 Z = -115,65 (AR = 2) / -57,15 (AR = 1)	
<b>INITIALIZE</b>	compute from:	Inlet		
<b>ITERATE</b>	time step size	T/1000		
	max.iterations / time step	20		

Figure 2.23 : Fluent parameters



### 3. RESULTS OBTAINED FOR THE FLAT-PLATE MODEL

#### 3.1 Introduction to the Simulation Cases

In this last chapter we will present the results that have been obtained. In the first section, the preparatory work that was necessary before collecting the data is presented. The first step was to check that the user-defined function was perfectly matching with the exact motion. Secondly, it was necessary to determine the appropriate time step in order to optimize the simulations times while making sure that the correct solution was attained. Finally, before exporting the flow field variables we must verify that the flow has reached a periodic behaviour. Thus this last study helped us to establish the number of periods after which periodicity was reached.

After conducting these preliminary studies successfully we may consider the results as trustable. We will start by analysing the results for a given case such that the important features of the flow structures are highlighted. We will particularly concentrate on the formation of the leading-edge vortex and on the three-dimensional effects induced by the tip vortex. The last section will consist in several parameter studies. As discussed previously, the various flapping parameters will affect the flow patterns which in turn will influence the performance of the flapping flat-plate.

**Table 3.1:** Simulation cases

Simulations	Aspect ratio - AR	Mean flow angle - $\alpha_0$ ( $^\circ$ )	Amplitude ratio - $\lambda$	Reduced frequency - k
<b>CASE A</b>	<b>2</b>	<b>8</b>	<b>0.6</b>	<b>0.25</b>
CASE B	1	8	0.6	0.25
CASE C	2	4	0.6	0.25
CASE D	2	8	0.4	0.25
CASE E	2	8	0.75	0.25
CASE F	2	8	0.6	0.15
CASE G	2	8	0.6	0.35
CASE H	2	8	0.6	0.5

The aim is to observe these effects, essentially based on the aerodynamic coefficients, and relate these observations to the differences that can be seen in the

flow field. The parametric studies will consist in varying the aspect ratio of the flat-plate, the mean flow angle, the amplitude ratio and finally the reduced frequency imposed to the flapping motion. We will sometimes need to refer to the various simulations in abbreviated notations instead of giving all the parameter values. Therefore, we have assigned to each simulation a case letter that is given by Table 3.1 above. In each of the parametric study only one of the parameters varies while all the others remain constant. As we can see from the table above, case A will take part in every one of these studies since it is defined by the common parameters. It is this simulation that we will be taken as reference while investigating the flow structure in section 2. To conclude, let us recapitulate the simulations that compose each of the parametric studies:

- Aspect ratio:  $\left\{ \begin{array}{l} \text{case A} \rightarrow AR = 2 \\ \text{case B} \rightarrow AR = 1 \end{array} \right.$
- Mean flow angle:  $\left\{ \begin{array}{l} \text{case A} \rightarrow \alpha_0 = 8^\circ \\ \text{case C} \rightarrow \alpha_0 = 4^\circ \end{array} \right.$
- Amplitude ratio:  $\left\{ \begin{array}{l} \text{case A} \rightarrow \lambda = 0.6 \\ \text{case D} \rightarrow \lambda = 0.4 \\ \text{case E} \rightarrow \lambda = 0.75 \end{array} \right.$
- Reduced frequency:  $\left\{ \begin{array}{l} \text{case A} \rightarrow k = 0.25 \\ \text{case F} \rightarrow k = 0.15 \\ \text{case G} \rightarrow k = 0.35 \\ \text{case H} \rightarrow k = 0.5 \end{array} \right.$

## 3.2 Preparatory Work

### 3.2.1 Verification of the motion

The first step is to verify that the combined pitch and plunge motions that we wish to reproduce are being exactly reproduced numerically. Therefore, the objective in this preliminary study is to check the motion imposed by the user-defined function. In this paragraph we will mention about the procedure allowing us to determine the position of the CFD domain in time. More specifically, we are interested in the angle of attack and the vertical position of the flat-plate. Indeed, these can then be compared to the exact values for the motion to be verified.

We are using the software Enight for the post-processing of the results. Therefore, the case was run with Fluent for an entire period. The data was then exported to Enight. Considering that we are interested in checking the positioning of the motion, the x and y coordinates were exported.

Enight presents a very useful tool that allows us to position cursors anywhere we want in the flow field. Therefore, we have placed two of them at the leading and trailing edges of the flat-plate in order to monitor its positioning.

➤ Calculation of the angle of attack of the airfoil

We have made use of simple trigonometric relations in order to obtain the model's position. The necessary data was limited to the x and y coordinates of the leading and trailing edges. The evolution of these variables in time is recuperated thanks to the cursors we have created. We only have to specify the variables that we wish to observe at these fixed points and save these values. Figure 3.1 was obtained in the post-processing software Enight after the creation of the cursors, to which the relevant distances were added.

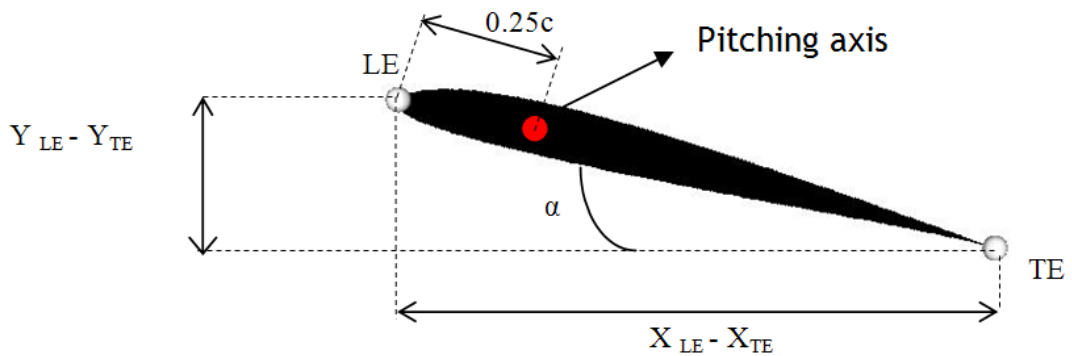


**Figure 3.1** : Cursors positionned at LE and TE

By making use of the above figure, we may deduce that:

$$\alpha = \tan^{-1} \left( \frac{Y_{LE} - Y_{TE}}{X_{LE} - X_{TE}} \right) \quad (3.1)$$

➤ Calculation of the vertical positioning of the airfoil:

To accurately verify the vertical position of the airfoil at any time, the point at which the y-coordinate is considered must be carefully chosen. Due to the pitching movement, it is at the pitching axis that the verification process must take place.

Indeed, it is the only point that is not affected by the changes in angle of attack caused by the pitching. However, we recall that the meshed and therefore resolved area is contained within the CFD domain's outer boundaries and the model's surface. Therefore, the pitching axis, located at 25% of the profile's chord is not part of it, so it needs to be determined. Again it is straightforward to calculate it by applying trigonometric relations. The only required data is again the  $x$  and  $y$  coordinates at the LE and TE as well as the distance between the pitching axis and the LE. In this study it is fixed at 25 % of the chord and will remain unchanged throughout the project. The  $y$  coordinate at the pitching axis is equal to the following, for which the angle  $\alpha$  is given by (3.1):

$$y_{25\%} = -0.25 \cdot c \cdot \sin \alpha + y_{LE} \quad (3.2)$$

➤ Comparison of the exact and numerical motions:

Now that the necessary formulas have been established, the computational angle of attack and vertical position of the plate are to be compared to the exact incidence and  $y$ -coordinate given by the pitching and plunging equations expressed as:

$$\textit{Plunging motion} \Rightarrow \textit{vertical position: } z(t) = z_1 \cdot \cos(\omega t) \quad (3.3)$$

$$\textit{Pitching motion} \Rightarrow \textit{angle of attack: } \alpha(t) = \alpha_0 + \alpha_1 \cdot \cos(\omega t + \varphi) \quad (3.4)$$

Finally we should mention that this checking procedure has been made automatic as much as possible. Indeed, in the incoming studies it will be necessary to verify that the motion under consideration is being accurately reproduced each time it is modified. Therefore, it is in our own interest to make this verification the easiest possible. Let us specify the modifications that still need to be made. First of all the appropriate motion parameters are to be entered in the excel sheet '*motion\_check.xls*'. We recall that the  $x$  and  $y$  coordinates are exported from Fluent to Enight. The cursors are created in Enight at the LE and TE and the data at these two points are saved on an output file from which the information is copied to the Excel sheet. The two comparative curves are then automatically updated.

### 3.2.2 Time step determination

The aim is to determine the appropriate time step. We wish to reach a case where the calculation at every time step ends after only a few iterations (around 10) because the convergence criterion is satisfied, not because the maximum number of inner-iterations has been reached. It is crucial for this requirement to be satisfied; otherwise the solution might not be correct and thus it cannot be considered as reliable. The convergence criterions are set to the following values:

$$\begin{array}{l} \text{continuity} \rightarrow 10^{-3} \\ k \rightarrow 10^{-5} \\ \text{omega} \rightarrow 10^{-5} \end{array} \left| \begin{array}{l} x\text{-velocity} \rightarrow 10^{-5} \\ y\text{-velocity} \rightarrow 10^{-5} \\ z\text{-velocity} \rightarrow 10^{-5} \end{array} \right. \quad (3.5)$$

To determine the appropriate time step we have carried out several trials using different  $\Delta t$  values. These simulations were run without setting any convergence criterions in order to highlight the general trend taken by the residuals.

All of the trials were done by running a journal file. In order to reach the periodic behaviour faster, the first time step was run for about 300 inner iterations such that the flow field could adjust itself to the initial and boundary conditions. Figure 3.2 a) below illustrates the behaviour of the residuals during this first iteration. We observe that 150 iterations is actually sufficient for this first phase as the residuals reach a steady value.

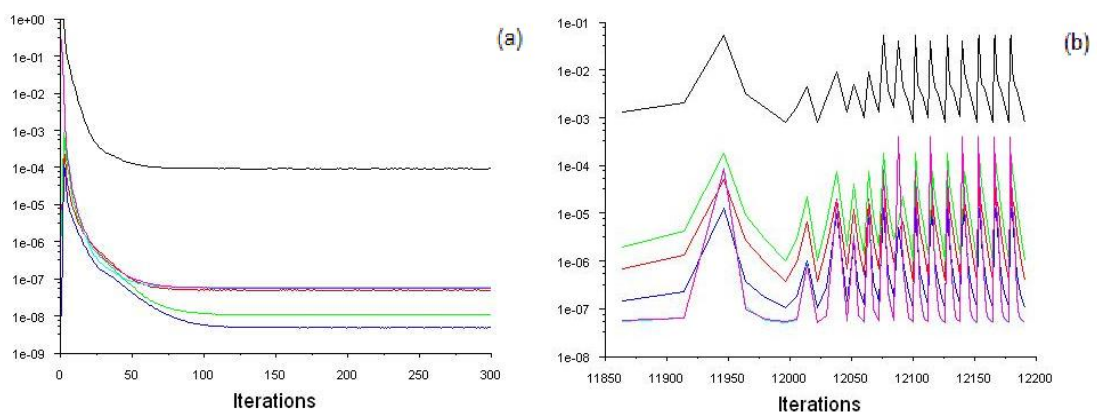


**Figure 3.2 :** a) Residuals during the first iteration b) Behavior of the residuals for  $\Delta t = T/1000$

In the first try, the  $\Delta t$  value was taken equal to  $T/500$ . After more than one period, the continuity residuals finally became smaller than  $10^{-3}$ , but this value could only be

reached after more than 23 inner iterations. This trend was then confirmed throughout the next few periods. We deduced that this time step was too large and unsuitable for our calculations.

The second try was undertaken for a time step twice as small and equal to  $T/1000$ . This time the residuals behaviour was much more satisfactory. Indeed, these satisfied all of the convergence criteria from the very first iteration, after less than 15 inner iterations. This continued to be the case throughout the entire calculation. The typical residual behaviour is plotted on Figure 3.2 b). As can be seen, the residuals are experiencing ups and downs, each of them corresponding to an iteration. As soon as all the convergence criteria are satisfied, the solver proceeds to the following one, and again these decrease very fast since the flow hardly changes between two iterations. Furthermore, the number of necessary inner iterations considerably reduces in time to sometimes reach less than 5 as illustrated below:

iter	continuity	x-velocity	y-velocity	z-velocity	k	omega	time/iter
4449	5.4982e-04	4.3665e-07	1.4999e-06	1.2179e-07	3.4648e-06	3.5764e-06	0:04:58 20
4450	4.1803e-03	2.0085e-06	2.8415e-06	1.5616e-06	1.9574e-03	2.0736e-03	0:05:19 19
4451	3.5783e-03	3.3032e-06	1.1188e-05	1.3269e-06	3.9867e-04	4.2025e-04	0:04:55 18
4452	1.1138e-03	1.4904e-06	5.1786e-06	7.3656e-07	8.1321e-05	8.5342e-05	0:04:29 17
4453	7.4133e-04	8.8180e-07	2.9024e-06	2.4376e-07	1.6672e-05	1.7406e-05	0:04:08 16
! 4454	solution is converged						
4454	5.8385e-04	5.1943e-07	1.6723e-06	1.2992e-07	3.4524e-06	3.5854e-06	0:03:47 15

To complete this study we have compared the drag coefficients that were obtained throughout an entire period. Three different cases were run for which we had  $\Delta t$  equal to  $T/500$ ,  $T/1000$  and  $T/1500$ .

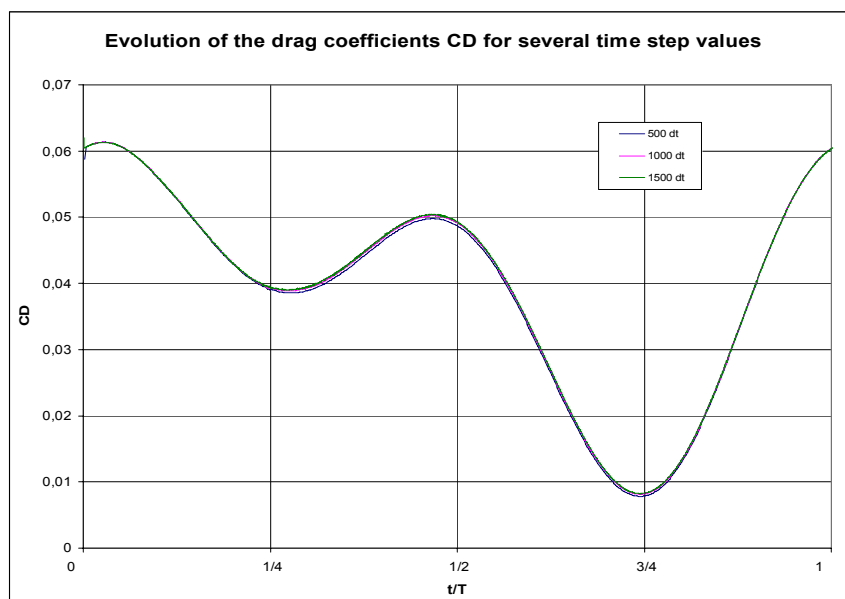


**Figure 3.3 :** Effect of the time step on the time variation of  $C_D$  - case A

We insured that the quantities evolved in a periodic manner before comparing them.

On Figure 3.3 are represented the various results obtained. We observe that a slight difference appears between  $T/500$  and  $T/1000$ , which indicates that the results are still slightly depending on the time step value. However, as it is further decreased this difference disappears and as we compare the curves for  $T/1000$  and  $T/1500$ , these appear to be identical. We deduce that time step independence has been reached and therefore  $\Delta t$  equal to  $T/1000$  is sufficiently small not to influence the results.

We may conclude by saying that a time step corresponding to  $T/1000$  appears to be perfectly adapted to our study. We are insured that the convergence criterions will be satisfied well before the maximum number of inner iterations fixed to 20 is reached. Moreover, only a few inner iterations are required which is essential to us since the running time needs to be optimized. Indeed, the calculations are three-dimensional and thus will require an important computational effort. In addition, we are dealing with a cyclic motion, for which periodicity of the flow must be reached before considering the solution throughout a whole period. Therefore, the time necessary for a single calculation to end is of major concern and this  $\Delta t$  value seems to be optimum.

### 3.2.3 Periodicity of the results

In this paragraph we will briefly discuss about the periodicity of the results. It is essential that before starting to export the relevant variables throughout an entire cycle, the flow is behaving periodically. To check this we may observe the evolution of the aerodynamic coefficients on Figure 3.4 for which we have compared the third and fourth period.

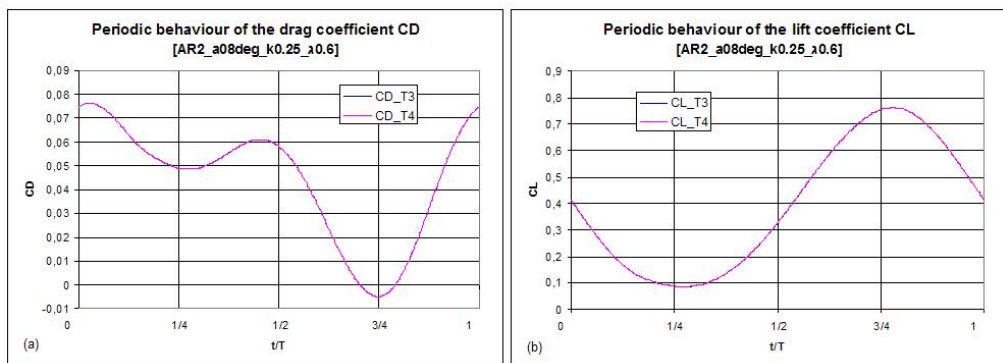


**Figure 3.4 :** a) Periodicity of  $C_L$  – case A b) Periodicity of  $C_D$  – case A

We should however specify that these calculations have been run using first order upwind schemes whereas our future calculations will be second order. Nevertheless this study holds for both configurations. We observe that for both the lift and drag coefficients, the curves are identical. We may conclude by saying that considering the fourth period as reference seems to be sufficient since periodicity is attained already at the third period. We therefore insure that the results are no longer affected by time and are trustable in terms of periodicity of the flow field. This has been applied to all cases which one by one confirmed these observations.

### 3.3 Mesh Effect Study

At the end of the 1<sup>st</sup> section of chapter 2 we presented the characteristic parameters of the two meshes that had been generated, namely *'flat\_plate.gg'* and *'flat\_plate\_finer.gg'* which were created thanks to *Gridgen*. We refer to them as the coarse and the fine mesh respectively. The aim in this study is to investigate the effect that the mesh has on the results. Unfortunately it would be too time costly for us to conduct a full mesh study. Indeed, it would require at the minimum a third mesh and the aim would be to reach grid independency.

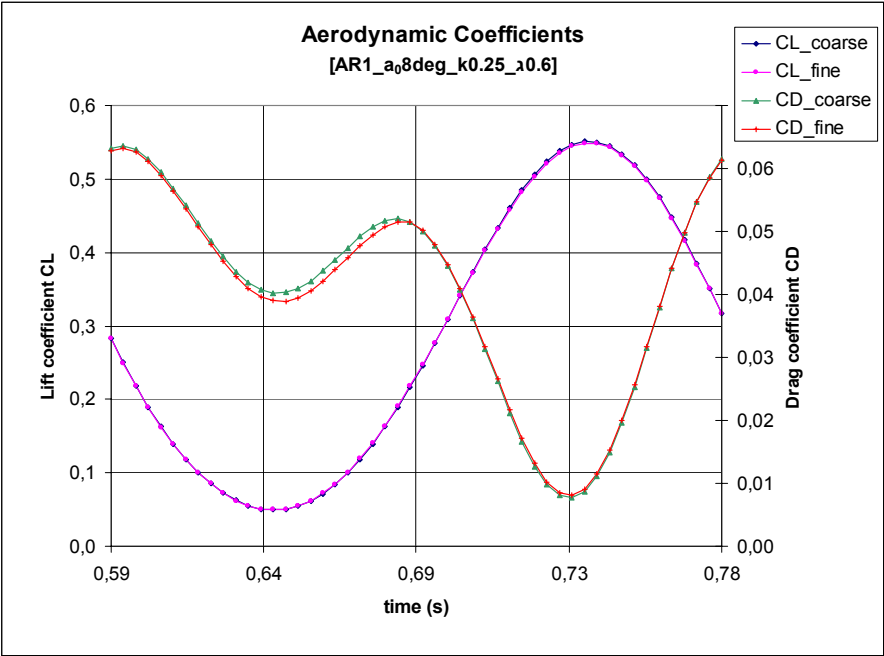


**Figure 3.5 :** Effect of the mesh on the lift and drag coefficients

Here, the objective is limited to comparing the results provided by the two grids in terms of aerodynamic coefficients. We recall that the finer mesh is considerably



larger as it contains about 1 250 000 nodes against only 840 000 for the coarse mesh, therefore we will see if such an increase is worth it by judging of its effect. We have plotted the drag and lift coefficients on Figure 3.5 above. We observe that the differences between the drag coefficient curves are minor as they only slightly differ for a small portion of the period during the second quarter. As far as the lift coefficient curves are concerned, they do not present any noticeable difference. We deduce that increasing the number of nodes by about 50% is unnecessary as it hardly influences the results. We will therefore conserve the height of the first cell and the first spacing from the tip (spanwise direction) equal to those imposed to the coarse mesh. Indeed these were the only two parameters that were modified and divided by two from the coarse to the fine mesh. To conclude on this point we may say that to obtain a noticeable difference related to the mesh density, a much larger grid would need to be used which cannot be considered as it would increase the computational effort beyond the one provided by our resources.

However by further investigating the flow features obtained for the coarse mesh, a problem appeared at the tip. Indeed, due to the mesh generation technique that was employed and specifically step 2 which consisted in creating the tip of the flat-plate by revolution, it is impossible to insure a smooth transition from the flat part of the plate and its rounded edge. Indeed, by nature the equal mesh size between those two regions, imposed on the surface, cannot be conserved throughout the grid.

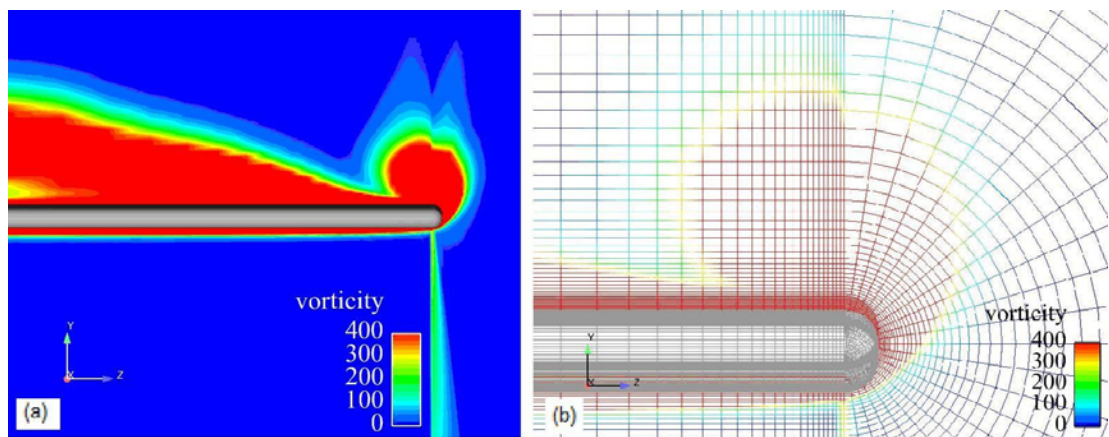


**Figure 3.6 :** a) Vorticity contours at the tip of flat-plate with the coarse grid – case B  
b) Mesh at the tip of the flat-plate with the coarse grid – case B.

The difference progressively increases in the radial direction as we get further from the tip. Very quickly important gaps appear in the tip vortex region, represented on Figure 3.6 b) which introduces important numerical errors. These are shown on

Figure 3.6 a) above. Although completely eliminating the problem is impossible, we have tried to limit its effect by increasing the number of iterations defining the extrusion by revolution that takes place during step 2 of the mesh generation procedure. From 16 points for the coarse mesh we increased the number up to 40. Considering that this mesh defect appears at the transition between the flat and round surfaces, the points were non-uniformly distributed and concentrated in those regions, as shown on Figure 3.7 b). Consequently, the numerical error spreading from the tip is considerably reduced, the improvement is visible on Figure 3.7 a) representing the vorticity magnitude contours. Although we will see later while presenting the results that this defect persists, especially as we progress downstream and the tip vortex increases in size, we decide to keep this grid as the final mesh. Compared to the coarse mesh its size has been greatly increased.

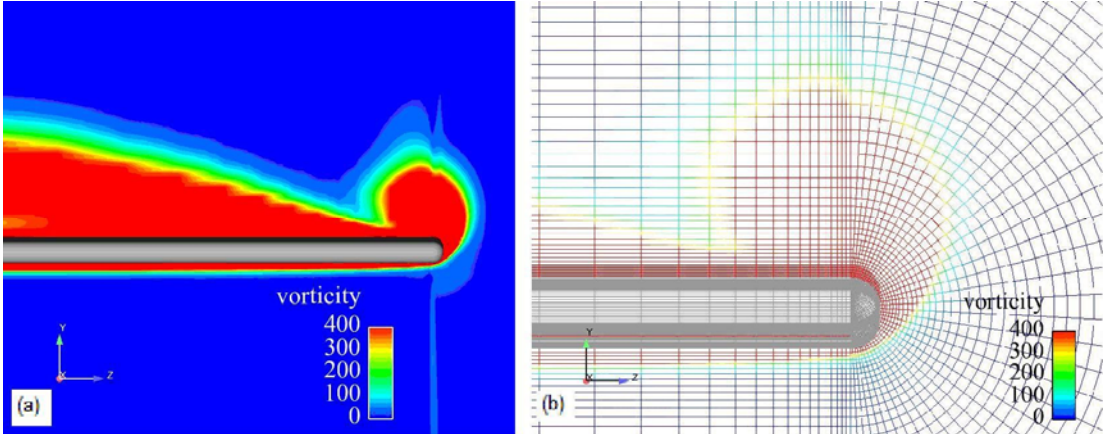


**Figure 3.7 :** a) Vorticity contours at the tip of flat-plate with the final grid – case B b) Mesh at the tip of the flat-plate with the final grid – case B.

**Table 3.2:** Modified mesh parameters characterizing the final grid

		FINAL MESH
<b>step 2: REVOLUTION</b>	Type of distribution	Non-uniform
	N. of iterations	40
<b>step 3: TRANSLATION</b>	Type of distribution	sub-connector
	Sub-connector: N° of points	25 (AR1) / 30 (AR2)
	Sub-connector: starting interval $\Delta s$	0.20 mm
<b>NUMBER OF CELLS</b>		1 136 742 (AR1) / 1 266 820 (AR2)
<b>NUMBER OF NODES</b>		1 130 821 (AR1) / 1 259 662 (AR2)

The total number of nodes is now approximately 1 200 000. Further increasing the number of points at the tip would result in an excessive number of nodes, requiring a far too large computational effort. All the modifications that were implemented to obtain the final mesh are summarized in Table 3.2 above.

### 3.4 Structure of the Flow

#### 3.4.1 Formation of the leading-edge vortex

In this section we will present the results that have been obtained for the simulation case A that will be used as reference in all of the parametric studies. In correspondence to the experimental tests, the simulation parameters have been fixed to the following:

<i>Aspect ratio</i>	→	$AR = 2$
<i>Mean angle of attack</i>	→	$\alpha_0 = 8^\circ$
<i>Reduced frequency</i>	→	$k = 0.25$
<i>Amplitude ratio</i>	→	$\lambda = 0.6$

While post-processing the results, we have made available the necessary information allowing us to analyze the flow structure. The vorticity contours in both chordwise and spanwise directions have been obtained. In order to investigate the three-dimensional effects the contours these were plotted in several planes that are represented on Figure 3.8 below.

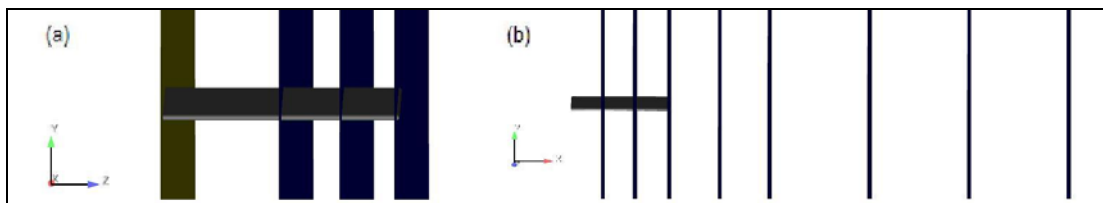


**Figure 3.8 :** a) xy planes in the chordwise direction x b) xz planes in the spanwise directions z

These have been positioned spanwise at the root of the flat-plate, 50%, 75% of its span and at its tip. Chordwise, they were defined at 33% and 66% of its chord as well as at the trailing-edge. To capture the flow evolving in the wake we also have plans at 0.5, 1, 2, 3 and 4 chord lengths from the trailing-edge. We will start by analyzing the flow in the symmetric plane without considering the spanwise variations. The aim is to understand the characteristics of the flow under these conditions and

eventually highlight the formation of a leading-edge vortex. On Figure 3.9 the spanwise vorticity contours are given at four different times throughout the cycle, corresponding to  $t = 0, T/4, T/2$  and  $3T/4$ . We recall that the mean angle of attack between the incoming flow and flat-plate was assigned through the velocity inlet conditions; therefore it is not visible in any of these plots. Consequently at  $t = 0$  for instance, the model appears to have no incidence whereas in reality there is 8 degrees incidence. We observe that the vorticity contours vary importantly as the rates of rotational spin around the  $z$  axis change according to the angle of attack and plunge position.

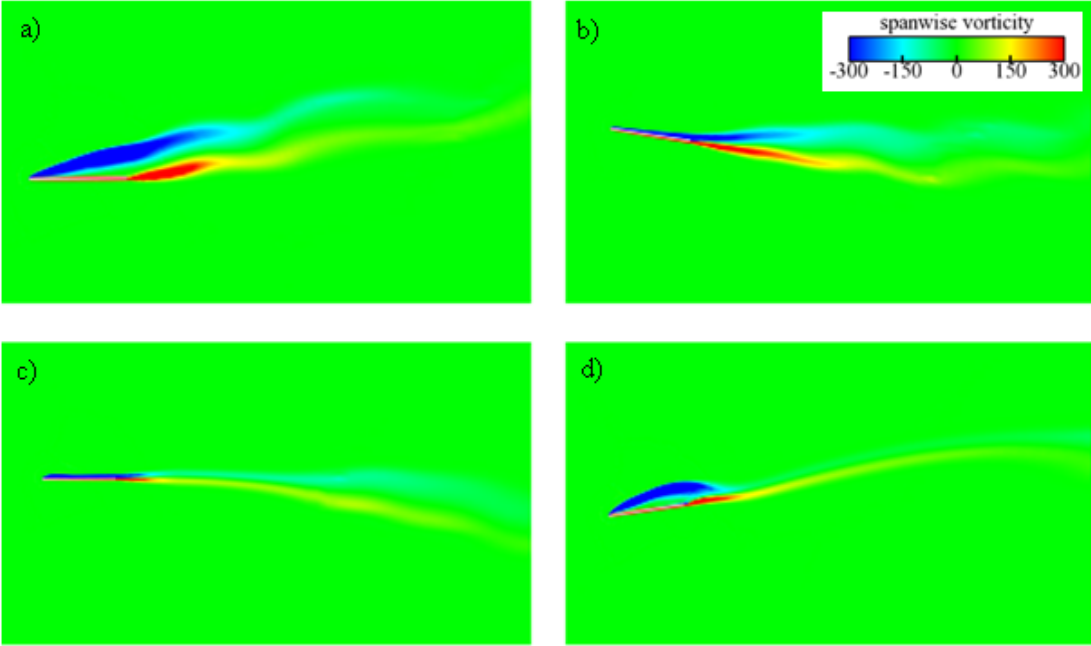


**Figure 3.9 :** Spanwise vorticity contours in the symmetry plane - cased A a)  $t = 0$  b)  $t = T/4$  c)  $t = T/2$  d)  $t = 3T/4$

No reversed Von Karman vortex street appears in the wake of the flat-plate however, which is most probably related to the coarse grid that is used which leads to the dissipation of these vortices. Although some flow rotation is present these cannot be distinguished.

These contour plots can help us to understand the flow structure that develops throughout the cycle. Combined to the velocity vectors present in the symmetry plane and the pressure coefficients along the chord of the flat-plate, we will start by commenting on the formation of the leading-edge vortex. Let us first of all give the graphs that describe the flapping motion of the flat-plate.

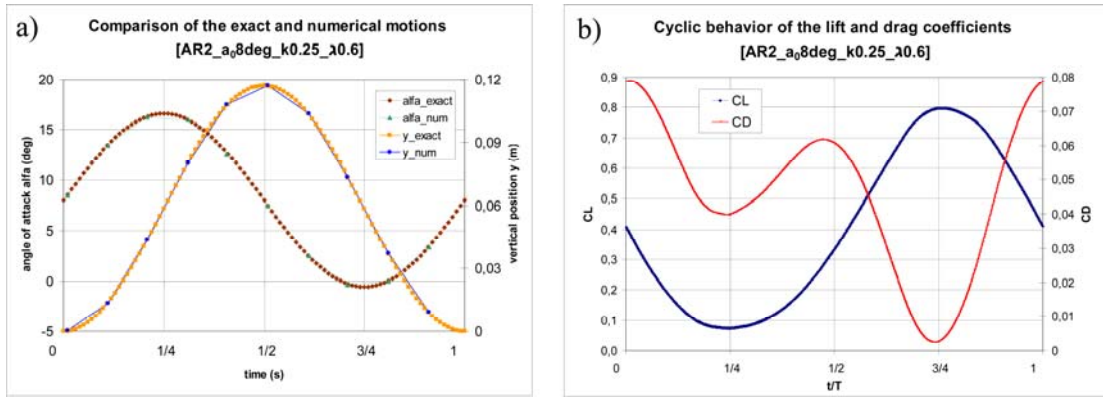


**Figure 3.10 :** a) Kinematics of the flapping motion – case A b) Behavior of the  $C_D$  and  $C_L$  in time – case A

On Figure 3.10 a) is plotted the incidence and plunge position of the model throughout the cycle. The verification of the motion applied numerically was carried out and appears to perfectly match the exact motion. On Figure 3.10 b) the periodic behavior of the lift and drag coefficients can be found. Their evolution across the period will be described in correspondence to the velocity vector flow fields and pressure distributions. We remark however that the drag coefficient remains positive across the whole period indicating that thrust is never generated at any moment during the cycle. We may conclude that unfortunately these simulation parameters necessarily result in a drag-producing case.

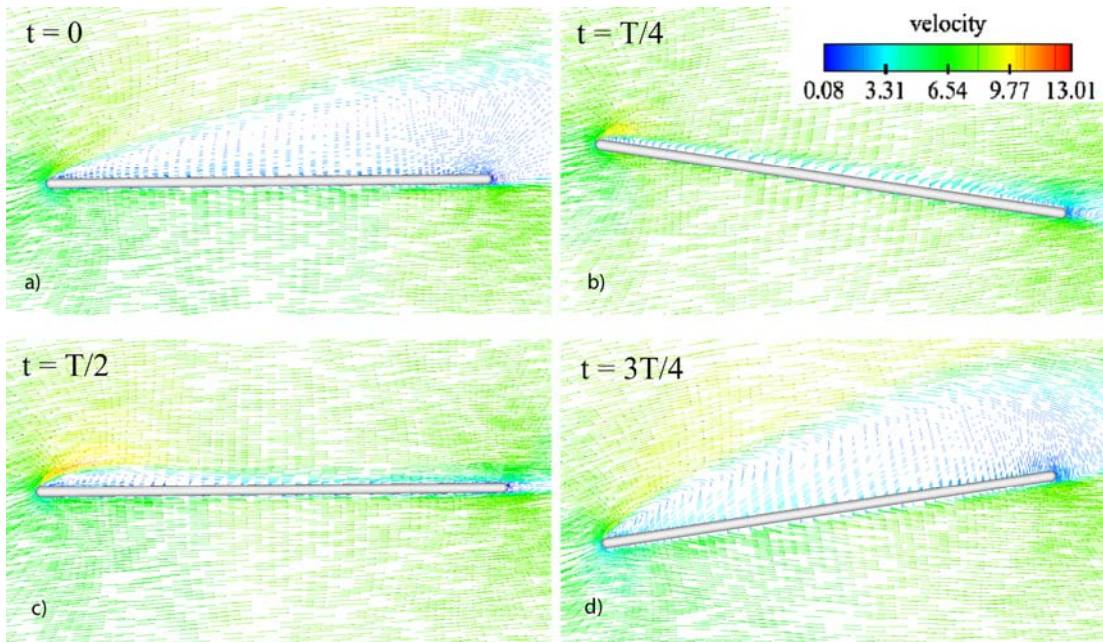


**Figure 3.11 :** Velocity vector flow fields fields – case A a)  $t=0$  b)  $t=T/4$  c)  $t=T/2$  d)  $t=3T/4$

In addition, we observe that the lift force varies symmetrically around a certain value equal to the lift force generated at the mean flow angle  $\alpha_0$ . This is due to the up-and-down symmetrical movement of the flat-plate. The velocity vectors are represented on Figure 3.11 from a) to d). We observe that at  $t = T/4$  which corresponds to the maximum angle of attack at the centre position, the flow is fully-attached and the lift is at its lowest value. It is from this point on that the leading-edge vortex starts forming, up to time  $T/2$ . Let us refer to the pressure distributions, for which the pressure coefficient values, minus  $C_p$  however, are plotted for both the upper and lower surfaces. The above and bottom curves correspond to the upper and lower surface distributions respectively. From Figure 3.14 we may relate the observations made based on the velocity vectors to the pressure distributions. Indeed, we see that after the sudden rise at the leading-edge corresponding to the highest velocities, the  $-C_p$  values directly decrease from the maximum value to the lowest one at the trailing-edge. This region is known as the recovery region and indicates the extent of a possible separation region. At this time ( $t = T/4$ ), since the pressure does not experience any flatter portion in the distribution, we conclude in confirmation to the velocity vectors, that no recirculation region exists.

However, between the quarter and half period, the flow characteristics change considerably as a small separation bubble appears and is visible at time  $T/2$ , referred to as a leading-edge vortex. Figure 3.12 a) focuses on the leading edge at this time.

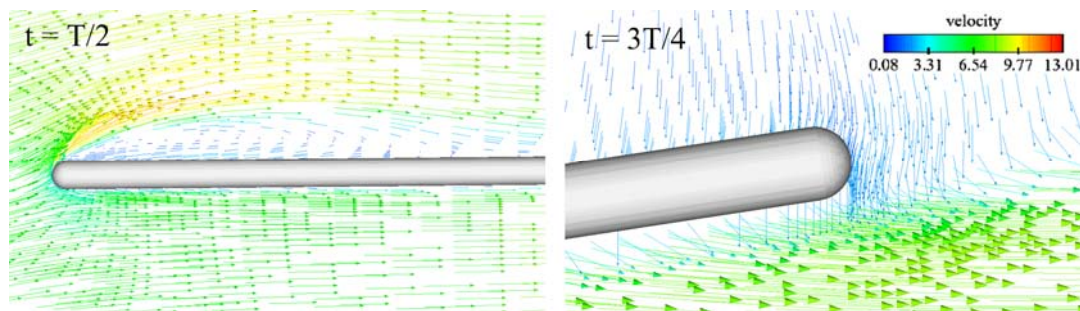


**Figure 3.12 :** a) Velocity vectors at the LE ( $t = T/2$ ) – case A b) Velocity vectors at the TE ( $t = 3T/4$ ) – case A

It is clearly seen that the flow separates from the very beginning of the LE but quickly reattaches around  $1/6$  of the chord length. Indeed, the adverse pressure gradient being modest allows the separated flow to reattach to the surface, thus forming a small and thin separation bubble. It is the turbulent shear stress that causes transport of momentum across the boundary layer, responsible for the closure of the

laminar separation bubble. This recirculation region is characterized by constant pressure values which impact the chordwise  $C_p$  values along the surface. Indeed, the decrease in  $-C_p$  values after the leading edge stagnation point is much smoother such that the lowest value is not reached before 0.5 chord lengths. The flat portion at the beginning indicates the LEV and as we can see it is not larger than 10 % of the chord length. It appears on Figure 3.10 b) that the motion of the flat-plate from the central and maximum angle to the upper and mean angle positions between times  $T/4$  and  $T/2$  is accompanied by a reduction in lift and increase in drag. The wing is in the upstroke part of the motion which induces a negative incidence with respect to the flow, and although the angle induced by the pitching is increasing, this movement leads to a loss in lift. As for the augmentation of drag it can be explained by the formation of the LEV.

From time  $T/2$ , the size of the leading-edge vortex extends along the chord, as we observe on the velocity vectors at time  $3T/4$ . At this point of the cycle the flat-plate is back to the central position and the angle of attack is at its lowest value. Between these two times it is obvious from the pressure distributions that the separation bubble is growing in size as the extent of the flatter portion of the distribution increases. This can be seen as we compare the curves that are plotted for the successive times  $T/2$ ,  $2T/3$  and  $3T/4$  on Figure 3.14. On Figure 3.13 a) we may observe that the LEV has almost entirely covered the upper surface of the flat-plate as the flow reattaches slightly before the trailing-edge. The progressive increase in size of the laminar separation bubble between times  $T/2$  and  $3T/4$  appears to be very beneficial. Indeed, the lift increases as the drag decreases up to their highest and lowest values respectively while the LEV spreads downstream. Obviously, the contribution of an elevated pressure drag for a larger bubble is compensated by a reduced friction drag, due to the larger and stronger recirculation area. Between these two times the wing is in the downstroke part of the motion such that it acquires a certain incidence with respect to the flow in addition to the instantaneous pitching angle. As a result, the strength of the LEV increases with the maximum instantaneous angle of attack. The extension of the LEV is caused by this descending movement of the wing.

At time  $3T/4$  we may consider that the LEV has reached the trailing-edge. This is shown on Figure 3.12 b), illustrating the velocity vectors at the TE, and indicating

that the recirculation region is limited to the very end of the flat-plate. However, after  $3T/4$  the lift suddenly drops as the drag increases. This is related to the pitching up of the flat-plate from its lowest pitching angle. In this simulation it also corresponds to the sudden bursting of the separation bubble as the LEV extends beyond the trailing-edge. Indeed, as the adverse pressure gradient increases we come to a point where the turbulent shear stress is not able to overcome these forces and reattachment of the boundary layer is no longer possible. From this point dynamic stall of the flat-plate is surpassed and leads to a sudden drop in lift and rise in drag. Between  $3T/4$  and the end of the cycle, these aerodynamic coefficients monotonically evolve since the flow on the upper surface remains fully-separated due to the increasing angle of attack caused by the augmentation of the pitching angle combined to the descending motion of the wing. As a result, the bubble further affects the surrounding flow that is more and more slowed down by the wing's presence. This clearly appears as we compare the velocity vectors of Figure 3.13 b) down below taken at time  $5T/6$  with the previous flow field taken at time  $t = 0$  shown on Figure 3.11 a).

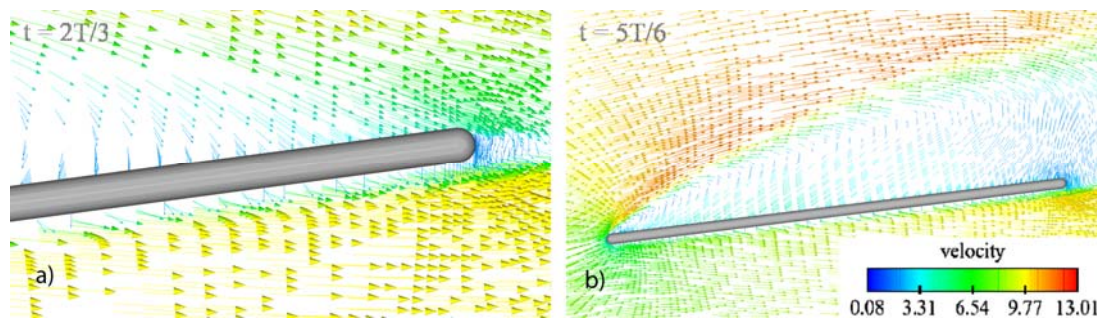


**Figure 3.13 :** a) Velocity vectors at the TE,  $t = 2T/3$  – case A b) Velocity vectors at  $t = 5T/6$  – case A

This is confirmed by the pressure distributions of Figure 3.14. At time  $5T/6$ , the bubble covers the whole plate as we know and the lowest value is not reached before the trailing-edge at the stagnation point. This is also the case at time  $T$ , however the  $C_p$  values are much lower and as these decrease in time until time  $T$ , so does the lift generated. In addition, this low-pressure region created by the large amount of vorticity leads to an increase the drag.

As the cycle starts again, the size of the separation bubble decreases very fast until the flow is fully reattached at  $T/4$ . This progressive reattachment of the boundary layer from the leading-edge is made possible by the ascending motion of the wing as the next upstroke begins at time  $t = 0$ . This portion of the cycle is naturally



accompanied by an important reduction of the drag. We may conclude by saying that the formation of a leading-edge vortex has proved to be very advantageous since while it develops, the lift suddenly increases and the drag drops to reach its lowest value as the LEV covers more and more of the upper surface. Although no detachment of the LEV has been observed, the spreading of the LEV has proved to be very beneficial. This is accompanied by an increasing suction that results in a lift increase. However, once the LEV bursts and the flow becomes fully separated, the performance of the wing suddenly deteriorates.

The flapping parameters imposed in this case have not allowed us to produce any thrust since even at the optimum point of the cycle, the drag remained positive. We will later perform several parameter studies in order to try and obtain a thrust producing case.

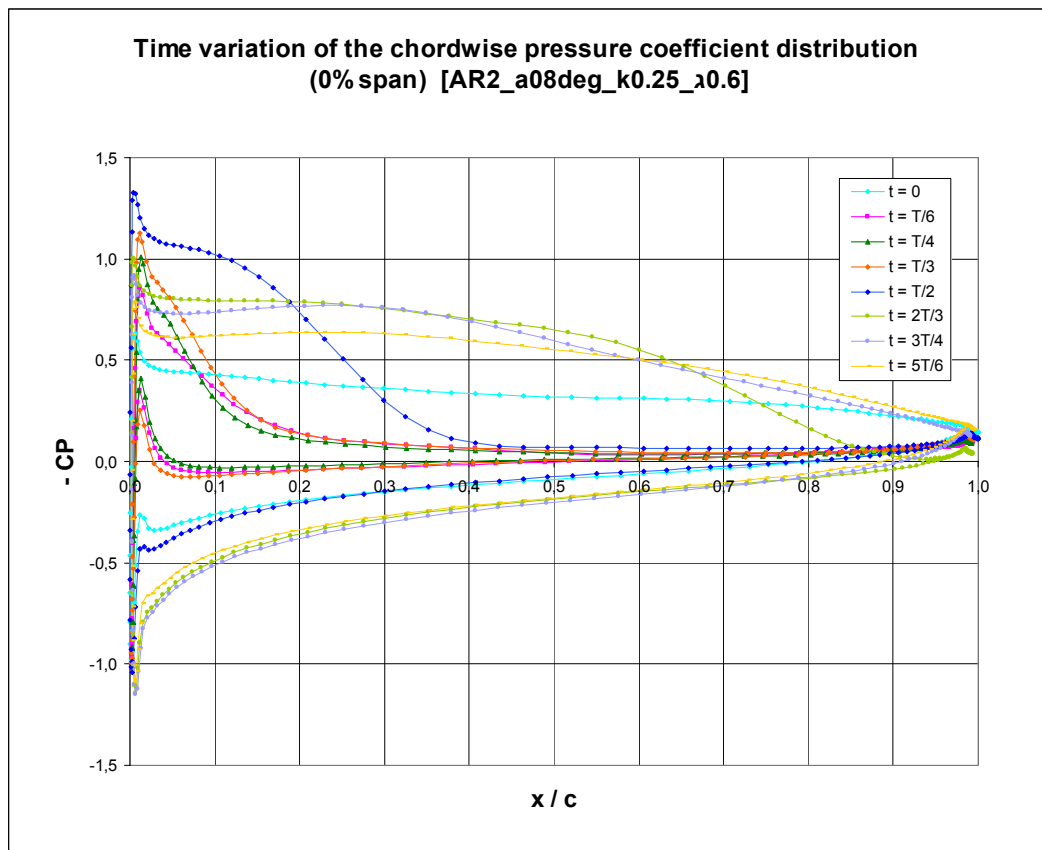


**Figure 3.14 :** Pressure distributions throughout the period ( $-C_p$  values)

### 3.4.2 Tip effects

In this paragraph the three-dimensional effects will be investigated based on the same simulation case. The aim is to highlight the spanwise variations and eventually

relate them to the evolution of the tip vortices that develop. Let us first of present the contours of vorticity magnitude that were obtained in the different planes that were shown on Figure 3.8 b). These are given at four different times during the cycle:  $t = 0, T/4, T/2$  and  $3T/4$  in Appendix B.

We recall that the formation of the wing tip vortex is directly related to the generation of lift. Indeed, as lift is produced the transverse pressure gradients impose an additional three-dimensional component of velocity in the region surrounding the tips. Consequently, a concentration of streamwise vorticity appears. We should note that referring to ‘*streamwise*’ vorticity indicates that the flow rotates around the x axis. Its formation can be observed on the vorticity contours of Appendix B at all times during the cycle as the streamwise vorticity is one of the components of the vorticity vector that contributes to the total vorticity magnitude. In the plane located at a third of the chord length, it is just starting to appear. It is possible to distinguish the ‘*streamwise*’ vorticity induced by the tip vortices which rotates around the x axis, from the ‘*spanwise*’ vorticity related to the boundary layer separation which rotates around the z axis. This is done by plotting these components of vorticity separately. For instance, we have represented them on Figure 3.15 at times  $t = 0$  and  $t = 3T/4$  in the plane positioned at the trailing-edge.

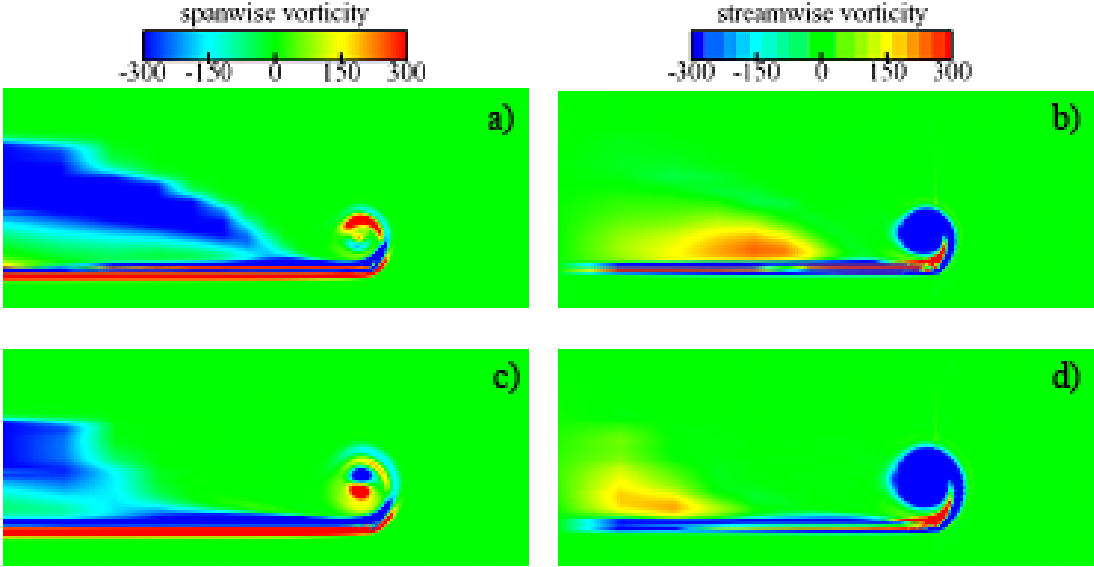


**Figure 3.15 :** Vorticity components in the TE plane a) spanwise vorticity at  $t = 0$  b) streamwise vorticity at  $t = 0$  c) spanwise vorticity at  $t = 3T/4$  b) streamwise vorticity at  $t = 3T/4$

Thanks to these pictures we can now discern the regions of spanwise vorticity from those dominated by streamwise vorticity. As expected, the rotation of the flow at the tip of the flat-plate occurs streamwise because of the strong presence of the tip vortex as shown on pictures b) and d). The boundary layer very close to the surface of the plate, at the trailing-edge, appears to be sucked in towards the tip by the vortex. A small and weaker region exists above the wing indicating the presence of three-dimensional effects. The spanwise contours of pictures a) and c) are representative of the boundary layer separation that takes place in the streamwise direction since it results in a recirculation region. Now that we are able to distinguish between the two vorticity components, it will be easier to comment on the series of pictures of Appendix B, taken for the vorticity magnitude. Indeed, these are particularly useful since the size and effect of the tip vortex on the spanwise vorticity appears on the same image.

As we have just observed on the streamwise contours of Figure 3.15, the vortex is initially fed by the wing boundary layer vorticity. By comparing the contours of vorticity magnitudes in the planes positioned at 33%, 66% of the chord and at the trailing edge, we observe that it grows in size as it progresses downstream. Indeed, the development of the tip vortex is due to the rolling-up of additional shear layer vorticity that causes the spiral to increase as it convects downstream. In the wake of the wing, we can see from the contours in the planes at 0.5, 1 and 2 chord lengths from the trailing-edge that as the vortex continues to grow the spirals smooth together under the action of turbulent and viscous diffusion. Eventually, the vortex is diffused and decays as time passes and the downstream distance lengthens. We have found that the vortex starts dissipating right after the rolling-up and merging of the layers is complete. The time and length during which the vortex is quasi steady and homogeneous is very limited. This may be related to the grid that was used to resolve the flow since we recall that to limit its size the meshes in the wake of the flat-plate had to rapidly increase in size. This resulted in a relatively coarse mesh in the downstream direction which is most probably accelerating the diffusion of the vortices. In our case, we observe that already at four chord lengths from the trailing-edge the vortices have considerably weakened in concentration as the vorticity levels are much lower. We suppose that a few chord lengths later these will have totally dissipated and disappeared.

We may now make a few comments on the evolution of the tip vortex throughout the cycle. Obviously its size and circulation depend greatly on the motion of the flat-plate at all times. It appears from the vorticity contours of Appendix B that the vortex is larger and more disorganized at  $t = 0$  and  $3T/4$ . Between these two times the flat-plate is descending and pitching up. This agitated behavior is a result of the fully-separated turbulent boundary layer present on the upper side of the wing during this portion of the motion related to the bursting of the LEV beyond the trailing-edge as discussed previously. We could observe on Figure 3.9 that the vortex trajectory in the chordwise direction experienced some spatial excursions caused by the flat-plate's oscillations, although rather limited due to the low reduced frequency. As opposed to these movements in the transverse direction, we see from these contours that the spanwise location of the vortex centre remains almost stationary as it evolves downstream. Four planes have been positioned in the symmetry plane, at 50% and 75% of the span and at the flat-plate's tip.

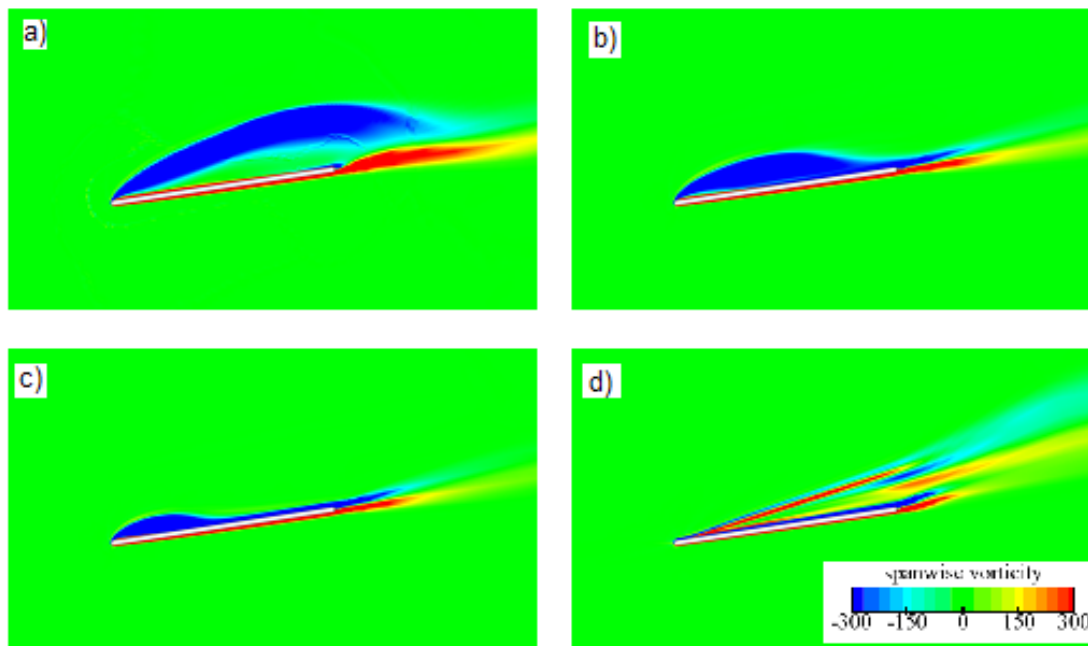


**Figure 3.16** : Spanwise vorticity contours at  $t = 3T/4$  – case A a) symmetry plane b) plane at 50% span c) plane at 75% span d) tip plane

The aim is now to better understand the effect that the tip vortices have on the flow structure and on the aerodynamic performance of the wing. The spanwise vorticity contours are represented on Figure 3.16. The rotational movement is therefore related to the behavior of the flat-plate's boundary layer. It appeared that for  $t = 0$  and  $3T/4$  at which the flow was shown to be fully-separated in the symmetry plane, it

progressively reattaches from the trailing-edge as we move towards the tip. The size of the LEV in being reduced and we see on picture d) that it has totally disappeared in the tip plane.

As we observe the corresponding pressure distributions on Figure 3.17, the reattachments are clearly visible since the flatter portion of the curve shortens as the  $-C_p$  values decrease to reach the trailing-edge value much sooner along the chord. At the '100% span' plane at the tip the curve shift upwards as the  $-C_p$  values considerably increase, indicating the presence of the tip vortex.

From these observations, we deduce that the effect of the tip is to limit the strength and growth of the laminar separation bubble nearest it, as the tip vortex energizes the flow and reduces the size of the laminar separation bubble.

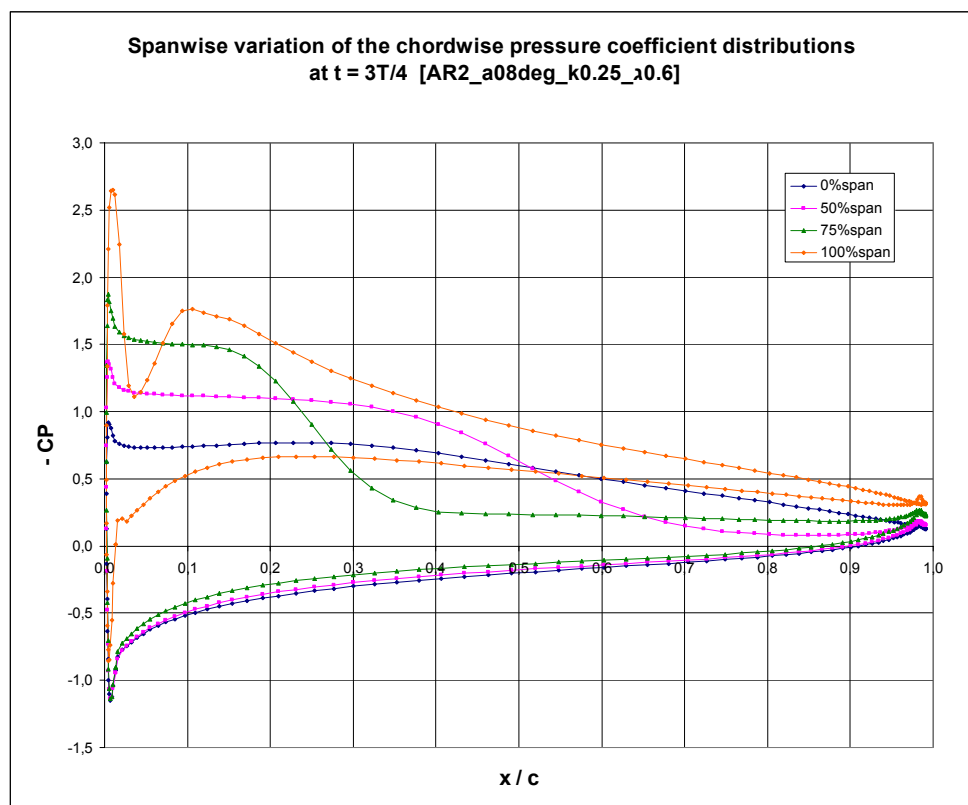


**Figure 3.17 :** Evolution of the pressure distributions spanwise at  $t = 3T/4$  – case A

These observations highlight the positive impact that the tip vortex may have on the flow. Indeed, in these first few observations related to the three-dimensional effects that develop, we have seen that the tip vortex helps to control the spreading of the LEV by limiting its extension to the downstream. Its effect increases progressively from the symmetry plane towards the tip, while the amount of separation reduced

with the growth rate of the LEV. This leads to a reduction of the pressure drag. However, we are not yet able to conclude on the overall contribution of the tip vortex as it also has negative aspects. Indeed, the induced drag will be considerably increased which might deteriorate the global aerodynamic performance of the wing by inducing energy losses. In addition, it might also impact on the lift distribution by causing sharp gradients towards the tips that cause the flow field to present significant hysteresis during a cycle of oscillation. By performing parametric studies, we will further investigate these three-dimensional effects and try to answer these questions.

### 3.5 Parameter Study

#### 3.5.1 Effect of the aspect-ratio

Considering that MAVs are to maneuver and move in unsteady environments combined to the requirements in terms of lift for the weight of the structure to be balanced, their aspect ratio (AR) are usually smaller than 2. The aim in this paragraph is to compare the results obtained for two different AR values of 1 and 2. The simulation parameters remain the same, only the AR is changed. These are fixed to the following values:

- Mean angle of attack →  $\alpha_0 = 8^\circ$
- Reduced frequency →  $k = 0.25$
- Amplitude ratio →  $\lambda = 0.6$

Let us first of all compare the behavior of the lift and drag coefficients throughout the cycle represented on Figure 3.18 below.

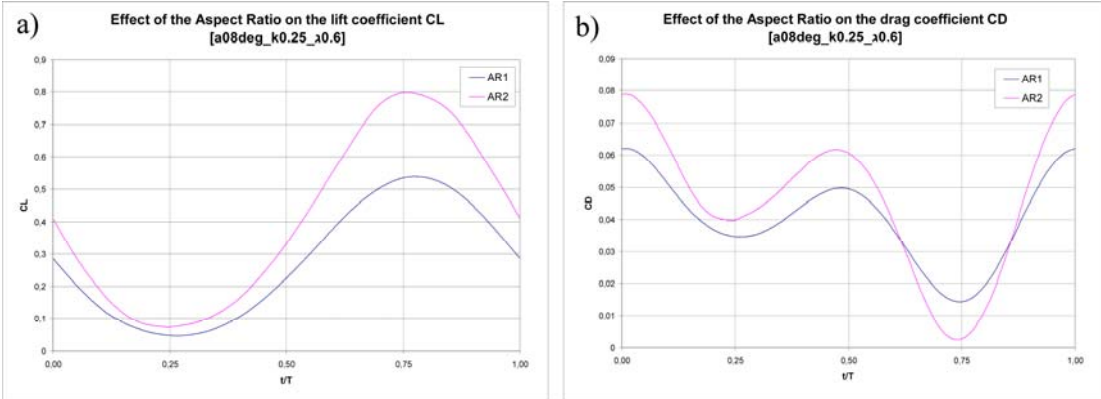


**Figure 3.18 :** Evolution of the lift and drag coefficients according to the aspect ratio – case A & B a) CL Vs. time b) CD Vs. time.

On image a) it appears that the lift curve obtained for an AR of 1 shifts down with respect to the values obtained when the AR is equal to 2. As for the drag produced plotted on image b) it is less throughout most of the cycle for a value of 1. To explain why the aerodynamic coefficients behave in such a way, let us first of all refer to the vorticity magnitude contours that highlight the effect of the tip vortex. These are represented in the plane positioned at the trailing-edge of the flat-plate for time  $t = 3T/4$ . As we compare pictures a) and b) of Figure 3.19, we observe that the size and strength of the core of the tip vortex is not affected by the aspect ratio. However, its influence on the wing surface increases as the AR reduces. Indeed, the portion of the span under the direct influence of the vortex is larger and therefore the lift generated decreases. However a smaller AR appears to be advantageous in terms of drag. Indeed, the tip vortex as mentioned previously tends to reduce the growth of the LEV, thus delaying the bursting of the laminar separation bubble. Its effect on the chordwise flow field diminishes as we get further from the tip. Thus, as the span reduces its influence is stronger. This is confirmed by the spanwise vorticity contours represented on Figure 3.20 at the same time  $3T/4$  in the plane located at 50% of the span.

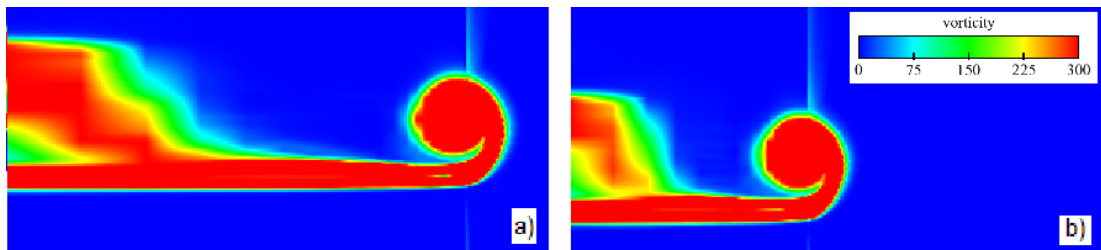


**Figure 3.19 :** Vorticity contours in the TE plane at  $t = 3T/4$  a) AR = 2 – case A b) AR = 1 – case B

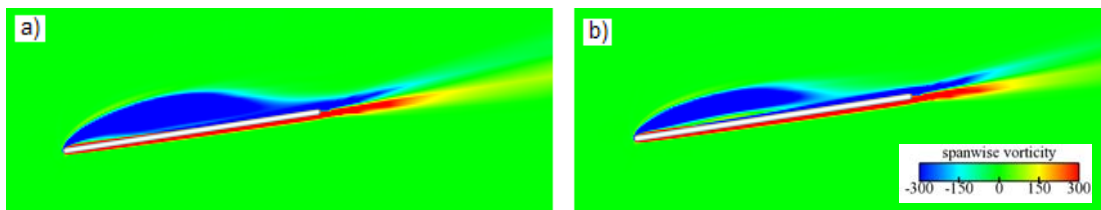


**Figure 3.20 :** Vorticity contours in the plane at 50% span at  $t = 3T/4$  a) AR = 2 – case A b) AR = 1 – case B

For an AR of 1 represented on Figure 3.20 b), we see that although the distance from the tip is less since the plane is positioned relative to the span of the wing, the LEV is smaller compared to Figure 3.20 a) where the AR equals 2. This continues to be the

case up to the symmetry plane as illustrated on the velocity vector fields of Figure 3.21 at  $t = 3T/4$ .

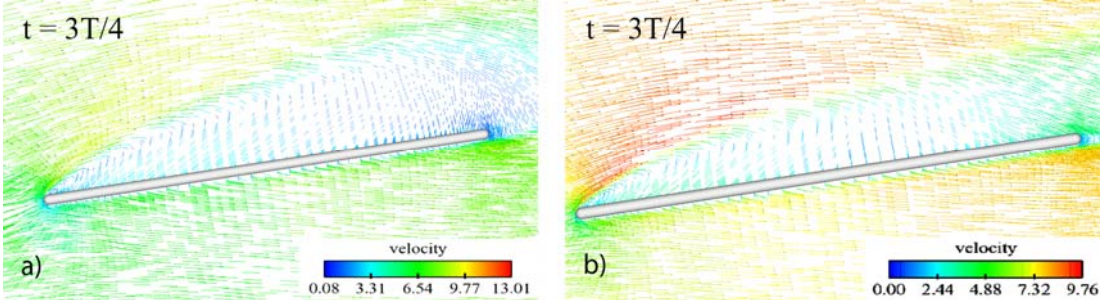


**Figure 3.21** : Velocity vectors in symmetry plane at  $t = 3T/4$  a)  $AR = 2$  – case A b)  $AR = 1$  – case B

By comparing pictures a) and b), it clearly appears that the tip vortex affects the flow up to the symmetry plane. Indeed, in both cases the flow is separated over the entire flat-plate but the size of the separation region for an AR of 1 has been further reduced by the tip vortex. These observations were based on a single time during the cycle. To complete this study let us compare the chordwise pressure distributions between the two AR at several times throughout the cycle in order to generalize our previous comments. The  $-C_p$  curves are represented on Figure 3.22 further below.

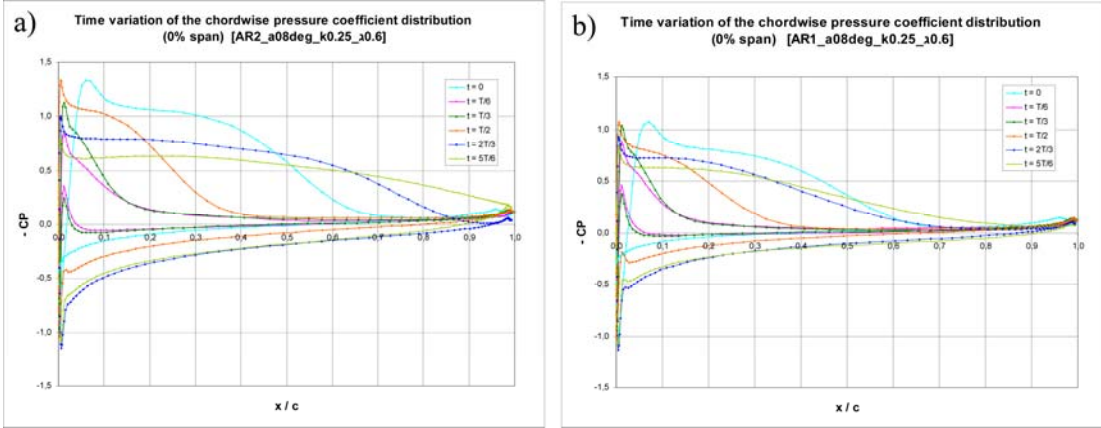


**Figure 3.22** : Effect of the AR on the pressure distributions in the symmetry plane a)  $AR = 2$  – case A b)  $AR = 1$  – case B

These are confirmed since they hold whatever the moment in the cycle. Indeed, as we compare the curves at a given time, the AR of 1 will always present lower values and shorter laminar separation bubbles. This explains the behavior of the drag coefficient for which a lower AR reduces its fluctuation amplitudes. As a result, for an AR of 1, the  $C_D$  values are generally lower throughout the majority of the period.



Now that the effect of the AR has been investigated we may present the thrust coefficients that were obtained for the two AR under consideration. Table 3.3 gives their values along with the power input coefficients.

**Table 3.3:** Effect of the AR on the thrust and power input coefficients

AR	$C_T$	$C_{P\_IN}$
1	-0,03983	0,038
2	-0,04515	0,055

As expected, the reduction in drag that has been observed for a smaller AR leads to an improvement in terms of thrust. Of course, we cannot really speak of thrust since its value is negative in correspondence to a drag-producing case. However, there is a slight improvement since it increases from approximately -0.045 to - 0.04 which corresponds to 11% reduction. We cannot speak of propulsive efficiency in any of cases A and B since they are both drag-producing cases. However we do notice that the power input coefficient representing the work necessary to impose the flapping motion is much higher since the aspect ratio doubles, with a 45% increase when AR goes from 1 to 2.

We may conclude by saying that this study has proved that the tip effect is highly dependent on the wing aspect ratio. Under the present conditions, it appears to be more advantageous to have a lower aspect ratio due to the positive effect of the tip vortex on the flow-field. These results may question the negative effect of the tip vortices and their possible role on the force production capability. However this cannot be generalized as we know that the tip vortex is often accompanied by important energy losses that can result in the deterioration of the efficiency of a flapping wing mechanism.

### 3.5.2 Effect of the mean angle of attack

In this study, the aim is to investigate the effect that the mean angle of attack has on the flow structure and the performance parameters. We will be comparing the reference simulation, case A, for which the mean incidence between the incoming flow and the flat-plate was fixed to 8 degrees, with a lower value of 4 degrees, implemented in case C. In correspondence to the future experimental studies, the

aspect ratio is fixed to 2 for all simulations, and the other parameters are kept constant:

- Aspect ratio* →  $AR = 2$
- Reduced frequency* →  $k = 0.25$
- Amplitude ratio* →  $\lambda = 0.6$

On Figure 3.23 the aerodynamic coefficients are given. As we can see, reducing the mean flow angle from 8 to 4 degrees shifts the lift and drag curves downwards.

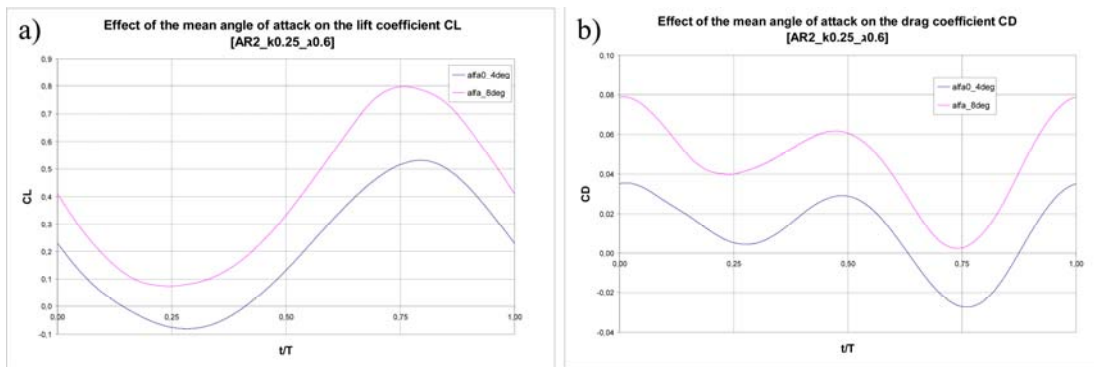


**Figure 3.23 :** Evolution of the lift and drag coefficients according to the mean flow angle – case A & C a) CL Vs. time b) CD Vs. time.

In order to understand why this loss in lift and reduction of the drag force occur, we first refer to the spanwise vorticity contours of Figure 3.24. We compare the two sets of images at  $t = 0$  in the four different spanwise locations. Put side by side it is obvious that the simulation with  $\alpha_0$  equal to 4 degrees generates much less vorticity. We may deduce that the boundary layer is lightly to separate much less easily. This also appeared to be the case at times  $T/4$ ,  $T/2$  and  $3T/4$  although we have not included those results to the report and we deduce that this remains the case throughout the entire period. The same observations can be made as we compare on Figure 3.25 the contours of vorticity magnitude in the spanwise direction this time. On these, time  $t = 3T/4$  is considered. The tip vortex at 4 degrees is smaller in size since less streamwise vorticity is present in the tip region.

We recall that at this moment of the motion the flat-plate is descending and for 8 degrees the LEV had reached the trailing-edge. This is not yet the case for 4 degrees since the size of the laminar separation bubble has been reduced as we will now illustrate.

We recall that the formation of the LEV starts at time  $T/4$  when the wing is going up and begins pitching down. It is after it reaches its highest position at time  $T/2$ , as the downstroke part of the motion begins, that the LEV starts spreading downstream.

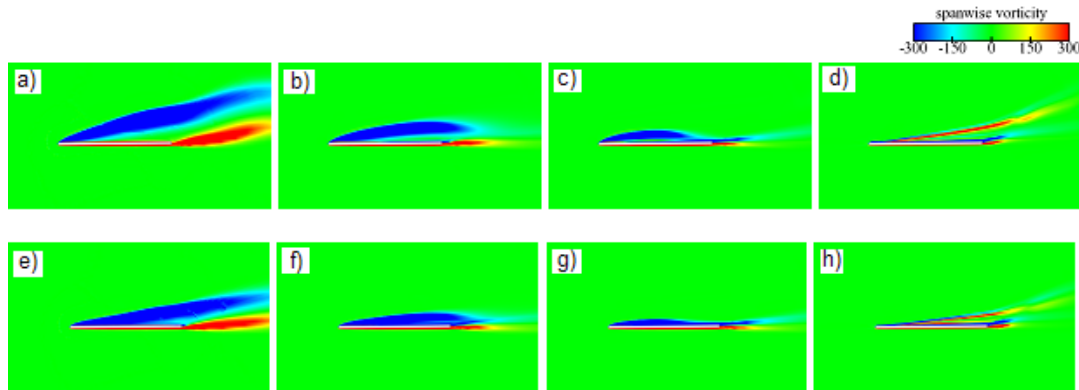


**Figure 3.24 :** Vorticity contours in the chordwise direction at  $t = 0$  a) Sym. plane,  $8^\circ$  - case A b) 50% span plane,  $8^\circ$  - case A c) 75% span plane,  $8^\circ$  - case A d) Tip plane,  $8^\circ$  - case A e) Sym. plane,  $4^\circ$  - case C b) 50% span plane,  $4^\circ$  - case C c) 75% span plane,  $4^\circ$  - case C d) Tip plane,  $4^\circ$  - case C

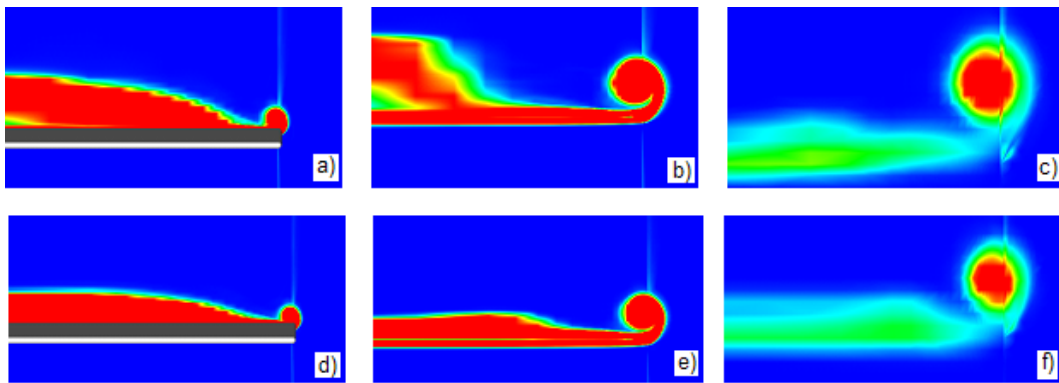


**Figure 3.25 :** Vorticity contours in the spanwise direction at  $t = 3T/4$  a) 33% chord plane,  $8^\circ$  - case A b) TE plane,  $8^\circ$  - case A c) 1 chord after TE plane,  $8^\circ$  - case A d) 33% chord plane,  $4^\circ$  - case C b) TE plane,  $4^\circ$  - case C c) 1 chord after TE plane,  $4^\circ$  - case C

On Figure 3.26 we have represented the velocity vector field at this moment, in the symmetry plane for both mean flow angles.

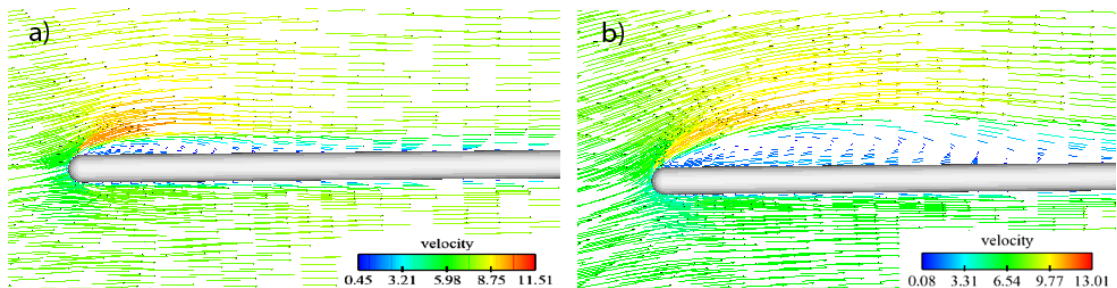


**Figure 3.26 :** Velocity vectors at  $t = T/2$  a)  $\alpha_0 = 4^\circ$  - case C b)  $\alpha_0 = 8^\circ$  - case A

By comparing the two pictures it is obvious that the LEV is considerably smaller for  $\alpha_0$  equal to 4 degrees which confirms our previous remarks based on the streamwise vorticity levels. We may conclude that it is the reduction in size of the laminar separation bubble, which reduces the suction induced by the pressure difference between the upper and lower surfaces that leads to the lift loss observed. The drag curve shifts downwards since both the pressure drag, due to less boundary layer separation, and the induced drag, caused by smaller tip vortices, are reduced.

Figure 3.27 representing the chordwise pressure distributions plotted at various times during the oscillation confirms that at any moment the separation distance from the leading-edge is reduced as  $\alpha_0$  decreases since the flatter portion of the curves is shorter as the  $-C_p$  values for all of them starts decreasing sooner along the chord length.

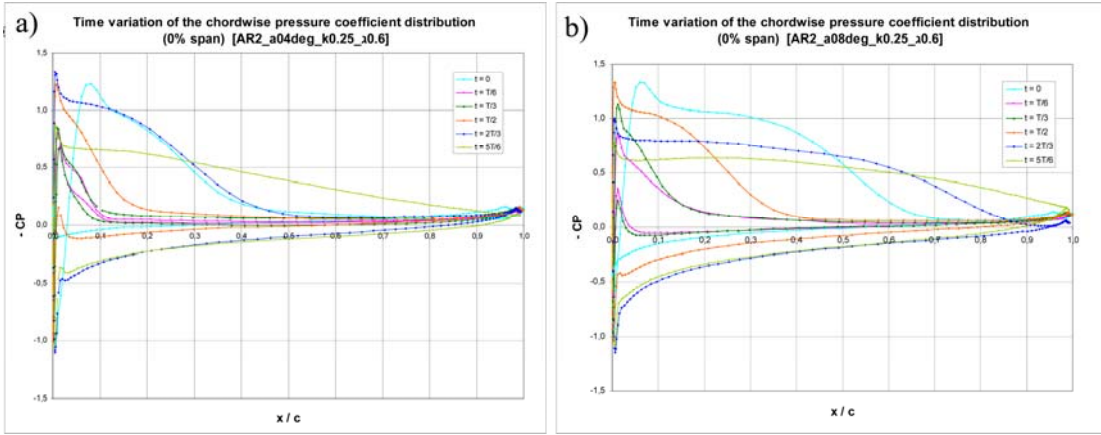


**Figure 3.27 :** Effect of the mean flow angle on the pressure distributions in the symmetry plane a)  $\alpha_0 = 4^\circ$  - case C b)  $\alpha_0 = 8^\circ$  - case A

The effect of the mean flow angle on the performance parameters is finally inspected. The thrust and power input coefficients are given in Table 3.4. Due to the reduction in drag accompanied by the lower mean flow angle, the thrust coefficient is improved although its overall value remains negative and thus the simulation case C still results in a drag-producing system. The value goes from -0.045 to -0.01 for 8 and 4 degrees respectively corresponding to a 78% drag reduction. Because of the mean angle reduction and the reduction of the lift available, the power input necessary to impose the motion increases by 20%.

**Table 3.4:** Effect of the mean flow angle on the thrust and power input coefficients

$\alpha_0$ (degrees)	$C_T$	$C_{P\_IN}$
4	-0,010	0,044
8	-0,045	0,055

We may conclude by saying that a lower mean flow angle compared to 8 degrees has shown to be much more advantageous since the thrust coefficient is improved. This is related to the fact that an incidence of 8 degrees, especially for a flat-plate geometry that tends to easily separate, is certainly too high and results in an excessive amount of separation at various moments of the cycle. This is actually visible on Figure 3.23 since the difference in time between the two  $C_L$  and the two  $C_D$  curves does not evolve linearly. This proves that at 8 degrees the aerodynamic performance of the flat-plate has already started to deteriorate because of excessive viscous effects, as the LEV and induced separations become dominant. A value of 4 degrees has shown to be more appropriate as it reduces the large separation that led to important drag. Although the drag curve has moved downwards and that for a short time towards the end of the spreading of the LEV downstream, negative values were obtained, this was not sufficient to yield into a thrust producing wing. Indeed, the creation of thrust instead of drag during the portion of the curve below zero was not long enough. In addition, further simulations are necessary to determine the optimum mean flow angle as it might be lower than 4 degrees. There is also a possibility that this value appears to be within 4 and 8 degrees since the excessive separation caused by the flat-plate geometry at 8 degrees might be eliminated before reaching 4 degrees such that the advantages of inducing incidence to the motion start emerging.

### 3.5.3 Effect of the amplitude ratio

The objective in this paragraph is to discuss about the influence that the amplitude ratio has on the results. We recall that this parameter measures the ratio between the pitch and plunge amplitudes. However, to make it non-dimensional it incorporates the reduced frequency and is defined as:  $\lambda = \alpha_1 / (2kh)$ . In this study three different amplitude ratios will be compared for values equal to 0.4, 0.6 and 0.75 while all the other parameters are kept constant and correspond to the following:

**Table 3.5:** Pitch amplitudes related to each amplitude ratio

Aspect ratio  $\rightarrow AR = 2$   
 Mean angle of attack  $\rightarrow \alpha_0 = 8^\circ$   
 Reduced frequency  $\rightarrow k = 0.25$

	Amplitude ratio	Pitch amplitude: $\alpha_1$ (°)
Case D	0,4	5,7
Case A	0,6	8,6
Case E	0,75	10,7

To modify the amplitude ratio we decide to only change one parameter while the others are fixed. Thus, the non-dimensional plunge amplitude  $h$  does not change and remains equal to 0.5 such that it is the pitching amplitude  $\alpha_1$  that is modified. The values are summarized in Table 3.5 above.

The evolution of the lift and drag coefficients are shown on Figure 3.28. On one hand, the trend observed for the lift force is common to all  $\lambda$  values but as it increases the maximum amplitudes observed decrease which yields into generating less lift across the cycle. This is due to the increasing pitching amplitude that causes stronger flow separation, resulting in a diminished lift level. On the other hand, the trend observed for the drag coefficient is modified by the various values of  $\lambda$ . Between 0.4 and 0.6 for instance, the drag is reduced in some portions of the oscillation while it increases in other parts. During the upstroke from time  $t = 0$  to  $T/2$ ,  $C_D$  is much less whereas during the downstroke it is increased.

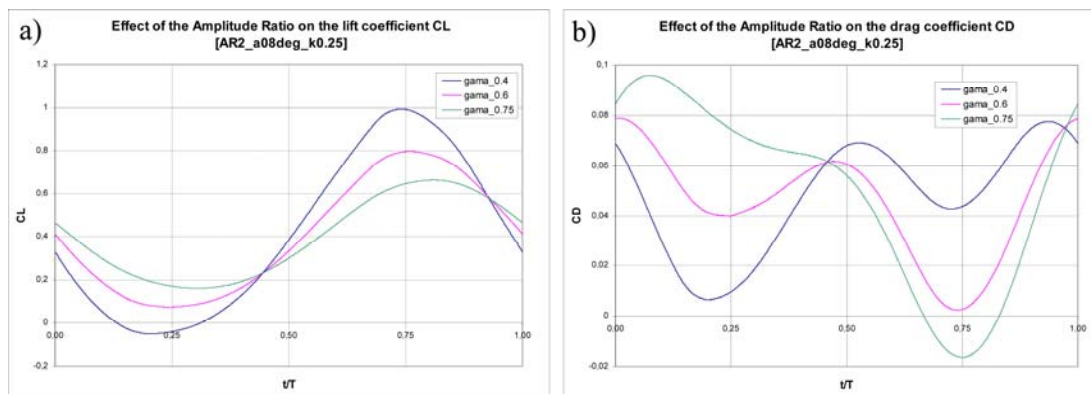


**Figure 3.28 :** Evolution of the lift and drag coefficients according to the amplitude ratio – case D, E & A a) CL Vs. time b) CD Vs. time.

As for the difference between 0.6 and 0.75 it is the opposite, drag is higher during the first half of the period and lower in the second. We will later consider the overall effect of the amplitude ratio on the thrust coefficient but let us first of all try and understand the drag behavior by comparing the results obtained.

During the first quarter of the cycle, the reattachment seems to occur much faster for lower values of  $\lambda$ , as the drop experienced by the drag force is considerably steeper. We recall that reattachment is made possible by the ascending motion of the wing that reduces the effect of the pitching up and allows the boundary layer to reattach. If in addition the pitching amplitude is reduced this has a very desirable effect on this phase of the oscillation as it facilitates reattachment since the pressure difference between upper and lower surfaces is less. Indeed, as we compare the pressure distributions on Figure 3.32 a), b) and c) at the intermediate time  $T/6$ , we observe that the pressure difference decreases with the amplitude ratio, thus generating less drag. As  $\lambda$  is increased from 0.6 to 0.75, the drag does not decrease monotonically but first rises and then drops down to a much higher value than for the other two cases at the same time  $T/4$ . We deduce that reattachment of the boundary layer is not as straightforward due to the higher pitching rate. Although the flat-plate is ascending, the rate at which it plunges needs to progressively increase to counter the faster rotational movement of the wing upwards. This is achieved at the middle of the first quarter cycle and initiates the reattachment accompanied by the reduction in drag.

In order to investigate the effect of the amplitude ratio on the formation of the tip vortex, we have plotted the streamwise vorticity contours in the trailing-edge plane for all three cases. These are compared on Figure 3.29 at time  $t = 0$ .

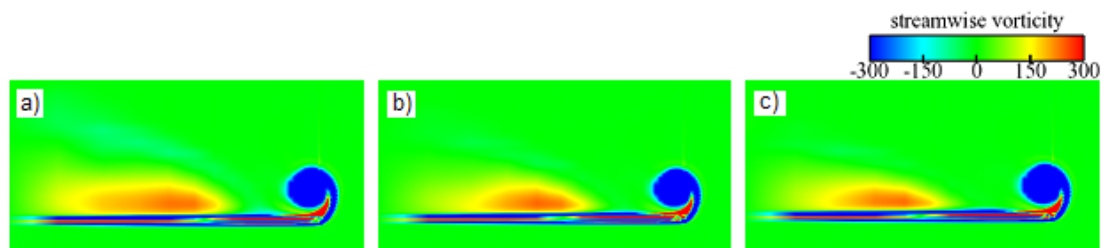


**Figure 3.29** : Streamwise vorticity contours at  $t = 0$  in the TE plane a)  $\lambda = 0.4$  – case D b)  $\lambda = 0.6$  – case A c)  $\lambda = 0.75$  – case E.

We observe that the strength and size of the vortex does not vary with  $\lambda$  and we conclude that the changes obtained between cases A, D and E are not related to the three-dimension effects.

At the contrary, in the second quarter of the cycle, the reduction of the amplitude ratio has a negative effect. We recall that this phase corresponds to the formation of the LEV for which the drag increases at a much faster rate when  $\lambda$  equals 0.4 compared to 0.6. The  $-C_p$  values at the intermediate time  $T/3$  indicate that the

development of the LEV is not as advanced for a value of 0.4. Indeed, the increase in amplitude ratio from 0.6 to 0.75 confirms this remark since we observe that at the same time the pressure differences are more important at 0.75 since they extend to a larger portion of the wing, characteristic of a larger separation. For this value, the drag coefficient actually continues to decrease directly after the reattachment phase and therefore drops instead of rising between times  $T/4$  and  $T/2$ . The pitching down movement seems to be fast enough to counter the production of drag related to the formation of the LEV. The growth of the LEV is faster as observed on Figure 3.30 that illustrates its size at time  $T/2$  for all three amplitude ratio values. This is confirmed by the pressure distributions of Figure 3.32 taken at the same time since the flatter portion of the graphs enlarges as the reattachment takes place further down along the chord length.

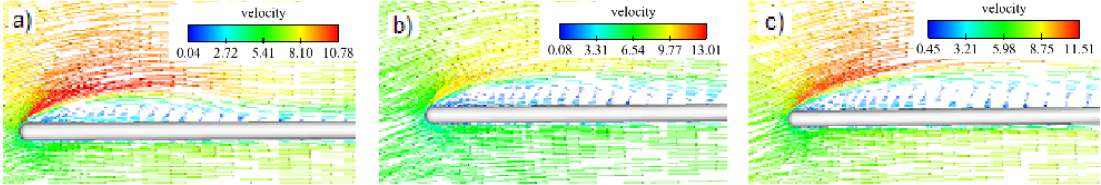


**Figure 3.30 :** Velocity vector flow fields in the LE region of the symmetry plane at  $t = T/2$  a)  $\lambda = 0.4$  – case D b)  $\lambda = 0.6$  – case A c)  $\lambda = 0.75$  – case E.

Throughout the third quarter of the oscillation during which the drag reduces as the LEV extends, a higher amplitude ratio is very advantageous as the drop in drag gets steeper due to the faster pitching down of the flat-plate. In the final phase of the oscillation between times  $3T/4$  and  $T$ , the pitching up of the wing continues to increase the separation and leads to excessive amounts causing all three  $C_D$  curves of Figure 3.28 b) to increase. The flow at time  $3T/4$  is fully separated in all cases as illustrated on Figure 3.31 where the velocity vector flow fields are plotted in the symmetry plane. These indicate, in agreement with the higher drag coefficients observed for decreasing  $\lambda$  values that separation gets more important.

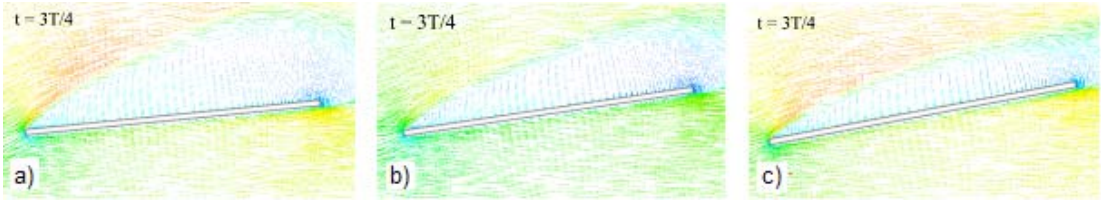


**Figure 3.31 :** Velocity vector flow fields in the symmetry plane at  $t = 3T/4$  a)  $\lambda = 0.4$  – case D b)  $\lambda = 0.6$  – case A c)  $\lambda = 0.75$  – case E.



However, as the amplitude ratio decreases, the rate of drag increase is less for  $t$  within  $3T/4$  and  $T$  since the lower pitching amplitude results in less incidence and lower pitching rates at a given time. For instance, we observe that a value of  $\lambda$  equal to 0.4 allows the reattachment to start sooner since the drag begins to decrease towards the middle of this last time interval.

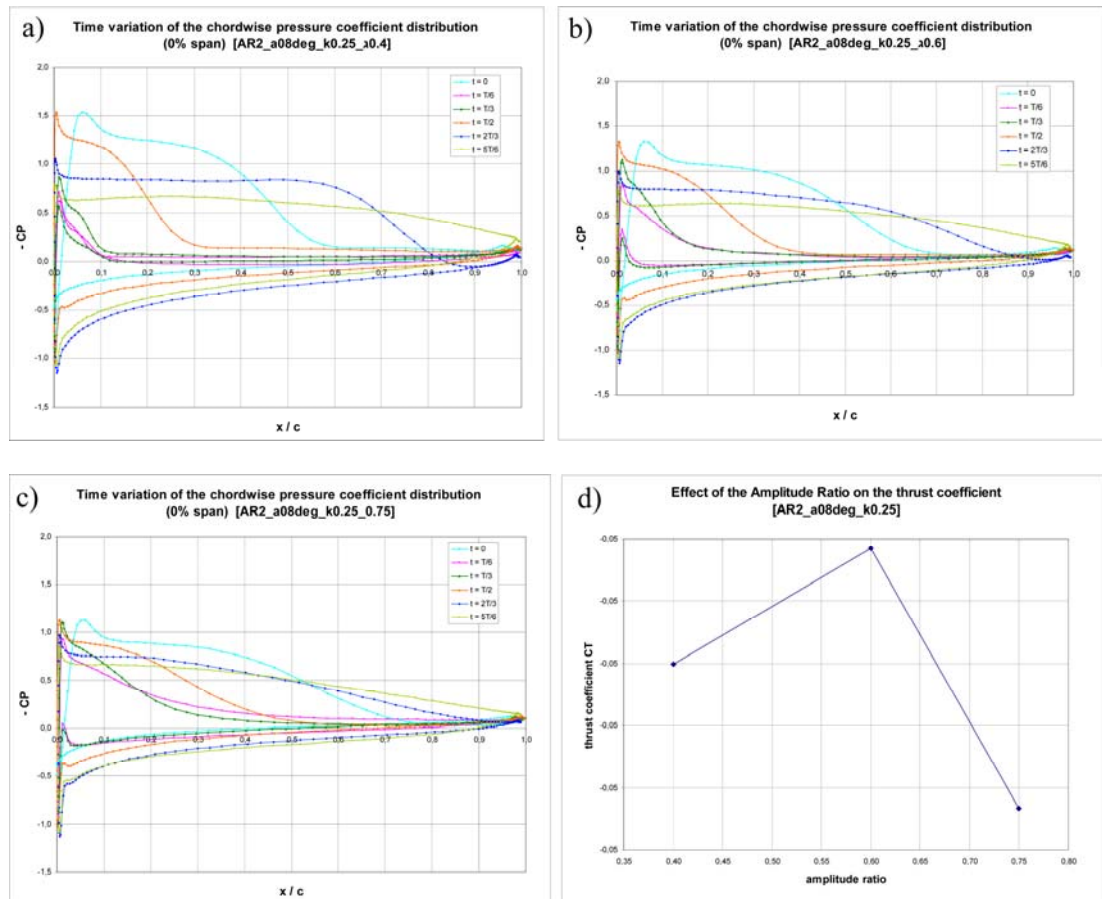


**Figure 3.32 :** a)  $-C_p$  values in sym. plane,  $\lambda = 0.4$  – case D b)  $-C_p$  values in sym. plane,  $\lambda = 0.6$  – case A c)  $-C_p$  values in sym. plane,  $\lambda = 0.75$  – case E d) Effect of the amplitude ratio on the thrust coefficient.

The global effect of these drag fluctuations on the thrust coefficient is plotted on Figure 3.32 d) as a function of the amplitude ratio. In any case the simulations all result in a drag-producing system however under these conditions there appears to be an optimum value, allowing the drag to be minimized.

**Table 3.6:** Effect of the amplitude ratio on the thrust and power input coefficients

gama $\lambda$	CT	CP_IN
0,40	-0,04701	0,069
0,60	-0,04515	0,055
0,75	-0,04933	0,045

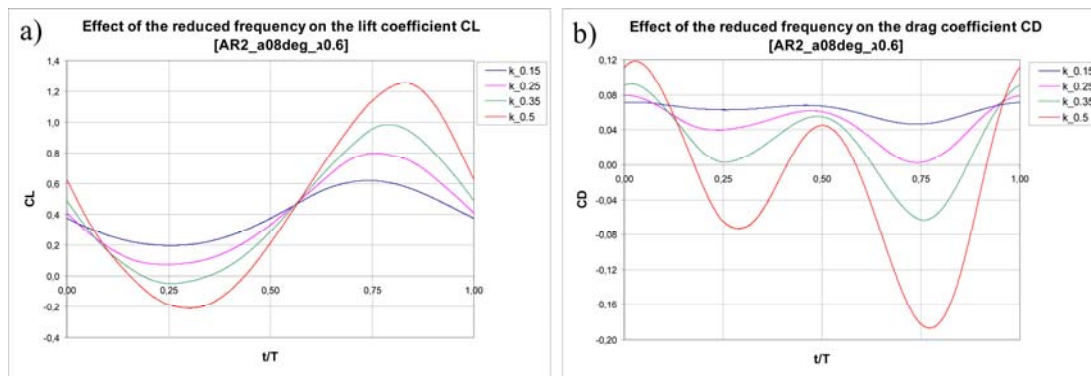
Indeed, the best of the three values in terms of thrust appears to be 0.6 as shown in Table 3.6 above. To precisely determine an optimum value, further calculations are needed. In terms of power input necessary to support the motion, it logically reduces as the pitching amplitude increases.

### 3.5.4 Effect of the reduced frequency

The last parameter study that was performed focused on the effect that the reduced frequency has on the results. Four different values were compared corresponding to 0.15, 0.25, 0.35 and 0.5, while all the other parameters were fixed to the following values:

$$\begin{aligned} \text{Aspect ratio} &\quad \rightarrow \quad AR = 2 \\ \text{Mean angle of attack} &\quad \rightarrow \quad \alpha_0 = 8^\circ \\ \text{Amplitude ratio} &\quad \rightarrow \quad \lambda = 0.6 \end{aligned}$$

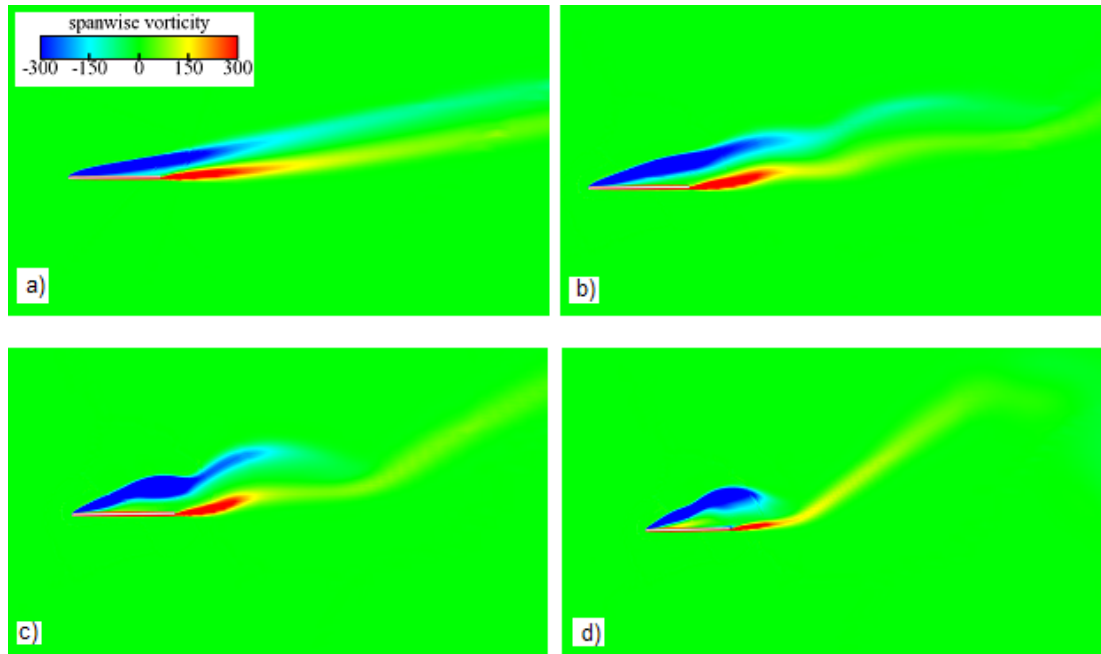
We note that the pitching amplitude also had to be modified since it is the non-dimensional ratio of the pitching and plunging amplitudes that we wish to maintain constant. We start by observing the effect that the parameter has on the lift and drag coefficients from Figure 3.33.



**Figure 3.33 :** Evolution of the lift and drag coefficients according to the reduced frequency – case F, G, H & A a) CL Vs. time b) CD Vs. time.

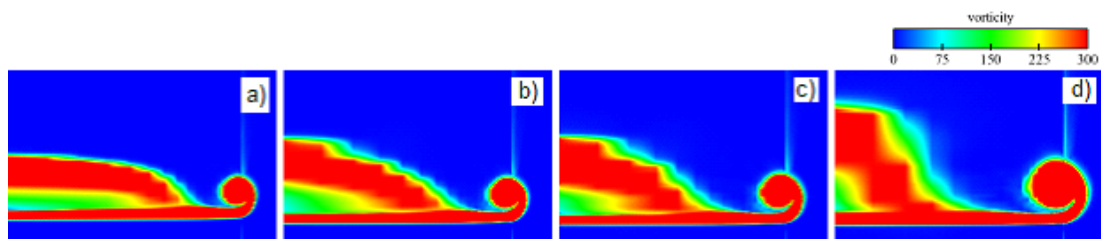
As we can see, the lift force generated increases with  $k$  all through the cycle due to the increased pitching amplitude, whereas the drag penalty considerably decreases. It is clearly much more advantageous to oscillate the wing at a faster frequency but let us now try and understand the reasons of this improvement in performance. On Figure 3.34 are represented the spanwise vorticity contours that were taken in the symmetry plane at time  $t = 0$ . These indicated that the vortical wake is highly dependent on the reduced frequency. As discussed previously, the wake does not

exhibit any distinctive Von Karman street pattern however the vorticity pattern just downstream of the wing shoes that the vertical deflections increase with  $k$  as the wavelengths of the oscillations get smaller.



**Figure 3.34 :** Vorticity contours in the symmetry plane at  $t = 0$  a)  $k = 0.15$  – case F  
 b)  $k = 0.25$  – case A c)  $k = 0.35$  – case G d)  $k = 0.5$  – case H

We may conclude that the unsteadiness present in the flow is progressively increasing as  $k$  varies from 0.15 to 0.5.



**Figure 3.35 :** Contours of vorticity magnitude in the TE plane at  $t = 0$  a)  $k = 0.15$  – case F  
 b)  $k = 0.25$  – case A c)  $k = 0.35$  – case G d)  $k = 0.5$  – case H.

Let us now inspect the contours of vorticity magnitude in the spanwise direction in order to highlight the effect of the reduced frequency on the tip vortex. The pictures of Figure 3.35 are taken in the plane positioned at the trailing-edge of the flat-plate at time  $t = 0$  for which the flow is fully-separated in the symmetry plane whatever the reduced frequency. Considering that the main contribution to the vorticity magnitude in the symmetry plane is the spanwise vorticity related to the boundary layer separation, these pictures suggest that the amount of separation at that time in the

symmetry plane increases with the reduced frequency which is confirmed by the velocity vector flow fields represented on Figure 3.36 down below.

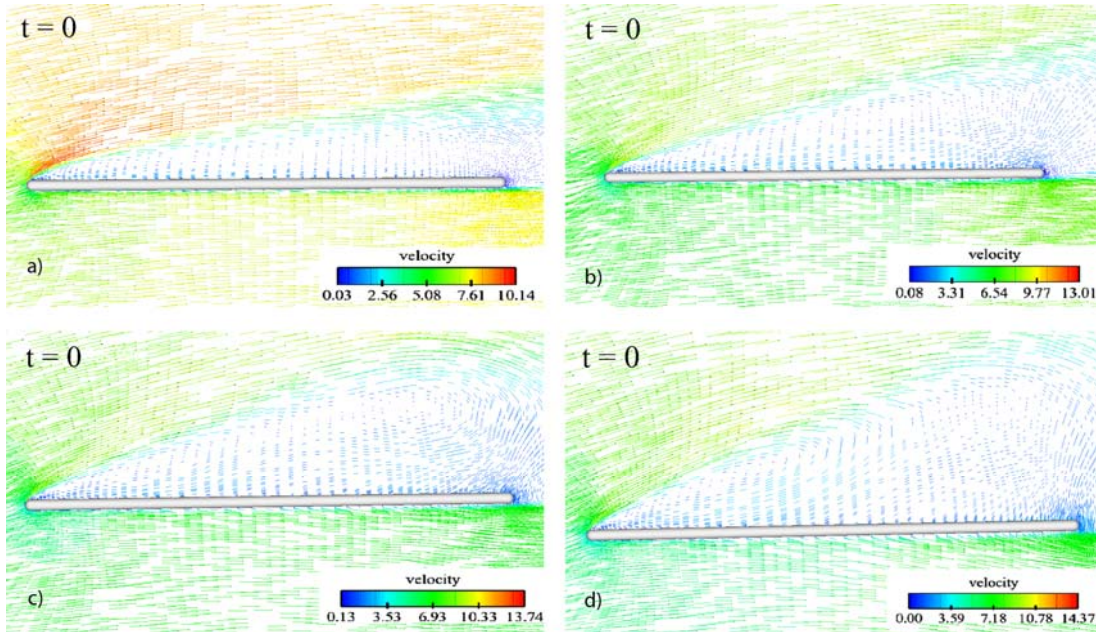


**Figure 3.36 :** Velocity vector flow fields in the symmetry plane at  $t = 0$  a)  $k = 0.15$  – case F b)  $k = 0.25$  – case A c)  $k = 0.35$  – case G d)  $k = 0.5$  – case H.

Indeed, the size of the separation bubble becomes larger and larger with the reduced frequency. This first observation explains why the level of drag at the very beginning of the cycle gets larger at higher frequencies. By comparing the levels of vorticity magnitude at the tips on Figure 3.35, we can see that they increase with  $k$ . This is made obvious on the following Figure 3.37, as the streamwise vorticity alone appears, thus highlighting the progressive increase in size of the vortex core. In terms of effect on the spanwise vorticity variation, it becomes larger and larger along with the vortex size. On Figure 3.35 d) we see that the variations in vorticity magnitude on the top surface of the flat-plate, mainly representing the spanwise vorticity component, occur much faster as  $k$  increases.

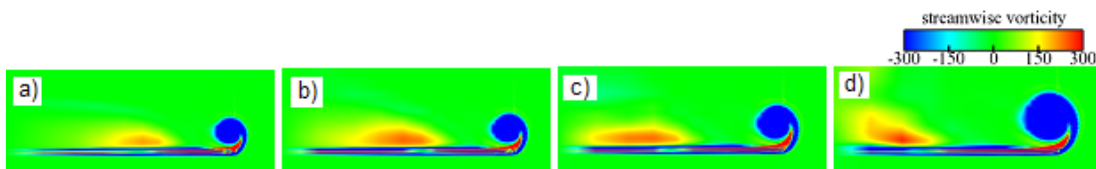


**Figure 3.37 :** Streamwise vorticity in the TE plane at  $a = 0$  a)  $k = 0.15$  – case F b)  $k = 0.25$  – case A c)  $k = 0.35$  – case G d)  $k = 0.5$  – case H.

Indeed, the portion of the wing under the effect of the tip vortex is enlarged, thus further reducing the fully separated flow region.

To confirm these observations we compare on Figure 3.38 the levels of vorticity magnitude, at the same time  $t = 0$  for  $k$  equal to 0.15 and 0.5 in three different planes, located in the symmetry plane and at 50% and 75% along the span. At these locations, since the vorticity is mainly rotating spanwise, these pictures are good indicators of the amount of boundary layer separation. As we just commented, the separation is larger in the symmetry plane for  $k = 0.5$  however it appears considerably reduced in planes located at 50% and 75% of the span width. Already at 50% the separation bubble is reattached which is not yet the case if  $k$  equals 0.15. At 75% both are reattached but the LEV is much smaller for 0.5.

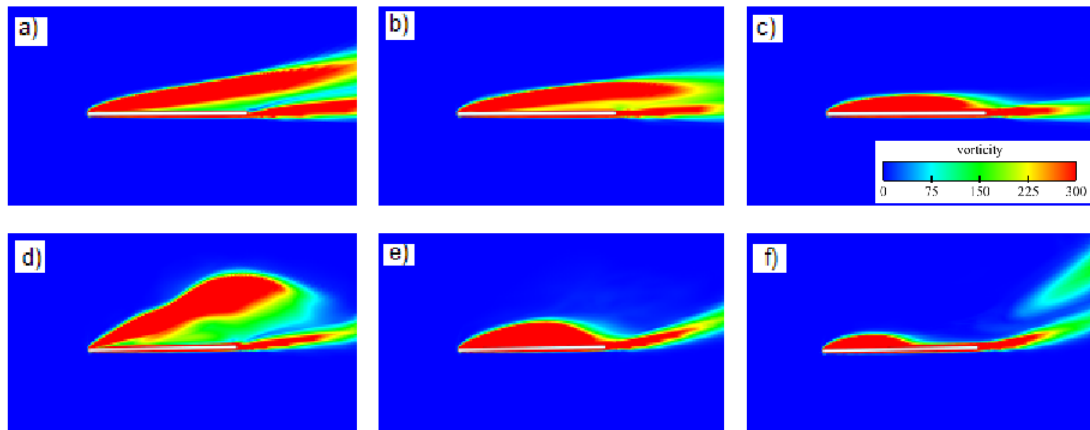


**Figure 3.38 :** Contours of vorticity magnitude at  $t = 0$  a) sym. plane,  $k = 0.15$  – case F b) plane at 50% span,  $k = 0.15$  – case F c) plane at 75% span,  $k = 0.15$  – case F d) sym. plane,  $k = 0.5$  – case H e) plane at 50% span,  $k = 0.5$  – case H f) plane at 75% span –  $k = 0.5$  – case H.

Although the size of the separation region was shown to increase with  $k$  at time  $t = 0$ , this only holds for a small portion of the cycle around the very bottom plunge position. For all the rest of the period, the flow behaves in the opposite way. Indeed, at all times the flow presents less and less separation, due to the shortening of the wave length of the flapping motion combined to the enlargement of the tip vortex. On Figure 3.39, the velocity vector flow fields are represented in the symmetry plane.

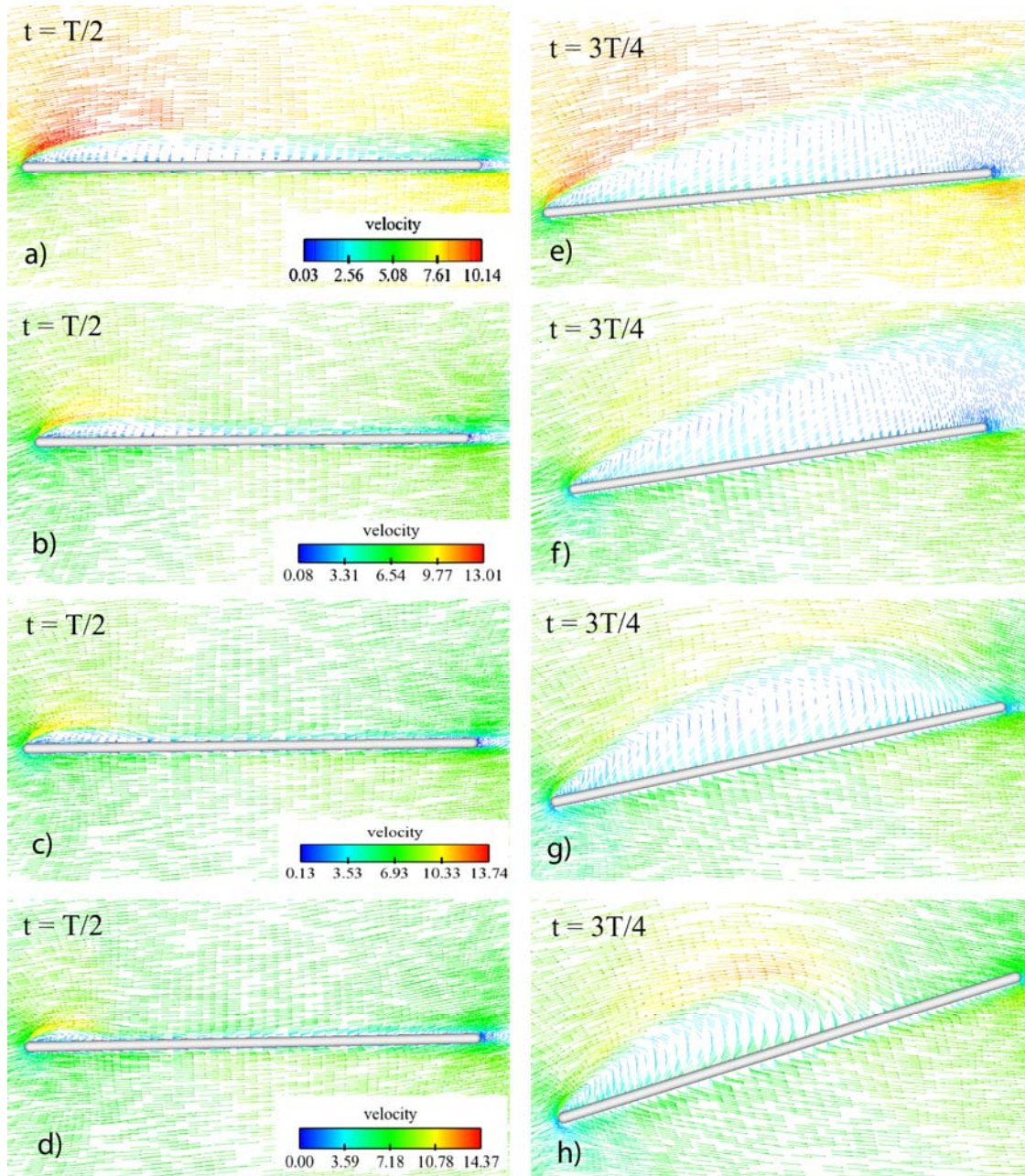


**Figure 3.39 :** Velocity vector flow fields in the symmetry plane a)  $t = T/2$ ,  $k = 0.15$  – case F b)  $t = T/2$ ,  $k = 0.25$  – case A c)  $t = T/2$ ,  $k = 0.35$  – case G d)  $t = T/2$ ,  $k = 0.5$  – case H e)  $t = 3T/4$ ,  $k = 0.15$  – case F f)  $t = 3T/4$ ,  $k = 0.25$  – case A g)  $t = 3T/4$ ,  $k = 0.35$  – case G h)  $t = 3T/4$ ,  $k = 0.5$  – case H

On pictures a) to d), at  $t = T/2$  which is characterized by the presence of the LEV that started forming around  $T/4$ , we observe that the size of the laminar separation bubble decreases dramatically from  $k$  equal to 0.15 to 0.5. The same remark can be made as we observe the pictures from e) to f) taken at time  $t = 3T/4$ . For  $k$  equal 0.15, the LEV has spread beyond the trailing-edge and the flow is fully separated whereas for 0.25 it has just reached the end of the flat-plate. For higher values, the flow

reattaches before the end, as the spreading of the LEV has been controlled by the increasingly large tip vortex associated to a smaller wave length. The reduction of the separation area explains the lower drag levels observed for  $k$  equal 0.35, which are further reduced when  $k$  equals 0.5.

All these observations can also be made based on the comparison of the pressure distributions throughout the cycle, plotted on Figure 3.40.

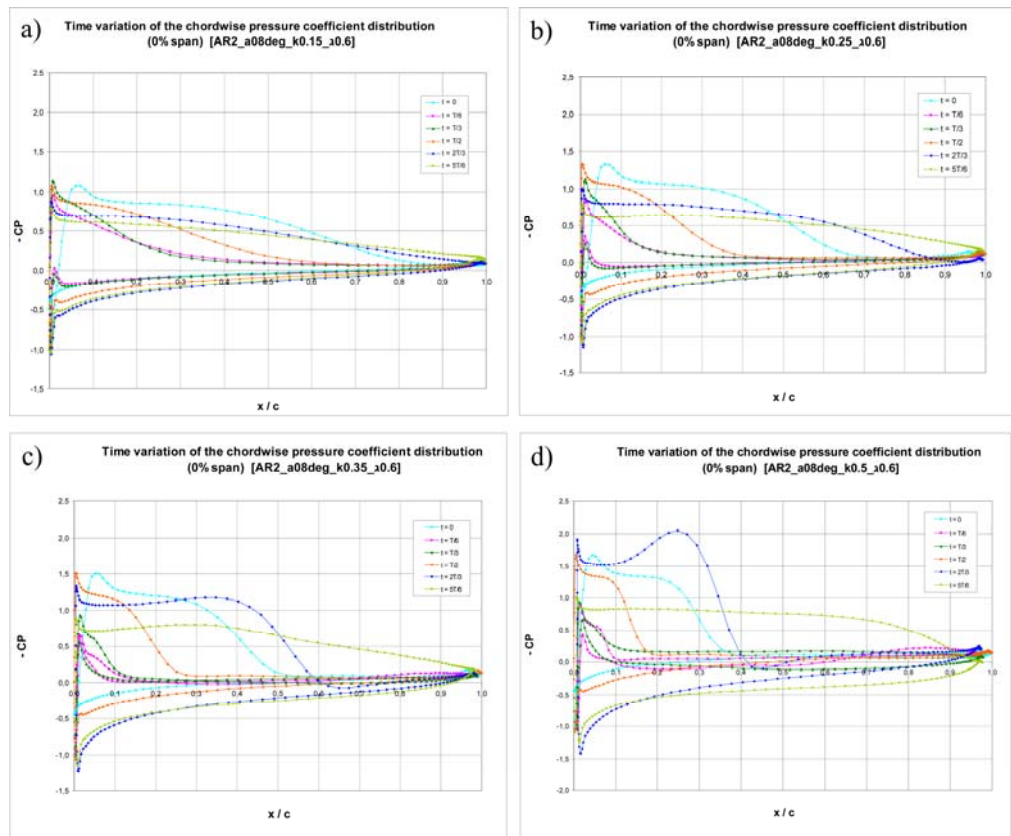


**Figure 3.40 :** Pressure distributions in the symmetry plane a)  $k = 0.15$  – case F b)  $k = 0.25$  – case A c)  $k = 0.35$  – case G d)  $k = 0.5$  – case H.

These also indicate that at all times, the extent of the separation region along the chord decreases as the reduced frequency gets higher. We see this from the length of the flatter portion of the curve. The second remark we may formulate is that while the values decrease sooner along the chord, at the contrary the pressure differences between upper and lower surfaces get more and more important. This is a sign of the augmentation of the suction force that causes the progressive gain in lift as  $k$  increases.

Let us now investigate the effect of the drop in drag on the thrust coefficient values. These are summarized in Table 3.7 which also provides the power input coefficient and the propulsive efficiency when it can be defined.

**Table 3.7:** Effect of the reduced frequency on the performance parameters

reduced frequency $k$	$C_T$	$C_{P IN}$	$\eta$ (efficiency)
0,15	-0,062	0,018	x
0,25	-0,045	0,055	x
0,35	-0,022	0,115	x
0,5	0,024	0,254	0,095

The thrust was found to be negative even for  $k$  equal 0.35 since the overall drag value remained positive. We deduce that up to then all the configurations were drag-producing. However, for a value of 0.5, integrating the drag force throughout the period finally provides a force in the direction of motion of the flat-plate, thus positive and equal to 0.024. Consequently, the system can be qualified as thrust-producing. A value can now be attributed to the propulsive efficiency which up to then did not have any meaning for negative thrust. Of interest in this parameter, is the necessary power input that appears at the denominator. It increases as the work needed to sustain the flapping motion gets larger when  $k$  rises. This is partly responsible for the very low efficiency of 0.095 that was calculated.

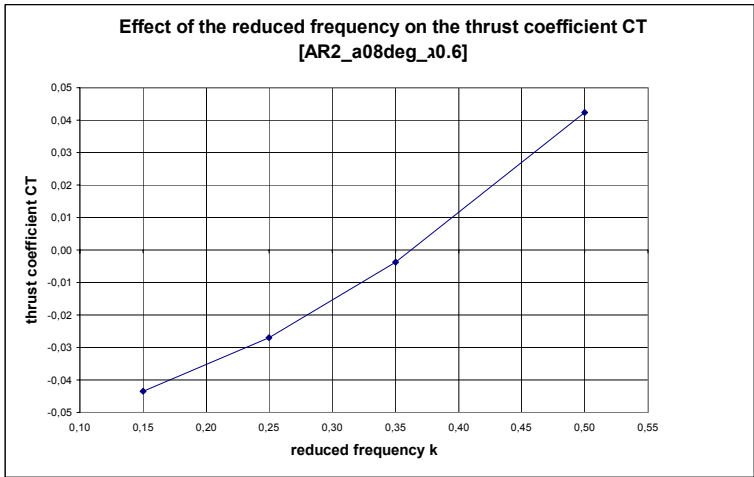


**Figure 3.41 :** Effect of the reduced frequency on the thrust coefficient

To conclude we may say that a minimum reduced frequency must be exceeded to produce thrust instead of drag. On Figure 3.41 is plotted the evolution of the thrust coefficient as a function of the reduced frequency.



This last parametric study has proved to be very promising since the thrust increases approximately linearly with the reduced frequency. We may conclude that shortening the wave length of the flapping motion is very beneficial and should be further applied in order to obtain higher thrust values and more efficient systems.

### 3.6 Conclusions

Based on the series of results that were collected and the discussions which took place for each of the parametric studies, let us summarize the important points and conclude. It appears that the range of parameters that were used for this project did not lead to many thrust-producing configurations. The cases of drag-generating motion were characterized by a strong flow separation giving rise to generation of vortices at the leading-edge which then spread across the entire upper surface. Eventually, the bursting of the separation bubble led to a fully separated flow for part of the cycle. For a reduced frequency of 0.25, these adverse effects could be limited by imposing a smaller aspect ratio of 1 and a reduced mean flow angle of 4 degrees. In the first case, it is thanks to the enlargement of the tip vortex relative to the wing span, that the spreading of the LEV across the flat-plate could be further controlled and limited to a smaller portion of the plate. As for the second case, the adverse pressure gradients were weakened by reducing the mean incidence and thus slowing down the extension of the separation bubble downstream. The flat-plate geometry was proved to be very sensitive to the mean angle of attack of the flow. Due to the absence of bluntness, the flow is very lightly to separate at the leading-edge. However, we have shown that the growth and extent of the separation should be limited by controlling the parameter  $\alpha_0$ . It is critical that its value is contained in the linear portion of the lift and drag curves as a function of the incidence, without which the aerodynamic performance of the flapping wing deteriorates rapidly, as it was the case for a value of 8 degrees. In terms of amplitude ratio, comparing the results obtained for several values indicated the existence of an optimum. Finally by varying the reduced frequency, this last parametric study showed that the range of variation, where  $k$  was contained within the interval [0.15 - 0.5] and especially the reference value of 0.25 chosen for this numerical work, in correspondence to future experimental studies, were not high enough. Indeed, as it was increased to the upper limit 0.5, the performance attained by the flapping system was considerably

improved since a thrust-producing motion appeared. Reducing the period of the cycle resulted in limiting the flow separation which did not extend so much to the downstream. In addition, the spreading of the LEV was further reduced by the formation of a stronger tip vortex. Consequently, the boundary layer resists better to adverse pressure gradients which may allow higher mean flow angles in order to further support the motion by generating a larger average lift force. The behaviour of the thrust coefficient with the reduced frequency is very promising since the trend indicates an ever increasing thrust force as  $k$  gets higher. We should bear in mind of course that as a propulsive system, the conditions of high thrust should be combined to high efficiency. Unfortunately, the present simulations do not permit us to draw a behaviour for the propulsive efficiency since not enough data was collected for positive thrust values. However we may acknowledge the fact that it should at first increase up to an optimum, whose value depends on all flapping parameters, and then start to drop when much higher thrust values are reached. Considering all the observations and conclusions that could be drawn from the present results, we may conclude by saying that it is necessary to perform further calculations which would take place at higher reduced frequencies. In preparation to these additional runs, we may refer to a few references. In the work conducted by M. S. Triantafyllou et al. [48] at a Reynolds number of 3000, the development of a reversed von Karman street inducing positive thrust, was best achieved for a Strouhal number between 0.25 and 0.35. The optimum propulsive efficiency was also contained within this Strouhal range. Our computations being based on the reduced frequency, an equivalent interval was calculated and corresponds to  $k$  within [0.8 – 1.1]. The thrust coefficient that was obtained is plotted as a function of  $St$  on Figure 3.42 a). It indicates that in their case, drag-producing motions were obtained for Strouhal numbers below 0.1 for which  $k$  equals 0.31. This transition point is close to ours and explains why our simulations mainly resulted in negative thrust values. The experimental study made by K. D. Jones [19] led to a wake classification based on observed vortex positions represented on Figure 3.42 b).

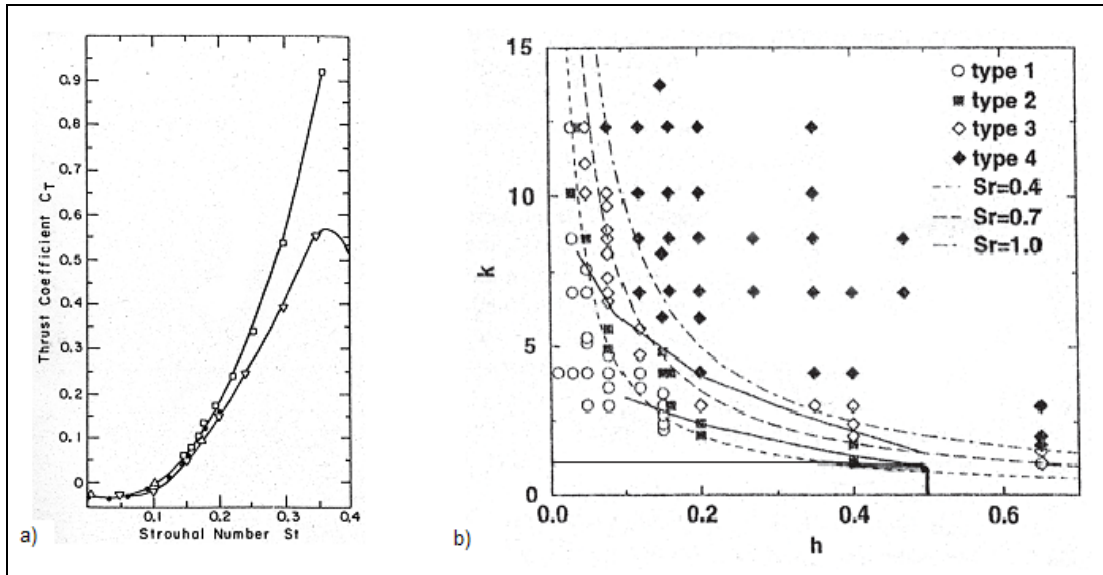


**Figure 3.42 :** a) Experimental data for the average thrust coefficient of an airfoil [48]  
 b) Wake classification based on observed vortex positions [19]

Type 1 and 3 indicate drag and thrust production respectively, whereas type 2 is the dividing line between the two, yielding into neither thrust nor drag. Type 4 shows cases for which both thrust and lift were produced. This plot also incorporates the effect of the plunge amplitude  $h$ . For a value of 0.5 that was assigned in our calculations,  $k$  had to exceed 1 to produce thrust. However, in this study the reduced frequency is defined with a factor of 2 compared to our definition and therefore brought back to our scale of reference  $k$  had to exceed 0.5. This is very close to our result since at this value, we have obtained a very low thrust which has just started to become positive, indicating a near transition from drag to thrust production. Although these other studies were made at different Reynolds numbers and used different geometries, the predominance of the reduced frequency as a governing parameter allows us to consider them as reference. While extending this project, these results combined to other references will therefore guide us for choosing a more appropriate interval of variation for the reduced frequency.



## REFERENCES

- [1] **Ifju, P. G., Jenkins, A.D., Ettingers, S., Lian, Y., and Shyy, W.**, 2000. Flexible-Wing Based-Micro Air Vehicle, AIAA Paper 2002-0705.
- [2] **Kroo, I., Kunz, P.**, 2001. Mesoscale Flight and Miniature Rotorcraft Development, Fixed and Flapping Wing Aerodynamics for Micro Air Vehicle Applications, p: 503-517.
- [3] **Tuncer, I. H., Kaya, M.**, 2003. Thrust Generation Due to Flapping Airfoils in a Biplane Configuration, Journal of Aircraft, Vol. 40, No. 3, pp. 509-515.
- [4] **Jones K. D., Platzer M. F.**, 2003. Experimental Investigation of the Aerodynamic Characteristics of Flapping-Wing Micro Air vehicles, AIAA Paper No. 2003-0418.
- [5] **Leishman, J.G.**, 2000. Principles of Helicopter Aerodynamics, Cambridge University Press, Cambridge, England, UK, Chapter 7.
- [6] **Rayner, J. M. V.**, 1999. Estimating Power Curves for Flying Vertebrates, Journal of Experimental Biology, Vol. 202, No. 23, pp. 3449-3461.
- [7] **Leishman, J. G.**, 2000. Principles of Helicopter Aerodynamics, Cambridge University Press, Cambridge, England, UK, Chapter 7.
- [8] **Knoller, R.**, 1909. Die Gesetze des Luftwiderstandes, Flug- und Motortechnik (Wien), Vol. 3, No. 21, pp. 1-7.
- [9] **Betz, A.**, 1912. Ein Beitrag zur Erklarung des Segelfluges, Zeitschrift fur Flugtechnik und Motorluftschiffahrt, Vol. 3, pp. 269-272.
- [10] **Katzmayr, R.**, 1922. Effect of Periodic Changes of Angle of Attack on Behavior of Airfoils, NACA TM 147.
- [11] **Birnbaum, W.**, 1924. Das ebene Problem des Schlagenden Fluegels, Zeitschrift fuer Angewandte Mathematik und Mechanik, Vol. 4, No. 4, pp. 277-292.
- [12] **Kuchemann, D., and Weber, J.**, 1953. Aerodynamic Propulsion in Nature, Aerodynamics of Propulsion, McGraw-Hill, New York, pp. 248-260.
- [13] **Prandtl, L.**, 1924. Uber die Entstehung von Wirbeln in der idealen Fliissigkeit, mit Anwendung auf die Tragfliigeltheorie und andere Aufgaben, Hydro- und Aerodynamik, Berlin, Julius Springer Verlag, pp. 18-33.
- [14] **Theodorsen, T.**, 1935. General Theory of Aerodynamic Instability and the Mechanism of Flutter, NACA, Rept. 496.
- [15] **Garrick, I. E.**, 1936. Propulsion of a Flapping and Oscillating Airfoil, NACA Rept. 567.

- [16] **Von Kármán, T. and Burgers, J. M.**, 1934. *Aerodynamic Theory*, vol. 2. Berlin: Springer.
- [17] **Lai, J. C. S. and Platzer, M. F.**, 1999. Jet Characteristics of a Plunging Airfoil, *AIAA Journal*, vol. 37, pp. 1529- 1537.
- [18] **Hess, J. L. and Smith, A. M. O.**, 1966. *Calculation of Potential Flow about Arbitrary Bodies*, Progress in Aerospace Sciences, Vol. 8, Pergamon Press.
- [19] **Jones, K.D., Dohring, CM. and Platzer, M.F.**, 1998. Experimental and Computational Investigation of the Knoller-Betz Effect, *AIAA Journal*, Vol. 36, No. 7, pp. 1240-1246.
- [20] **Tuncer, I. H. and Platzer, M. F.**, 1996. Thrust Generation due to Airfoil Flapping, *AIAA Journal*, vol. 34, pp. 324-331.
- [21] **Jones, K. D. and Platzer, M. F.**, 1997. Numerical Computation of Flapping-Wing Propulsion and Power Extraction, 35th Aerospace Sciences Meeting & Exhibit.
- [22] **Lai, J. C. S., and Platzer, M. F.**, 1999. Jet Characteristics of a Plunging Airfoil, *AIAA Journal*, Vol. 37, No. 12, pp. 1529-1537.
- [23] **Windte, J., Radespiel, R., and Neef, M.**, Aerodynamic Analysis of Flapping Airfoil Propulsion at Low Reynolds Numbers.
- [24] **Kussner, H. G.**, 1936. Zusammenfassender Bericht "über den instationären Auftrieb von Flügeln, *Luftfahrtforschung* 13, S. 410-424.
- [25] **Tuncer, I. H., Walz, R., and Platzer, M. F.**, 1998. A Computational Study on the Dynamic Stall of a Flapping Airfoil, in 16th Applied Aerodynamics Conference, Technical Papers (A98-32401 08-02) Albuquerque, NM: AIAA.
- [26] **Platzer, M. F., Jones, K. D., Young, J., and Lai, J. C. S.**, 2007. Flapping Wing Aerodynamics - Progress and Challenges, *AIAA Journal* (under review).
- [27] **Lewin, G. C., and Haj-Hariri, H.**, 2003. Modelling Thrust Generation of a Two-Dimensional Heaving Airfoil in a Viscous Flow, *Journal of Fluid Mechanics*, Vol. 492, pp. 339-362.
- [28] **Young, J., and Lai, J. C; S.**, 2004. Oscillation Frequency and Amplitude Effects on the Wake of a Plunging Airfoil, *AIAA Journal*, Vol. 42, No. 10, pp. 2042-2052.
- [29] **Bratt, J. B.**, 1953. Flow Patterns in the Wake of an Oscillating Airfoil, Aeronautical Research Council, pp. 17–24.
- [30] **Ashraf, M. A., Lai, J. C. S. and Young, J.**, 2007. Numerical Analysis of Flapping Wing Aerodynamics, 16<sup>th</sup> Australian Fluid Mechanics Conference, Gold Coast, Australia.
- [31] **Koochesfahani, M. M.**, 1989. Vortical Patterns in the Wake of an Oscillating Airfoil, *AIAA Journal*, vol. 27, pp. 1200-1205.
- [32] **Sarkar, S. and Venkatraman, K.**, 2006. Thrust Generation in Pitching Airfoils, *Computers & Fluids*, vol. 35, pp. 16-42.

- [33] **Jones, K.D., Lund, T. C., and Platzer, M. F.**, 2001. Experimental and Computational Investigation of Flapping Wing Propulsion for Micro Air Vehicles, Vol. 195, Progress in Astronautics and Aeronautics, AIAA, New York, pp. 307-339.
- [34] **Tuncer, I. H., Walz, R., and Platzer, M. F.**, 1998. A computational study on the Dynamic Stall of a Flapping Airfoil, 16<sup>th</sup> Applied Aerodynamics Conference, Technical Papers (A98-32401 08-02), Albuquerque, NM: AIAA.
- [35] **Isogai, K., Shinmoto, Y., and Watanabe, Y.**, 1999. Effects of Dynamic Stall on Propulsive Efficiency and Thrust of Flapping Airfoil, AIAA Journal, Vol. 37, No. 10, pp. 1145-1151.
- [36] **Anderson, J.M., Streitlin, K., Barrett, D.S., and Triantafyllou, M.S.**, 1998. Oscillating Foils of High Propulsive Efficiency, Journal of Fluid Mechanics, Vol. 360, pp. 41-72.
- [37] **Jane Wang, Z.**, ‘Vortex Shedding and Frequency Selection in Flapping Flight,’ Journal of Fluid Mechanics, Vol. 410, pp. 323-341
- [38] **Guglielmini, L. and Blondeaux, P.**, 2004. Propulsive Efficiency of Oscillating Foils, European Journal of Mechanics – B/Fluids, vol. 23, pp. 255-278.
- [39] **Ramamurti, R. and Sandberg, W.**, 2001. Simulation of Flow about Flapping Airfoils using Finite Element Incompressible Flow solver, AIAA Journal, vol. 39, pp. 253-260.
- [40] **Young, J., and Lai, J. C . S.**, 2007. Mechanisms Influencing the Efficiency of Oscillating Airfoil Propulsion, AIAA Journal, Vol. 45, No. 7, pp. 1695-1702.
- [41] **Read, D. A., Hover, F. S., and Triantafyllou, M. S.**, 2003. Forces on Oscillating Foils for Propulsion and Maneuvering, Journal of Fluids and Structures, vol. 17, pp. 163-183.
- [42] **Tuncer, I. H., and Kaya, M.**, 2005. Optimization of Flapping Airfoils for Maximum Thrust and Propulsion Efficiency, AIAA Journal, Vol. 43, No. 11, pp. 2329–2341.
- [43] **Neef, M. F., and Hummel, D.**, 2001. Euler Solutions for a Finite-Span Flapping Wing, Progress in Astronautics and Aeronautics, Vol. 195, Chap. 19, pp. 429–451.
- [44] **Hall, K. C., and Hall, S. R.**, 2001. A Rational Engineering Analysis of the Efficiency of Flapping Flight, Progress in Astronautics and Aeronautics, Vol. 195, Chap. 13, pp. 249–274.
- [45] **von Ellenrieder, K. D., Parker, K., and Soria, J.**, 2003. Flow Structure behind a Heaving and Pitching Finite-Span Wing, Journal of Fluid Mechanics, Vol. 490, pp. 129–138. doi:10.1017/S0022112003005408.
- [46] **Blondeaux, P., Fornarelli, F., Guglielmini, L., Triantafyllou, M. S., and Verzicco, R.**, 2005. Numerical Experiments on Flapping Foils Mimicking Fish-like Locomotion, Physics of Fluids, Vol. 17, pp. 113601-1 to 12.

- [47] **Anderson, J. D.**, 1995. Computational Fluid Dynamics.
- [48] **Triantafyllou, M. S., Triantafyllou, S., Gopalkrishnan, R.**, 1991. Wake mechanics for thrust generation in oscillating foils, *Phys. Fluids A*, Vol. 3, No. 12.



## **APPENDICES**

**APPENDIX A:** Computational studies on plunging and flapping airfoils

---

**APPENDIX B:** Streamwise contours of vorticity magnitude: tip vortex

APPENDIX A

COMPUTATIONAL STUDIES OF PURE PLUNGING AIRFOIL

Author	Type of Study	Airfoil	Re	k	h	kh	Observations
Garrick [15]	Incompressible Potential flow	Flat plate theory	x	x	x	x	* if $k > 4$ : $C_T \propto kh$ * if $k < 4$ : additional dependence on $k$
Tuncer and Platzer [20]	Navier-Stokes	NACA 0012	$3 \times 10^6$	0.2 – 3	0.1 – 0.4	0.02 – 1.2	* $\eta_{P\_MAX} = 0.72, C_{Tmean} = 0.01$ [ $k = 0.2; h = 0.4$ ] * tandem $\Rightarrow 33\% \nearrow \eta_p$ & $40\% \nearrow C_{Tmean}$ for [ $k = 0.75; h = 0.2$ ]
Jones et al. [21]	2D incompressible unsteady panel method	NACA 0012 0015 0009 0003	x	0.01 - 10	0.1 – 0.4	0.001 – 4	* $\eta_{P\_MAX} = 0.519, C_{Tmean} = 2.13$ [ $k = 4; h = 0.4$ ] $C_{Tmean\_MAX} = 2.5, \eta_p = 0.293$ [ $k = 4; h = 0.4$ ] * $\Delta thickness \Rightarrow negligible effect on \eta_p and C_{Tmean}$
Windte et al. [23]	RANS solver FLOWer-Code	NACA 4402	6 000	0.1 – 1	x	x	* shed vortices $\Rightarrow phase shift \nearrow$ with $k$ * $C_x$ always + $\Rightarrow no thrust production$ At $Re = 6000$ , pure plunge impossible $\searrow$

Tuncer et al. [25]	2D compressible Navier-Stokes solver	NACA 0012	$10^6$				<ul style="list-style-type: none"> <li>* <math>C_T \nearrow</math> with <math>kh</math></li> <li>* <math>kh &lt; 0.35</math> to avoid dynamic stall that <math>\searrow \eta_P</math> &amp; <math>C_{Tmean}</math></li> </ul>
Lewin and Hariri [27]	2D incompressible Navier-Stokes solver	Elliptical airfoil	500	2 – 10	x	0.8 – 1.5	<ul style="list-style-type: none"> <li>* <math>\eta_{P\_MAX} = 0.11</math> [<math>k = 5.333 ; kh = 1.2</math>]</li> <li>* Aperiodic, assymmetric solutions with <math>\sim</math> no effect on <math>\eta_P</math></li> <li>* LEV shed <math>\Rightarrow</math> interactions <math>V</math> with TEV and <math>\searrow (\eta_P, C_T)</math></li> <li>* Dissipation of the LEV <math>\Rightarrow \nearrow</math> efficiency</li> </ul>
Young and Lai [28]	2D incompressible viscous NS solver	NACA 0012	20 000			0.6	<ul style="list-style-type: none"> <li>* <math>C_{T\_mean\_MAX} = 0.28</math> [<math>k = 32 ; h = 0.1875</math>]</li> <li>* Importance of <math>k</math> as a control parameter in addition to <math>kh</math>.</li> </ul>
Ashraf et al. [30]	2D compressible Navier-Stokes solver	NACA 0012	20 000	0.5 - 24	0.0125 - 48		<ul style="list-style-type: none"> <li>* <math>\eta_{P\_MAX} = 0.72, C_{Tmean} = 0.01</math> , fixed <math>h = 0.175</math> [<math>k = 2 ;</math></li> <li>* <math>\eta_P</math> &amp; <math>C_{Tmean}</math> depend on both <math>k</math> and <math>kh</math> independently</li> <li>* Optimized motion : high <math>k</math> &amp; low <math>h</math></li> </ul>

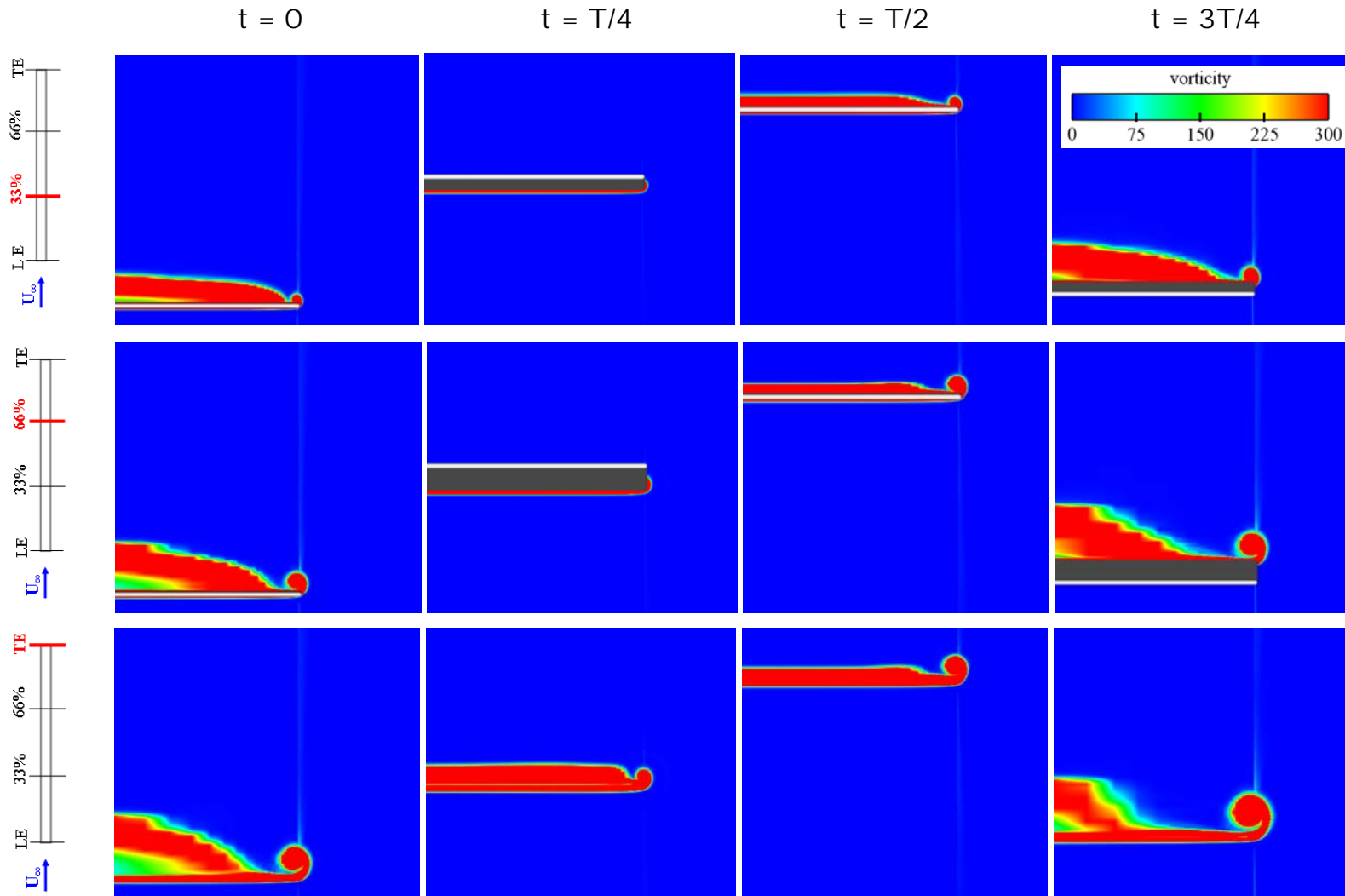
## COMPUTATIONAL STUDIES OF THE NACA 0012 AIRFOIL IN COMBINED PITCHING AND PLUNGING MOTION

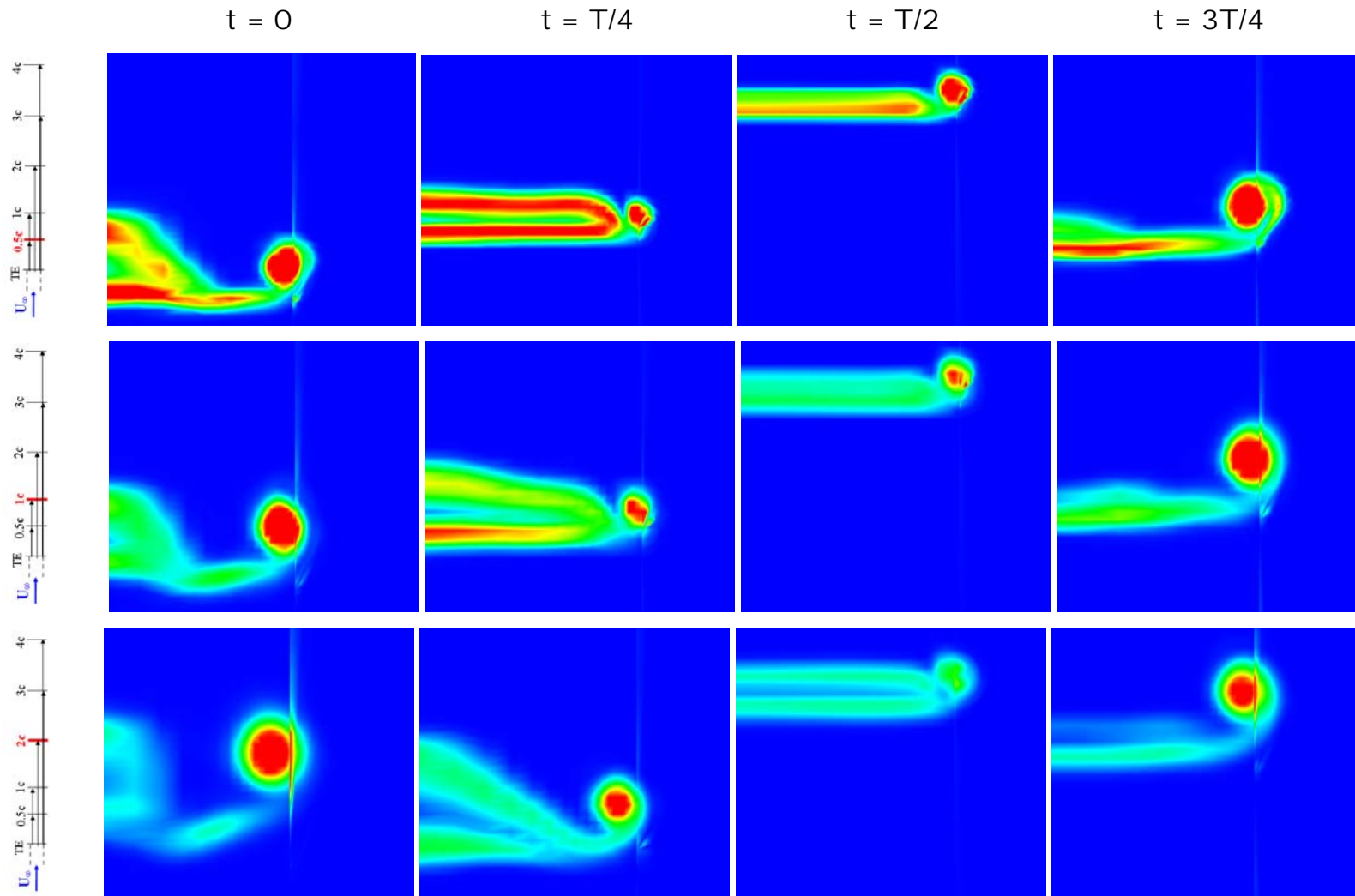
Author	Type of Study	Pitching axis	Re	k	h	kh (St)	$\theta_0$	$\phi$	Observations
Jones et al. [19]	Panel method	$1/4 \cdot c$	x	0.5	0.2	0.01	$4^\circ$	$[0^\circ ; 360^\circ]$	* <i>Linear theory and Panel method in good agreement</i> * <i>Phase angle <math>\phi = 90^\circ \Rightarrow \eta_{t\_MAX}</math></i>
Tuncer et al. [34]	2D Compressible Navier-Stokes (M = 0.3)	$1/2 \cdot c$	$10^5$	$[0.3 ; 1]$	1	$[0.3 ; 1]$	$10^\circ$	$[30^\circ ; 150^\circ]$	* <i>Phase angle <math>\phi = 90^\circ \Rightarrow \eta_{t\_MAX}</math> for any k</i> * <i><math>C_{Tmean\_MAX} = 1.3</math> for <math>k = 0.15</math> at <math>\phi = 30^\circ</math></i> * <i><math>\eta_{P\_MAX} = 0.86</math> for <math>k = 0.15</math> at <math>\phi = 90^\circ</math></i>
Isogai et al. [35]	2D Compressible Navier-Stokes (M = 0.3)	$1/2 \cdot c$	$10^5$	$[0.3 ; 1]$	0.5	$[0.15 ; 0.5]$	$20^\circ$	x	* <i><math>C_{Tmean\_MAX} = 0.70</math> for <math>k = 2.0</math> at <math>\phi = 120^\circ</math></i> * <i><math>\eta_{P\_MAX} = 0.72</math> for <math>k = 1.0</math> at <math>\phi = 90^\circ</math></i>
				$[0.3 ; 2]$	1	$[0.3 ; 2]$	$10^\circ$	x	* <i><math>C_{Tmean\_MAX} = 1.0</math> for <math>k = 0.3</math> at <math>\phi = 60^\circ</math></i> * <i><math>\eta_{P\_MAX} = 0.8</math> for <math>k = 0.3</math> at <math>\phi = 90^\circ</math></i>
Young and Lai [28]	Potential Flow Navier-Stokes	$1/3 \cdot c$	40 000		0.75	$[0.01 ; 3.0]$	$15^\circ$	$90^\circ$	* <i>Peak in <math>\eta_t</math> for <math>St \in [0.1 ; 0.2]</math></i>

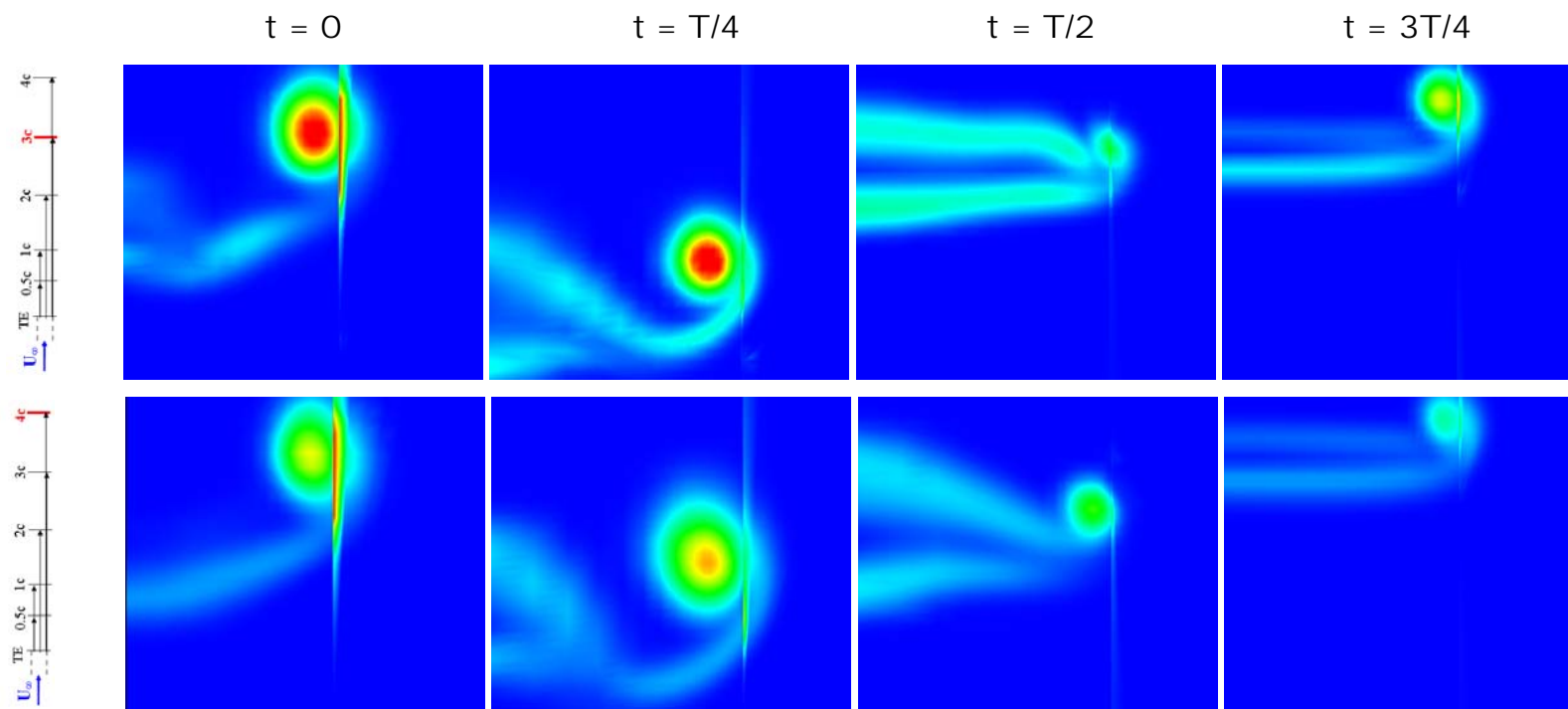
Guglielmini and Blondeaux [46]	Numerical solution of the vorticity equation	$[-0.5c; 2c]$	1100 3300		$[0.4; 4.5]$	$([0.15; 0.6])$	$[10^\circ; 40^\circ]$		<ul style="list-style-type: none"> <li>* <math>\eta_{P\_max}</math> for <math>h \sim 3</math></li> <li>* <math>\eta_{P\_max} = 0.45</math> for <math>(\alpha_{max} \in [30^\circ; 40^\circ] \text{ and } St \in [0.3; 0.4])</math></li> <li>* <math>\eta_{P\_max}</math> for <math>\varphi = 80^\circ</math></li> <li>* <math>\eta_{P\_max}</math> for pitching axis at <math>1/3 \cdot c</math></li> </ul>
Ramamurti and Sandberg [39]	2D Incompressible Navier-Stokes	$1/4 \cdot c$	1100	3.77, 5.65	1	3.77, 5.65	$15^\circ$	$[30^\circ; 140^\circ]$	<ul style="list-style-type: none"> <li>* <math>\eta_{P\_max} = 0.3</math> for <math>\varphi = 90^\circ</math> at <math>k = 5.65</math></li> <li>* <math>C_{T\_max} = 2.42, \eta_p = 0.24</math> for <math>\varphi = 120^\circ</math> at <math>k = 5.65</math></li> </ul>
Read et al. [41]	2D experiments	$1/3 \cdot c$	40 000	$[0.25; 1.9]$	0.75	0.094-0.69 (0.06-0.44)	$[10^\circ; 40^\circ]$	$[80^\circ; 100^\circ]$	<ul style="list-style-type: none"> <li>* <math>\eta_{P\_max} = 0.715, C_{T\_mean} = 0.18</math> for <math>\varphi = 90^\circ</math> and <math>kh = 0.502</math></li> <li>* <math>C_{T\_mean} = 2.41, \eta_p = 0.43</math>, for <math>\varphi = 100^\circ</math> and <math>kh = 1.88</math></li> <li>* Side force coeff.: 5.5 <math>\Leftrightarrow</math> excellent manoeuvring capabilities</li> </ul>
Tuncer and Kaya [42]	Navier-Stokes + optimization algorithm		$10^4$	1					<ul style="list-style-type: none"> <li>* <math>\beta = 1: \eta_{P\_max} = 0.675, C_{T\_mean} = 0.18</math> (<math>\varphi = 86.5^\circ, \alpha_{max} = 35.6^\circ, h = 0.83</math>)</li> <li>* <math>\beta = 0: C_{T\_mean\_max} = 1.45, \eta_p = 0.36</math> (<math>\varphi = 94.9^\circ, \alpha_{max} = 28.6^\circ, h = 1.55</math>)</li> <li>* <math>\beta = 0.5: C_{T\_mean\_max} = 1.08, \eta_{P\_max} = 0.44</math> (<math>\varphi = 97.8^\circ, \alpha_{max} = 29.6^\circ, h = 1.36</math>)</li> </ul>
Young and Lai [40]	2D unsteady Navier-Stokes	$1/3 \cdot c$	20000 - 40000	$[0; 2.15]$	0.25 – 0.75	$[0; 1.61]$	$[-15^\circ; 55^\circ]$	$[75^\circ; 90^\circ]$	<ul style="list-style-type: none"> <li>* Peak in <math>\eta_p</math> dependent on many factors, <math>St \in [0.1; 0.4]</math></li> <li>* At low <math>St</math>: (Viscous drag + LE separation) <math>\Rightarrow \searrow \eta_p</math></li> <li>* At high <math>St</math>: LE separation <math>\Rightarrow \searrow \eta_p</math></li> </ul>

## APPENDIX B

### STREAMWISE CONTOURS OF VORTICITY MAGNITUDE: TIP VORTEX













## **CURRICULUM VITA**



**Candidate's full name:** Sophia Catherine BUCKINGHAM

**Place and date of birth:** Paris, 31/12/84

**Permanent Address:** 20 rue Mouton Duvernet, 75014 Paris, France

**Universities and**

**Colleges attended:** ESTACA, France

Istanbul Technical University